DISS. ETH NO. 23270

Simulation and Experimental Studies of Polymer-Brushes under Shear

A thesis submitted to attain the degree of

DOCTOR OF SCIENCES of ETH ZURICH

(Dr. sc. ETH Zurich)

presented by

Manjesh Kumar SINGH

Master of Engineering, IISc, Bangalore

born on 06.05.1987

citizen of India

accepted on the recommendation of

Prof. Dr. Nicholas D. Spencer, examiner

Prof. Dr. Mark O. Robbins, co-examiner

Prof. Dr. Martin Kroger, co-examiner

Prof. Dr. Patrick Ilg, co-examiner

2016

न चोरहार्यं न च राजहार्यं न भ्रातृभाज्यं न च भारकारि।

व्यये कृते वर्धत एव नित्यं विद्याधनं सर्वधनप्रधानम्॥

"It cannot be stolen by a thief.
It cannot be taken away by a king.
It cannot be divided among siblings.
It does not cause load. It always increases when spent.
The wealth of education is the greatest of all wealth."

~The Vedas

For my family

Abstract

Nature has its own complex way of lubricating sliding surfaces with the help of glycoproteins. In recent times mankind has tried to imitate natural lubrication using polymer brushes. Polymer molecules are attached by one end to a surface using different approaches (‘grafting to’ or ‘grafting from’); if the surface grafting density is so high that the polymer chains start to overlap, they stretch away from the surface forming a polymer brush. The equilibrium brush height is larger than the size of the unperturbed chains in bulk solution. Polymer-brush-coated surfaces find applications in many fields including colloidal stabilization, adhesion, bio-compatibilization and tribology. The aim of this thesis is to understand the underlying molecular mechanisms of frictional behavior of polymer brushes and gels in a good solvent by employing complementary experimental and simulation studies.

The colloidal-probe-based lateral force microscopy (LFM) technique has been employed for experimental investigations, and used to study the frictional behavior of PLMA (poly lauryl methacrylate) brushes in hexadecane and PGMA (poly glycidyl methacrylate) brushes and gels in a dimethylformamide (DMF) solvent. Polymer brushes and gels were grafted on a silicon surface using SI-ATRP (surface initiated atom transfer radical polymerization) by another PhD student in the project. The ex-situ/post-modification method is used to fabricate PGMA gels of different degrees of crosslinking with two different lengths of crosslinkers to facilitate the study of the effect of crosslinking on the frictional behavior of polymer brushes. The AFM-based nanoindentation technique was employed to study the mechanical properties of PGMA brushes and gels in DMF.

Polymer brushes were modeled using a multibead-spring model and studied via molecular-dynamics (MD) simulations to understand their tribological behavior. The

simulations were performed for two kinds of systems (i) brush-against-brush and (ii) brush-against-wall. Both implicit and explicit solvent-based approaches have been employed in this thesis. Polymer chains are modeled as linear semi-flexible chains, randomly grafted on a planar surface with the help of tethered beads. In the first step, the polymer-brush-bearing surfaces (grafting surface and wall) are brought near to each other and allowed to equilibrate. In the next step, tethered beads are displaced at constant shear speed, keeping the separation between the brush bearing surfaces (brush and wall) constant. Simulations are performed over a range of shear speeds and separation between grafting surfaces (grafting surface and wall). Normal and shear stresses are calculated using the Irving-Kirkwood expression for the stress tensor. The coefficient of friction is defined as the ratio of shear and normal forces. Speed-dependent studies are carried out using an implicit-solvent approach for a fixed separation, whereas the separation-dependent studies are carried out at a fixed speed using an explicit-solvent approach. Simulations are performed on polymer brushes as well as gels for a combination of lengths of crosslinker chains and degree of crosslinking to facilitate the study of the effect of the crosslinking on the behavior of polymer brushes subjected to shear. Quantities extracted from the simulations are the normal and shear stresses, radius of gyration, density and velocity profiles and interdigitation for different combinations of shear speeds and separations between brush-bearing surfaces (brush and wall). At each stage, simulation results are compared with our experimental data to rationalize the behavior of end-grafted polymer chains under shear.

The combined experimental and simulation study offers a number of insights that will help to establish a framework for design rules for polymer-brush-based lubrication aiming at specific tribological properties.

f

Abstract

Die Natur hat ihren eigenen komplexen Weg gleitende Flächen mit der Hilfe von Glycoproteinen zu schmieren. In jüngster Zeit hat die Menschheit versucht die natürliche Schmierung mittels Polymerbürsten zu imitieren. Polymermoleküle werden durch unterschiedliche Methoden an einem Ende an der Oberfläche verankert (aufpfropfen reaktiver Polymere - 'grafting to' oder Oberflächen-initiiertes Polymerwachstum - 'grafting from'). Ist die Oberflächenpropfdichte hoch genug, dass sich die Polymerketten zu überlappen beginnen, strecken sich die Polymerketten senkrecht zur Oberfläche und bilden bürstenähnliche Schichten. Die Bürstenhöhe im Gleichgewicht ist grösser als die Grösse der Polymerketten in Lösung. Oberflächen mit bürstenähnlichen Schichten finden Anwendung in vielen Fachgebieten, wie Kolloidchemie, Adhäsion, Biokompatibilität und Tribologie. Das Ziel dieser Arbeit ist es, mit Hilfe von Simulationsstudien und komplementären experimentellen Untersuchungen, die zugrunde liegenden molekulare Mechanismen des Reibungsverhaltens von Polymerbürsten und Gelen in einem guten Lösungsmittel zu verstehen.

Für die experimentelle Untersuchung wurde mit kolloidaler Rasterkraftmikroskopie das Reibungsverhalten von PLMA (Poly Laurylmethacrylat) Bürsten in Hexadecan und von PGMA (Poly Glycidylmethacrylat) Bürsten und Gelen in Dimethylformamid (DMF) getestet. Ein anderer an diesem Projekt beteiligter Doktorand hat die Polymerbürsten und -gele mit Hilfe der Oberflächen-initiierten Atom Transfer Radical Polymerisation (SI-ATRP) auf einer Silizium-Oberfläche aufgebracht. Mittels einer ex-situ/Postmodifikationsmethode werden PGMA Gele mit unterschiedlichem Vernetzungsgrad hergestellt, wobei zwei verschieden lange Vernetzer verwendet werden, um den Effekt der Vernetzung auf das

Reibungsverhalten der Polymerbürsten zu untersuchen. Eine auf dem AFM basierende Nanoindentationstechnik wurde eingesetzt, um die mechanischen Eigenschaften von PGMA Bürsten und Gelen in DMF zu erforschen.

Um das tribologische Verhalten zu verstehen, wurden Polymerbürsten mit Hilfe eines Multibead-Spring Models modelliert und via Molekulardynamik-Simulation (MD) untersucht. Die Simulationen wurden für zwei Arten von Systemen ausgeführt, (i) Bürste-gegen-Bürste und (ii) Bürste-gegen-Wand. In dieser Arbeit wurden sowohl implizite, wie auch explizite Lösungsmittel-basierende Vorgehen genutzt. Polymerketten werden als lineare semi-flexible Ketten modelliert, die mit Hilfe von angeketteten Perlen zufällig auf einer ebenen Oberfläche verankert sind.

Im ersten Schritt werden Oberflächen mit bürstenähnlichen Schichten (beschichtete Oberfläche und Wand) nahe zueinander gebracht und äquilibriert. Im zweiten Schritt werden verankerte Perlen bei konstanter Schergeschwindigkeit versetzt während der Abstand zwischen den Bürsten-tragenden Oberflächen (Bürste und Wand) konstant gehalten wird. Simulationen werden über eine Reihe von Schergeschwindigkeiten und Abständen zwischen den bürstenähnlichen Schichten (beschichtete Oberfläche und Wand) ausgeführt. Die Normal- und Scherspannungen werden mit der Irving-Kirkwood Gleichung für den Spannungstensor berechnet. Der Reibungskoeffizient ist definiert als das Verhältnis der Scher- und Normalkräfte. Geschwindigkeits-abhängige Studien werden mit einem Ansatz für implizite Lösungsmittel und einen fixierten Abstand durchgeführt, während die Abstands-abhängigen Studien mit einer fixierten Geschwindigkeit und einem Ansatz für explizite Lösungsmittel durchgeführt werden. Um die Untersuchung des Effekts der Vernetzung auf das Verhalten von Polymerbürsten unter Scherung zu vereinfachen, werden Simulationen mit

Polymerbürsten als auch mit Gelen durchgeführt, wobei die Länge der Vernetzungsketten und der Vernetzungsgrad variiert werden.

Grössen die bei den Simulationen bestimmt werden sind Normal- und Scherspannung, Gyrationsradius, Dichte und Geschwindigkeitsprofile, sowie die Verzahnung für verschiedene Kombinationen von Schergeschwindigkeit und Abstand zwischen Bürsten-tragenden Oberflächen (Bürste und Wand). In jeder Phase werden die Simulation-Resultate mit unseren experimentellen Daten verglichen, um das Verhalten von Oberflächen-initiierten Polymerketten unter Scherung zu erklären.

Die Kombination von Simulation und experimenteller Beobachtung ermöglicht eine Anzahl von Erkenntnissen, die helfen werden, Rahmenbedingungen für Entwurfsregeln zu schaffen, mit welchen die Polymerbürsten-basierte Schmierung für spezifische tribologische Eigenschaften optimiert werden kann.

Chapter 1

Introduction

1.1 Theoretical Background

1.1.1 Polymer Brushes

Polymer brushes can be defined as assemblies of end-grafted (on any surface or interface) polymer chains in a good solvent with a sufficiently high grafting density that the chains stretch out to take on a brush-like form. They are normally of thicknesses of a few nanometers to a few micrometers.

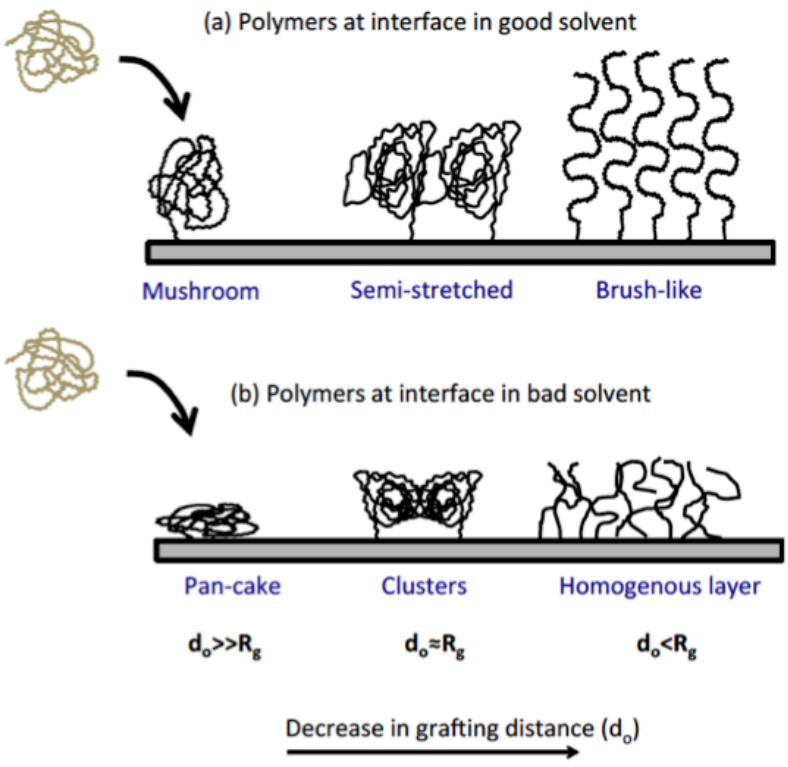

Figure 1.1: Schematic showing polymer chains in both a good and bad solvent at different grafting densities[1].

When polymer chains are grafted with low grafting density such that the distance between grafting points is much greater than the radius of gyration (R_g) of a single

unperturbed chain in bulk, the polymer chains take on a mushroom-like form in a good solvent, whereas they take on a 'pan-cake' like form by lying flat on the substrate in a bad solvent. As the grafting density is increased and grafting distance between the chains becomes comparable to the radius of gyration of a chain, macromolecules assume a semi-stretched form in a good solvent and take a 'cluster-like' form in a bad solvent. When the grafting density is further increased so that the grafting distance between the chains is less than the radius of gyration of a chain they stretch out, in order to avoid any segment-segment interaction, and form a brush-like structure in a good solvent but form a homogeneous layer on the grafting substrate in a bad solvent. The interaction among tethered chains results in a strong osmotic repulsive force in a good solvent, showing interesting interfacial features (lubrication and antifouling) due to this distinct physical structure. Polymer-brush-coated surfaces find applications in many fields including colloidal stabilization, adhesion, biocompatibility and tribology[2-6].

Polymer brushes can be synthesized using one of the following two methods: (i) 'grafting-to' or (ii) 'grafting-from'[7]. In the grafting-to approach the polymers are first prepared and then adsorbed onto the surface. The limitation of this method is that not very high grafting density polymer brushes can be synthesized using this approach. However, it can have the advantage of 'self-healing' as new chains present in the solvent replace the worn-off grafted chains. In the grafting-from approach the polymers are grown from initiators, which are covalently bonded to the surface. The advantage of this approach is that high grafting density polymer-brushes can be synthesized using this approach. Recent developments have focused on the grafting-from approach, which, by modulating the feed monomers to the reaction during synthesis, allows block copolymers to be synthesized, crosslinking to be switched on

and off during growth (yielding gel-like regions), and multilayered structures to be fabricated. This allows a major flexibility in the architecture of the brush, and therefore considerable design freedom concerning the dynamic properties of the polymer. Physical properties of polymer brushes depend on various parameters such as polymerization degree, grafting density, and solvent quality.

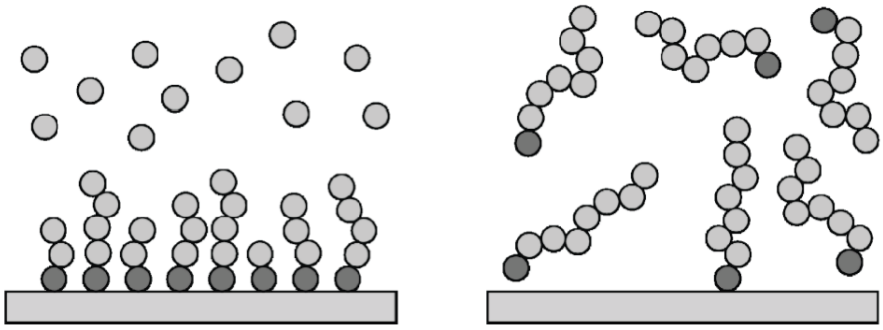

Figure 1.2: 'Grafting-from' (left) and 'grafting-to' (right) approaches to the synthesis of polymer brush[7].

1.1.2 Crosslinked Polymer Brushes/Gels

Crosslinked polymer brushes are called polymer brush-gels or simply gels. Surface-grafted polymer gels can be prepared using two different methods (i) in-situ and (ii) ex-situ method. In the in-situ method the polymer gels are prepared by crosslinking the chains while growing the chains from the grafting surface whereas in the ex-situ method polymer gels are prepared by crosslinking the chains in post-modification steps. Polymer gels have many applications in the fields of tissue engineering and bio-tribology[8,9].

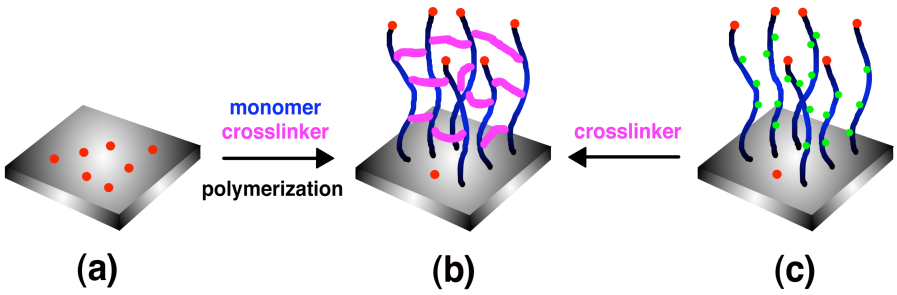

Figure 1.3: 'In-situ' and 'ex-situ' approach of synthesizing crosslinked polymer brushes[6].

1.2 Tribology

Tribology is a field of science that focuses on studies of friction, wear and lubrication of interacting surfaces under relative motion[10]. The word 'Tribology' is derived from the Greek word 'τριβοσ', which means rubbing or sliding. We can see implications of tribology in almost everything around us in our daily lives. Friction can be defined as resistance to motion when objects in contact try to slide relative to each other due to any external or internal influence. Friction has both advantages and disadvantages for humankind. For writing with pen or pencil, walking, running, driving, clutches and brakes, friction is essential, whereas for bearings, gears, cams and mechanical machining we aim to minimize friction. Wear is one of the most important reasons for material wastage and any reduction in wear leads to considerable savings. The goal of lubrication is to control friction and wear of surfaces under contact. Lubrication can be solid based (MoS_2, graphene, etc coating on surfaces to be lubricated) or liquid based (oil, emulsions, etc. between the surfaces to be lubricated). In lubricated systems, the Stribeck curve (Fig. 1.4) is typically used to express the coefficient of friction as a function of a combination of load, velocity and viscosity of the lubricant.

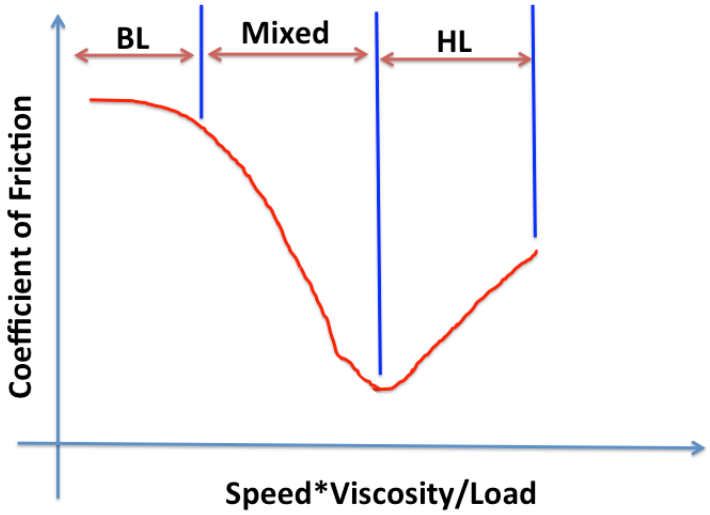

Figure 1.4: A typical Stribeck curve. BL stands for boundary lubrication and HL stands for hydrodynamic lubrication. The parameter speed*viscosity/load is also known as Sommerfeld number.

The first set of experiments in tribology was performed by Leonardo da Vinci (1452-1519). He concluded that the force needed to slide an object is independent of its position over a surface but it does depend on the weight of the object. Some two centuries later, and independently, Amontons proposed a general law for friction where the friction force (F) is equal to the product of normal load (L) and a parameter called coefficient of friction (μ). He also postulated that friction is independent of the apparent area of contact.

$$F = \mu L \tag{1.1}$$

Coloumb further added to Amontons' postulates the "law" that friction is independent of velocity. Later Tabor and Bowden found in their studies that while the apparent area of contact does not change under load, the real area of contact does vary. It is also important to state here that coefficient of friction is not a material constant but this value always refers to a tribological system under relative motion[11].

Tribology is also important for the economy of a country. Reports published as early as in the 1960s and the 1970s claimed that by proper implementation of principles of tribology, countries like the US, Britain and West Germany could save approximately 1% of their GDP. Today when the world is facing the challenge of global warming and the energy crisis, research in the field of 'Green Tribology' has become very widespread[10-12].

1.3 Polymer-Brush-Mediated Lubrication

Nature has its own complex way of lubricating sliding surfaces, involving glycoproteins, among other macromolecules. In recent times, humankind has tried to imitate nature lubrication using polymer brushes[13]. In previous studies, our laboratory has imitated the behavior of glycoproteins by adsorbing graft co-polymers poly(*L* lysine)-*graft*-poly(ethylene glycol) (PLL-*g*-PEG) and poly(*L* lysine)-*graft*-dextran

(PLL-*g*-dextran) structures onto a silica surface, in order to reduce the interfacial friction[14-17].

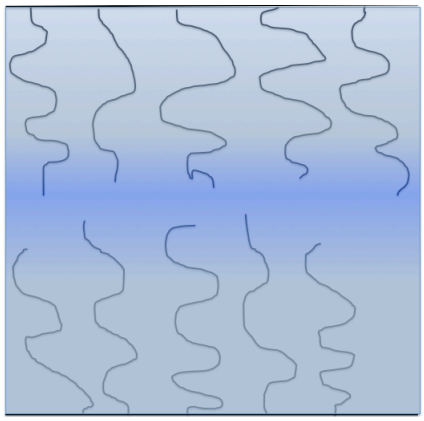

Figure 1.5: Schematic showing polymer-brush assisted lubrication.

When hard surfaces are brought in contact and sheared against each other, asperity-asperity contacts result in a high value of the coefficient of friction at the contact surface. In contrast, when polymer-brush-coated surfaces are sheared against each other in the presence of a good solvent, very low coefficients of friction are observed[18,19]. A strong entropic repulsive force prevents interdigitation of polymer chains even at high compressions, enabling the development of a thin fluid film between opposing brushes[20]. This thin fluid film assists in reducing friction at the interface. There have been several studies, both theoretical[21-25] and experimental[20,26-32], that have investigated the origin of frictional forces between contacting brushes at different shear rates, and at different loads.

Polymer-brush-based aqueous lubrication, as opposed to oil-based lubrication, is a promising candidate for having a positive impact on the environment. Although water has the advantage of possessing high thermal capacity and of being environmentally friendly, it is not *per se* as good a lubricant as oil, due to its low viscosity at high pressure. However, when water is used in conjunction with polymer brushes, the macromolecules, rather than hydrodynamic forces, can support the load, while a thin

layer of water between the brushes can reduce the friction by orders of magnitude. Concerns such as eco-toxicity, bioaccumulation and renewability of lubricants could, in principle, be readily addressed by using such water-based lubricants.

Tribological properties of polymer-brush based lubricants have long been studied under different loads and speeds. Different regimes of boundary and hydrodynamic have been established[10]. Both experimental and simulation studies have been carried out to understand the tribological behavior of polymer brushes in solvents. Experiments have been carried out to study the tribological behavior of polymer brushes at the nano, micro and macro scales. Nalam et.al[1] studied PLL-g-Dextran and PLL-g-PEG polymer brushes in different mixtures of solvent at the nano scale employing the surface forces apparatus (SFA) and colloidal- probe lateral force microscopy (LFM) at different load and speeds. They also carried out a macro-scale study using a macro-tribometer and a mini traction machine (MTM) and micro-scale studies with a microtribometer. Bielecki *et. al*[11] carried out experimental studies to understand the wear behavior of polymer brushes and polymer gels using a microtribometer. Klein et al.[20,26,27,33-35] used SFA in an oscillatory manner to measure both normal and shear forces. Tsuji et al.[31,36] studied the tribolological behavior of concentrated polymer brushes (CPBs) in mixtures of solvents. The effect of grafting density on the tribological response of polymer brushes was also studied and a 'transition -load' was reported at different grafting densities[16]. There has been great interest in the tribological behavior of gels[9,30,37-43]. Pan *et. al.*[39] studied the friction properties of poly(vinyl alcohol) hydrogels against titanium alloys for their application in articular cartilage. Poly(2-hydroxyethyl methacrylate) (PHEMA) hydrogels have also been of special interest for researchers for its application in bio-tribology and studies have been carried out for different combinations of substrate and

counter-surface[9,38,44,45]. Ishikawa *et al.*[46] have studied the role of solvent water in the lubrication behavior of hydrogels using pin-on-disk experiments. Dunn *et. al.*[8] have explored the distinctions between the self-mated "Gemini" hydrogel interface and hydrogels sliding against hard impermeable counter surfaces.

The first theoretical studies of polymer brushes on flat surfaces were performed by Alexander[47], de Gennes[48] and Semenov[49]. Alexander and de Gennes had assumed a 'step-like' density profile, but Milner[50] later suggested a parabolic density profile in his work. The concept of strong stretching of brushes was implemented by Milner[50] and Zhulina[51] in their work independently, implying that the brush height is much larger than an unperturbed extension of a single chain. Simulation work to understand polymer brush behavior have been carried out using various approaches such as Monte Carlo[52-54], Brownian dynamics[23] and dissipative particle dynamics[18]. Several molecular-dynamics simulation studies have been also carried out to understand the details of polymer-brush-based tribology using implicit[25,55-58] and explicit solvents[59-68]. Prior to Galuschko et. al.[22,69] there were not many molecular dynamics studies comparing implicit-solvent- and explicit-solvent-based approaches. Simulation studies have focused on different thermostat approaches, and a comparison of Langevin dynamics and dissipative dynamics methods has been published[70]. Most of the implicit-solvent-based studies have considered the Langevin dynamics approach. Simulation studies on gels have been mostly focused on the confirmation and solvent-gel interactions[71-75]. To the best of my knowledge there has not been any simulation studies of the tribological behavior of gels.

1.4 Aim of the Thesis

- To characterize the tribological behavior of various polymer-brush systems (synthesized by PhD student Chengjun Kang). Friction measurements were

carried out at different sliding speeds and various applied loads, so as to enable comparisons with modeling results under different conditions, to pursue the understanding of the brush behavior at the molecular scale.

- To model polymer brushes using a multibead-spring, coarse-grained molecular-dynamics simulation technique to study the effect of brush architectures on their tribological behavior.
- To maintain a close interaction between experimental and simulation efforts to elucidate details of the molecular design of brush systems with specific tribological properties.

1.5 Outline of the Thesis

The present work involves both experimental and simulation studies of polymer brushes under shear. In Chapter 2 a description of the experimental approach taken in this thesis is provided. All the friction experiments are performed using colloidal-probe lateral force microscopy and the chapter discusses the calibration method for cantilevers. Further indentation experiments using atomic force microscope (AFM) are also mentioned.

In Chapter 3, experimental results for poly (lauryl methacrylate) (PLMA) and poly (glycidyl methacrylate) (PGMA) brushes and gels are presented. The effects of the degree and length of crosslinkers on tribological behavior of PGMA gels have been presented and are compared with PGMA brushes.

Chapter 4 discusses the modeling approach employed for coarse-grained molecular-dynamics simulations of polymer brushes in this thesis. Polymer chains, implicit and explicit solvent including thermosttating, shear and chain-stiffness modeling including all the potentials used is explained in detail.

Chapter 5 presents the results for modeling of dextran brushes. Both quantitative and qualitative comparison with previously published experimental[14,15] work has been presented. A 'Boundary-like regime' observed in the experimental results is explained with the help of simulation work.

In Chapter 6, results for explicit-solvent-based MD simulations for a brush-against-brush system has been presented with a focus on the effect of grafting density and chain-stiffness of tribological behavior of polymer brushes.

In Chapter 7, simulation results for crosslinked polymer brushes have been presented. The effect of length of crosslinkers and degree of crosslinking has been studied and trends from simulation work have been compared with experimental results presented in Chapter 3.

Finally, in Chapter 8 a summary of the thesis is presented along with an outlook for future work.

1.6 References

(1) Nalam, P. C. *Polymer Brushes in Aqueous Solvent Mixtures: Impact of Polymer Conformation on Tribological Properties*; 2012.

(2) Napper, D. H. *Polymeric Stabilization of Colloidal Dispersions*; London ; New York : Academic Press, 1983.

(3) Hucknall, A.; Simnick, A. J.; Hill, R. T.; Chilkoti, A.; Garcia, A.; Johannes, M. S.; Clark, R. L.; Zauscher, S.; Ratner, B. D. Versatile Synthesis and Micropatterning of Nonfouling Polymer Brushes on the Wafer Scale. *Biointerphases* **2009**, *4* (2), FA50–FA57.

(4) Auroy, P.; Auvray, L.; Leger, L. Characterization of the Brush Regime for Grafted Polymer Layers at the Solid-Liquid Interface. *Phys. Rev. Lett.* **1991**, *66* (6), 719–722.

(5) Lee, S.; Spencer, N. D.; Erdemir, A.; Martin, J. M. Achieving Ultralow Friction by Aqueous, Brush-Assisted Lubrication. *Superlubricity* **2007**, 365–396.

(6) Li, A. *Structure-Property Relationships of Surface-Grafted Polymeric Architectures: From Ultra-Thin Films to Quasi-3D Polymer Assemblies*; 2013.

(7) Spencer, N. D. *Tailoring Surfaces*; World Scientific, 2011.

(8) Dunn, A. C.; Sawyer, W. G.; Angelini, T. E. Gemini Interfaces in Aqueous Lubrication with Hydrogels. *Tribol. Lett.* **2014**, *54* (1), 59–66.

(9) Freeman, M. E.; Furey, M. J.; Love, B. J.; Hampton, J. M. Friction, Wear, and Lubrication of Hydrogels as Synthetic Articular Cartilage. *Wear* **2000**, *241* (2), 129–135.

(10) Stachowiak, G. W.; Batchelor, A. W. *Engineering Tribology*; Elsevier : Amsterdam. London. New York. Tokyo, 1993.

(11) Bielecki, R. M. On Surface-Tethered, Hydrophobic and Lubricious Polymers, 2013, pp 1–152.

(12) Ramakrishna, S. N. *Adhesion and Tribology on Well-Defined, Nano-Scale Rough Surfaces: a Gradient Approach*; 2013.

(13) Lee, S.; Spencer, N. D. Sweet, Hairy, Soft, and Slippery. *Science* **2008**, *319* (5863), 575–576.

(14) Nalam, P. C.; Ramakrishna, S. N.; Espinosa-Marzal, R. M.; Spencer, N. D. Exploring Lubrication Regimes at the Nanoscale: Nanotribological Characterization of Silica and Polymer Brushes in Viscous Solvents. *Langmuir* **2013**, *29* (32), 10149–10158.

(15) Espinosa-Marzal, R. M.; Nalam, P. C.; Bolisetty, S.; Spencer, N. D. Impact of Solvation on Equilibrium Conformation of Polymer Brushes in Solvent Mixtures. *Soft Matter* **2013**, *9* (15), 4045.

(16) Rosenberg, K. J.; Goren, T.; Crockett, R.; Spencer, N. D. Load-Induced Transitions in the Lubricity of Adsorbed Poly(L-Lysine)- G-Dextran as a Function of Polysaccharide Chain Density. *ACS Appl. Mater. Interfaces* **2011**, *3* (8), 3020–3025.

(17) Perrino, C.; Lee, S.; Spencer, N. D. End-Grafted Sugar Chains as Aqueous Lubricant Additives: Synthesis and Macrotribological Tests of Poly(L-Lysine)-Graft-Dextran (PLL-G-Dex) Copolymers. *Tribol. Lett.* **2008**, *33* (2), 83–96.

(18) Irfachsyad, D.; Tildesley, D.; Malfreyt, P. Dissipative Particle Dynamics Simulation of Grafted Polymer Brushes Under Shear. *Phys. Chem. Chem. Phys.* **2002**, *4* (13), 3008–3015.

(19) Chen, M.; Briscoe, W. H.; Armes, S. P.; Klein, J. Lubrication at Physiological Pressures by Polyzwitterionic Brushes. *Science* **2009**, *323* (5922), 1698–1701.

(20) Klein, J.; Perahia, D.; Warburg, S. Forces Between Polymer-Bearing Surfaces Undergoing Shear. *Nature* **1991**.

(21) Grest, G. Interfacial Sliding of Polymer Brushes: a Molecular Dynamics Simulation. *Phys. Rev. Lett.* **1996**, *76* (26), 4979–4982.

(22) Galuschko, A.; Spirin, L.; Kreer, T.; Johner, A.; Pastorino, C.; Wittmer, J.; Baschnagel, J. Frictional Forces Between Strongly Compressed, Nonentangled Polymer Brushes: Molecular Dynamics Simulations and Scaling Theory. *Langmuir* **2010**, *26* (9), 6418–6429.

(23) Doyle, P. S.; Shaqfeh, E.; Gast, A. P. Rheology of Polymer Brushes: a Brownian Dynamics Study. *Macromolecules* **1998**, *31* (16), 5474–5486.

(24) Kröger, M. Simple Models for Complex Nonequilibrium Fluids. *Phys. Rep.* **2004**, *390* (6), 453–551.

(25) Grest, G. S. Normal and Shear Forces Between Polymer Brushes. *Adv. Polym. Sci.* **1999**, *138*, 149–183.

(26) Klein, J.; Kumacheva, E.; Mahaiu, D.; Perahia, D.; Fetters, L. J. Reduction of Frictional Forces Between Solid Surfaces Bearing Polymer Brushes. *Nature* **1994**, *370* (6491), 634–636.

(27) Klein, J.; Kumacheva, E.; Perahia, D.; Mahalu, D.; Warburg, S. Interfacial Sliding of Polymer-Bearing Surfaces. *Faraday Discuss.* **1994**, *98*, 173.

(28) Raviv, U.; Giasson, S.; Kampf, N.; Gohy, J.-F.; Jérôme, R.; Klein, J. Normal and Frictional Forces Between Surfaces Bearing Polyelectrolyte Brushes. *Langmuir* **2008**, *24* (16), 8678–8687.

(29) Schorr, P. A.; Kwan, T. C. B.; Kilbey, S. M.; Shaqfeh, E. S. G.; Tirrell, M. Shear Forces Between Tethered Polymer Chains as a Function of Compression, Sliding Velocity, and Solvent Quality. *Macromolecules* **2003**, *36* (2), 389–398.

(30) Li, A.; Benetti, E. M.; Tranchida, D.; Clasohm, J. N.; Schönherr, H.; Spencer, N. D. Surface-Grafted, Covalently Cross-Linked Hydrogel Brushes with Tunable Interfacial and Bulk Properties. *Macromolecules* **2011**, *44* (13), 5344–5351.

(31) Tsujii, Y.; Nomura, A.; Okayasu, K.; Gao, W.; Ohno, K.; Fukuda, T. AFM Studies on Microtribology of Concentrated Polymer Brushes in Solvents. *J Phys. Conf. Ser.* **2009**, *184* (1), 012031.

(32) Limpoco, F. T.; Advincula, R. C.; Perry, S. S. Solvent Dependent Friction Force Response of Polystyrene Brushes Prepared by Surface Initiated Polymerization. *Langmuir* **2007**, *23* (24), 12196–12201.

(33) Raviv, U.; Klein, J. Adhesion, Friction, and Lubrication Between Polymer-Bearing Surfaces. In *Polymer Science: A Comprehensive Reference*; Elsevier, 2012; pp 607–628.

(34) Klein, J. Interactions, Friction and Lubrication Between Polymer-Bearing Surfaces. In *Fundamentals of Tribology and Bridging the Gap Between the Macro- and Micro/Nanoscales*; Springer Netherlands: Dordrecht, 2001; pp 177–198.

(35) Klein, J. Shear, Friction, and Lubrication Forces Between Polymer-Bearing Surfaces. *Annu. Rev. Mater. Sci.* **1996**, *26* (1), 581–612.

(36) Nomura, A.; Okayasu, K.; Ohno, K.; Fukuda, T.; Tsujii, Y. Lubrication Mechanism of Concentrated Polymer Brushes in Solvents: Effect of Solvent Quality and Thereby Swelling State. *Macromolecules* **2011**, *44* (12), 5013–5019.

(37) Gong, J. P. Friction and Lubrication of Hydrogels?Its Richness and Complexity. *Soft Matter* **2006**, *2*, 544.

(38) Kim, S. H.; Opdahl, A.; Marmo, C.; Somorjai, G. A. AFM and SFG Studies of pHEMA-Based Hydrogel Contact Lens Surfaces in Saline Solution: Adhesion, Friction, and the Presence of Non-Crosslinked Polymer Chains at the Surface. *Biomaterials* **2002**, *23* (7), 1657–1666.

(39) Pan, Y.-S.; Xiong, D.-S.; Ma, R.-Y. A Study on the Friction Properties of Poly(Vinyl Alcohol) Hydrogel as Articular Cartilage Against Titanium Alloy. *Wear* **2006**, *262* (7), 1021–1025.

(40) Gong, J. P.; Higa, M.; Iwasaki, Y.; Katsuyama, Y.; Osada, Y. Friction of Gels. *Journal of Physical Chemistry B* **1997**, *101* (28), 5487–5489.

(41) Caravia, L.; Dowson, D.; Fisher, J.; Corkhill, P. H.; Tighe, B. J. Friction of Hydrogel and Polyurethane Elastic Layers When Sliding Against Each Other Under a Mixed Lubrication Regime. *Wear* **1995**, *181*, 236–240.

(42) Gong, J. P.; Kurokawa, T.; Narita, T.; Kagata, G.; Osada, Y.; Nishimura, G.; Kinjo, M. Synthesis of Hydrogels with Extremely Low Surface Friction. *J. Am. Chem. Soc.* **2001**, *123* (23), 5582–5583.

(43) Mamada, K.; Fridrici, V.; Kosukegawa, H.; Kapsa, P.; Ohta, M. Friction Properties of Poly(Vinyl Alcohol) Hydrogel: Effects of Degree of Polymerization and Saponification Value. *Tribol. Lett.* **2011**, *42* (2), 241–251.

(44) Bavaresco, V. P.; Zavaglia, C. A. C.; Reis, M. C.; Gomes, J. R. Study on the Tribological Properties of pHEMA Hydrogels for Use in Artificial Articular Cartilage. *Wear* **2008**, *265* (3-4), 269–277.

(45) Ohsedo, Y.; Takashina, R.; Gong, J. P.; Osada, Y. Surface Friction of Hydrogels with Well-Defined Polyelectrolyte Brushes. *Langmuir* **2004**, *20* (16), 6549–6555.

(46) Ishikawa, Y.; Hiratsuka, K.-I.; Sasada, T. Role of Water in the Lubrication of Hydrogel. *Wear* **2005**, *261* (5), 500–504.

(47) Alexander, S. Adsorption of Chain Molecules with a Polar Head a Scaling Description. *J. Phys-Paris* **1977**, *38* (8), 983–987.

(48) De Gennes, P. G. Conformations of Polymers Attached to an Interface. *Macromolecules* **1980**, *13* (5), 1069–1075.

(49) Semenov, A. N. *Soviet Phys*; JETP, 1985.

(50) Milner, S. T.; Witten, T. A.; Cates, M. E. Theory of the Grafted Polymer Brush. *Macromolecules* **1988**, *21* (8), 2610–2619.

(51) Zhulina, Y. B.; Pryamitsyn, V. A.; Borisov, O. V. Structure and Conformational Transitions in Grafted Polymer Chain Layers. a New Theory. *Polymer Science U.S.S.R.* **1989**, *31* (1), 205–216.

(52) Binder, K.; Müller, M. Monte Carlo Simulation of Block Copolymers. *Curr. Opin. Colloid Interface Sci.* **2000**, *5* (5-6), 315–323.

(53) Hsu, H.-P.; Paul, W. A Fast Monte Carlo Algorithm for Studying Bottle-Brush Polymers. *Comput. Phys. Commun.* **2011**, *182* (10), 2115–2121.

(54) Binder, K.; Müller, M.; Schmid, F.; Werner, A. Interfaces in Partly Compatible Polymer Mixtures: a Monte-Carlo Simulation Approach. *Physica A* **1998**, *249* (1-4), 293–300.

(55) Grest, G. S. Computer Simulations of Shear and Friction Between Polymer Brushes. *Curr. Opin. Colloid Interface Sci.* **1997**, *2* (3), 271–277.

(56) Hoy, R. S.; Grest, G. S. Entanglements of an End-Grafted Polymer Brush in a Polymeric Matrix. *Macromolecules* **2007**, *40* (23), 8389–8395.

(57) Murat, M.; Grest, G. S. Molecular Dynamics Simulations of the Force Between a Polymer Brush and an AFM Tip. *Macromolecules* **1996**, *29* (25), 8282–8284.

(58) Singh, M. K.; Ilg, P.; Espinosa-Marzal, R. M.; Kröger, M.; Spencer, N. D. Polymer Brushes Under Shear: Molecular Dynamics Simulations Compared to Experiments. *Langmuir* **2015**, *31* (16), 4798–4805.

(59) Goujon, F.; Ghoufi, A.; Malfreyt, P.; Tildesley, D. J. The Kinetic Friction Coefficient of Neutral and Charged Polymer Brushes. *Soft Matter* **2013**, *9* (10), 2966.

(60) Carrillo, J.-M. Y.; Brown, W. M.; Dobrynin, A. V. Explicit Solvent Simulations of Friction Between Brush Layers of Charged and Neutral Bottle-Brush Macromolecules. *Macromolecules* **2012**, *45* (21), 8880–8891.

(61) Elliott, I. G.; Kuhl, T. L.; Faller, R. Compression of High Grafting Density Opposing Polymer Brushes Using Molecular Dynamics Simulations in Explicit Solvent. *J. Phys. Chem. B* **2013**, *117* (15), 4134–4141.

(62) Jentzsch, C.; Sommer, J.-U. Polymer Brushes in Explicit Poor Solvents Studied Using a New Variant of the Bond Fluctuation Model. *J. Chem. Phys.* **2014**, *141* (10), 104908.

(63) Grest, G. S. Grafted Polymer Brushes: a Constant Surface Pressure Molecular Dynamics Simulation. *Macromolecules* **1994**, *27* (2), 418–426.

(64) Kreer, T.; Binder, K.; Müser, M. H. Friction Between Polymer Brushes in Good Solvent Conditions: Steady-State Sliding Versus Transient Behavior. *Langmuir* **2003**, *19* (18), 7551–7559.

(65) Kreer, T.; Müser, M. H.; Binder, K.; Klein, J. Frictional Drag Mechanisms Between Polymer-Bearing Surfaces. *Langmuir* **2001**, *17* (25), 7804–7813.

(66) Kreer, T.; Müser, M. H. On the Tribology and Rheology of Polymer Brushes in Good Solvent Conditions: a Molecular Dynamics Study. *Wear* **2003**, *254* (9), 827–831.

(67) de Beer, S.; Müser, M. H. Alternative Dissipation Mechanisms and the Effect of the Solvent in Friction Between Polymer Brushes on Rough Surfaces. *Soft Matter* **2013**, *9* (30), 7234.

(68) Dimitrov, D. I.; Milchev, A.; Binder, K. Polymer Brushes in Solvents of Variable Quality: Molecular Dynamics Simulations Using Explicit Solvent. *J. Chem. Phys.* **2007**, *127* (8), 084905.

(69) Galuschko, A. *Molecular Dynamics Simulations of Sheared Polymer Brushes*; 2010.

(70) Pastorino, C.; Kreer, T.; Müller, M.; Binder, K. Comparison of Dissipative Particle Dynamics and Langevin Thermostats for Out-of-Equilibrium Simulations of Polymeric Systems. *Phys. Rev. E* **2007**, *76* (2), 026706.

(71) Chen, J.; Zhou, S.-M.; Ma, B.-G.; Zhang, L.-M.; Yi, J.-Z. Molecular Dynamics Simulations on Dextran Hydrogels. *E-Polymers* **2013**, *13* (1).

(72) Walter, J.; Sehrt, J.; Vrabec, J.; Hasse, H. Molecular Dynamics and Experimental Study of Conformation Change of Poly(N-Isopropylacrylamide) Hydrogels in Mixtures of Water and Methanol. *J. Phys. Chem. B* **2012**, *116* (17), 5251–5259.

(73) Tönsing, T.; Oldiges, C. Molecular Dynamic Simulation Study on Structure of Water in Crosslinked Poly(N-Isopropylacrylamide) Hydrogels. *Phys. Chem. Chem. Phys.* **2001**, *3* (24), 5542–5549.

(74) Hoffmann, M.; Lang, M.; Sommer, J.-U. Gelation Threshold of Cross-Linked Polymer Brushes. *Phys. Rev. E* **2011**, *83* (2), 021803.

(75) Ou, X.; Han, Q.; Dai, H.-H.; Wang, J. Molecular Dynamic Simulations of the Water Absorbency of Hydrogels. *J Mol Model* **2015**, *21* (9), 231–10.

Chapter 2

Materials and Methods

2.1 Materials

The friction experiments were performed in dimethylformamide (DMF) on hydrophobic polymer brushes (poly(lauryl methacrylate)) in hexadecane and hydrophilic brushes (poly(glycidyl methacrylate)) synthesized by Chengjun Kang, a PhD student involved in this project. For the sake of completeness, I am reproducing here a brief description of the synthesis process, as also presented in Chengjun Kang's PhD thesis. The polymers were synthesized using the surface-initiated atom-transfer radical polymerization[1] (SI-ATRP) method on a silicon surface.

2.1.1 Hydrophobic Brushes

The detail of synthesis method for poly(lauryl methacrylate) on a Si wafer substrate can be found in the published work[2] of Kang et. al. The polymerization reactions were carried out in a Schlenk line under a nitrogen atmosphere. In the experiment, dNbpy (1.9 mmol, 0.8 g) and CuBr2/(dNbpy)2 complexes (0.05 mmol) in 550 μL of DMF were first dissolved in lauryl methacrylate (50 mL, 0.17 mol), after which the solution underwent three freeze−pump−thaw circles (10 min each) to remove the dissolved oxygen. Then the mixture was transferred to another flask containing CuBr (0.95 mmol, 0.14 g). After stirring for 30 min at room temperature, 75 μL of EBiB/monomer solution (0.1% v/v) was added to the clear dark solution, and the mixture was immediately transferred to freshly prepared, initiator-modified samples. Polymerization was carried out at 110 °C for various lengths of time (see the published paper for details), and subsequently the reaction was quenched by

precipitation in methanol, the wafer being subsequently sonicated in toluene to remove physisorbed polymers.

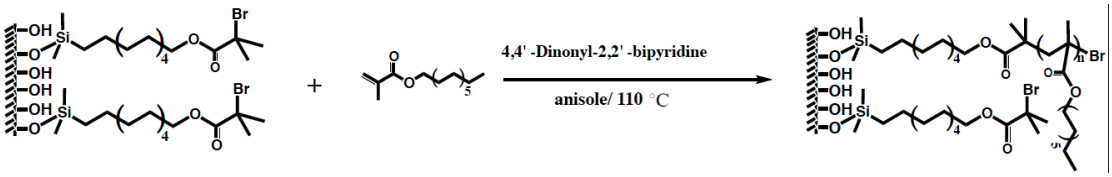

Figure 2.1: Schematic of polymer-brush synthesis using ATRP technique

2.1.2 Hydrophilic Brushes

The typical procedures for SI-ATRP of glycidyl methacrylate (GMA) were as follows: 0.141g (0.9 mmol) bipyridine (bpy) was dissolved in a solution of 5 ml GMA (0.037mol), 1ml H_2O and 4ml methanol. The mixture underwent four freeze-pump-thaw circles (15 min each) to remove dissolved oxygen. Then the mixture was transferred to another flask containing 52.8 mg CuBr (0.37 mmol) and 4.5 mg $CuBr_2$ (0.02 mmol). After stirring for 10 min at room temperature, the mixture was immediately transferred to freshly prepared, initiator-modified silicon substrates. Polymerization was carried out at room temperature for various lengths of time without stirring, after which the silicon substrates were removed from the polymerization solution, and sonicated in DMF to remove weakly adsorbed polymer. PGMA brushes were cross-linked by ethane-1,2-diamine or ethane-1,6-diamine in a post-modification manner The reaction between crosslinkers and PGMA could have four different possibilities, with different thickness increments expected owing to the different amount of cross-linker added to the PGMA brushes (discussed in **Appendix II**). The cross-linking of PGMA brushes was performed as in case (b) out of four possibilities discussed.

Crosslinkers of two different lengths were used to prepare PGMA gels with different degrees of crosslinking to facilitate the study of the effect of length and degree of crosslinking on tribological behaviour of the gels.

Table 2.1: Table showing crosslinkers used in preparing PGMA gels:

Crosslinkers	Referred in the thesis as:
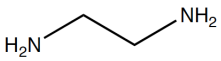 ethane-1,2-diamine	Crosslinkers of length C_2
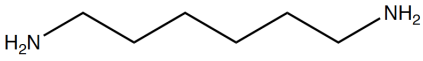 hexane-1,6-diamine	Crosslinkers of length C_6

2.2 Methods

2.2.1 Friction Force Microscopy

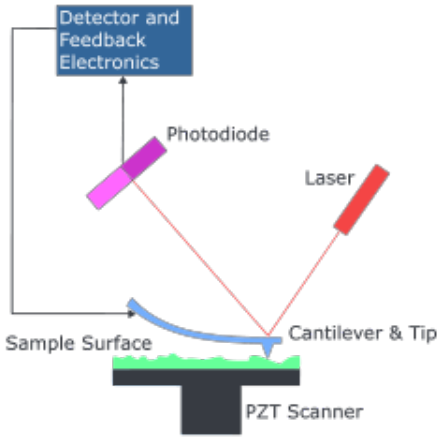

Figure 2.2: Schematic showing working principle of an AFM (hank.uoregon.edu)

Atomic force microscopy is a powerful tool allowing a variety of surfaces to be imaged and characterized at the nano and micro scales. It is one of the types of scanning probe microscopy (SPM), the first being scanning tunnelling microscopy (STM), which Binning and Rohrer developed in the early 1980s at IBM, Zurich. The

invention of the AFM provided the scientific community with a new and unique instrument that led to many further advancements in science and technology[3,4].

In AFM, a very sharp tip (generally of dia. 10-100 nm) is brought in contact with the sample surface. The interaction between the tip and surface is monitored as the tip scans the sample surface in the x-y direction. AFM relies on feedback mechanisms that enable piezo-electric scanners to maintain the cantilever at a constant deflection (generally due to the cantilever pressing the tip onto the surface). A laser beam is reflected from the back and reflective side of the cantilever to a four-quadrant photo detector while scanning the surface of the sample. The position-sensitive photo-detector (PSD) measures the difference in the light intensities between the upper and the lower photo-detector quadrants (Figure 2.3(b)) and converts intensity signal to voltage.

AFM has been predominantly used for imaging but it can be used in friction force microscopy (FFM) or lateral force microscopy (LFM) [5-8] also. AFM is operated under contact mode in LFM, the lateral and normal movements of cantilever are detected using the laser beam, which is reflected off the rear of cantilever and recorded using the 4-quadrant photo-diode. These normal and lateral movements of cantilever can be converted to normal and lateral forces acting between the cantilever-tip and sample surface if stiffness of the cantilever and sensitivity of photo detector with respect to cantilever position in the respective direction is known. All the frictional measurements are performed using the MFP 3D Instrument (Asylum Inc, Santa Barbara, USA).

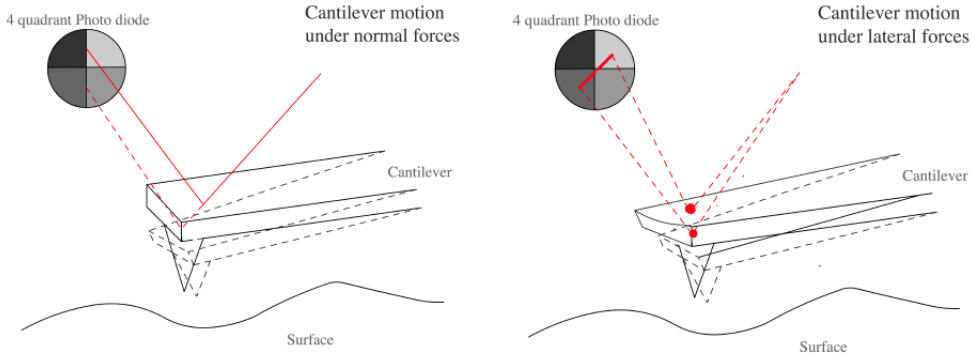

Figure 2.3: Schematic representation of the movement of AFM cantilevers in normal and lateral mode[9].

Friction loops at a given load are obtained by laterally scanning the tip on the surface as represented in Figure 2.4. The slow-scan axis was disabled while obtaining the friction loops. During forward scan the 'trace' (T) and backward scan the 'retrace' (R) of the loop are recorded. The average between trace and retrace voltages represents the frictional force of the underlying surface. The calibration method is explained below.

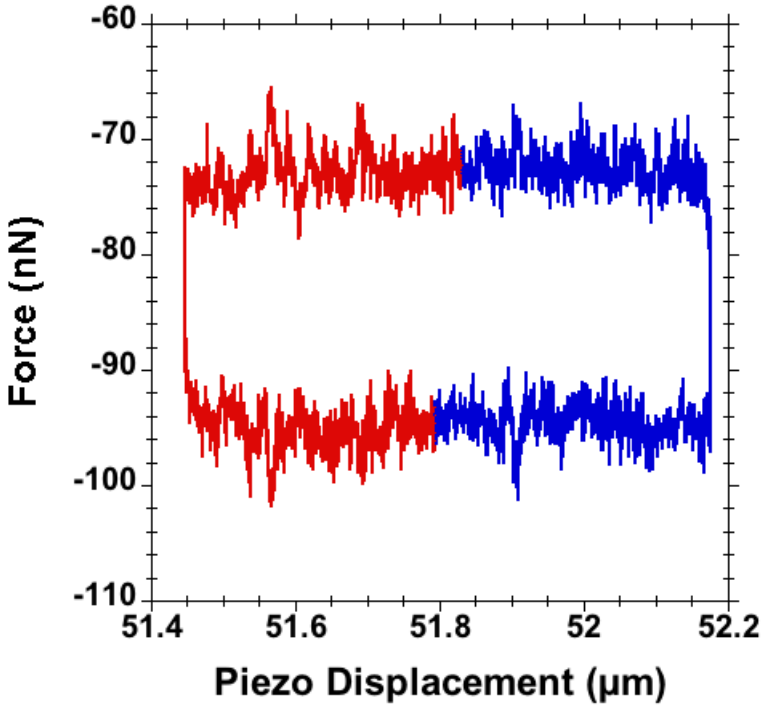

Figure 2.4: The friction loop obtained for bare-silica surface in HEPES showing trace and retrace curves.

2.2.2 Colloidal-probe Microscopy

In colloidal-probe microscopy, a commonly used AFM technique, a colloidal sphere is attached to the free end of an AFM cantilever[10]. The colloidal probe has many advantages as follows.

- It provides a well-defined contact geometry at the interface.
- It helps to reduce contact pressures by distributing the load over a larger contact area. Low contact pressures obtained at the interface due to colloidal-probe attachment minimize the wear of the sample at the interface while conducting frictional measurements.
- It is easy to functionalize colloidal probes with surfactants or polymers[11].

A homebuilt micromanipulator (BX 41, Olympus microscope, Japan) was used to attach the colloid particles to the cantilever. In the current study, silica microspheres (Kromasil, EKA Chemicals, Sweden) and polyethylene microspheres (Kobo Products, Inc. South Plainfield, N.J., USA) with a mean diameter = 10-15 μm were stuck to different tipless cantilevers using a UV-glue (NOA 61, Norland Optical adhesive, Cranbury, NJ) and were cured overnight using a UV lamp (9W, Panacol-E losol). The CSC12 (MicrosMasch, Tallinn, Estonia) and NSC36 (MicrosMasch, Tallinn, Estonia) tipless cantilevers were used for the experiments and are specified in Table 2.2 in the later section for each experiment.

2.2.3 Force-Distance Curves

Force-distance curves **(Figure 2.5)**[12,13] provide a measure of interactions between tip and the underlying surface. The cantilever deflection (d) is a function of the tip position along the Z-axis and is converted into a normal force by Hooke's law:

$$F = k_N \times d \qquad 2.1$$

where k_N is the normal stiffness of the cantilever (see section for calibration of normal forces).

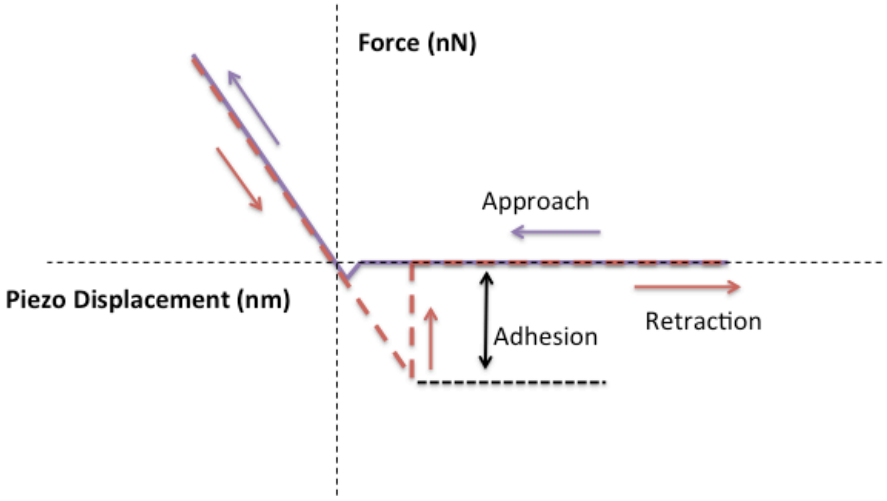

Figure 2.5: Representative curve of pull-off force measurements.

The force-curve data during approach can be used as applied force against penetration depth with appropriate modifications (as shown in the following equations). Further, the elastic modulus can be calculated using the Hertz model (when no adhesion is observed) for a sphere on plane[14]:

$$F = \frac{4}{3}\frac{\sqrt{r_{tip}}}{1-\nu^2} E\, \delta^{3/2} \qquad 2.2$$

$$\delta = z - d \qquad 2.3$$

where F is the applied load, r_{tip} is the radius of the colloidal probe, ν is the Poisson's ratio of the polymer films (taken as 0.5), E the apparent Young's modulus of polymer films and δ is the indentation-depth of the polymer films (calculated from the relative piezosensor position (z) and relative deflection of the cantilever (d)). The approach-speed of the cantilever to the polymer-bearing surface is maintained constant for all the experiments.

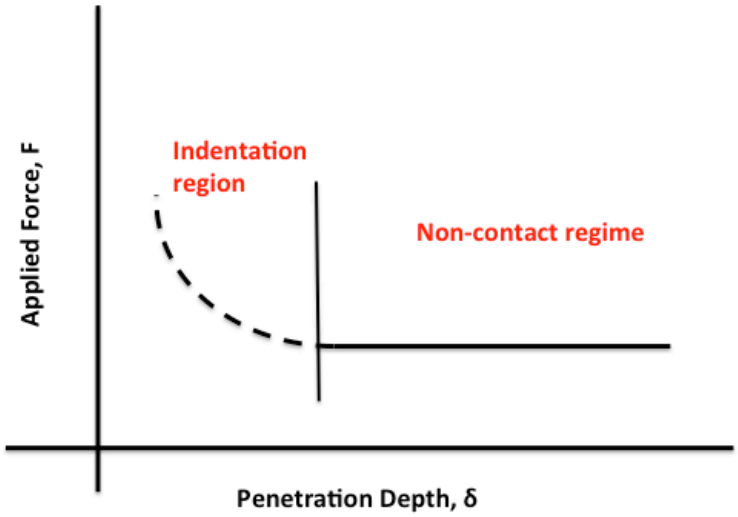

Figure 2.6: Representative curve for indentation experiments using AFM.

To exclude any substrate effects, the Hertz model was fitted to the first 10% of the force-indentation curves (obtained by modifying force-distance curve using equations 2.1-2.3) to calculate the Young's modulus of polymers in solvent[15]. These experiments were performed for PGMA brushes and gels in DMF.

2.2.4 Calibrating Normal and Lateral Forces in AFM

The photo-detector output voltage must be converted to force using a suitable calibration method in order to quantify the normal and lateral forces experienced between the tip and the sample. Several calibration procedures have been used in the literature to accurately estimate the stiffness and the deflection sensitivities, both in normal and lateral modes, for the given tip and sample system[16,17]. Here I describe, in brief, the calibration procedures for normal and lateral forces, used in this thesis.

2.2.5 Calibration of Normal forces

A non-destructive calibration procedure to estimate the normal stiffness of the cantilever is the thermal-noise method[18]. A harmonic oscillator in equilibrium fluctuates due to the surrounding thermal noise. The equi-partition theorem

establishes the relationship between the measured deflection signal of the AFM cantilever due to thermal noise and the spring constant of the cantilever.

$$\langle \frac{1}{2} m\omega_0^2 q^2 \rangle = \frac{1}{2} k_B T \quad (2.4)$$

$$\omega_0^2 = \frac{k_N}{m} \quad (2.5)$$

$$k_N = \frac{k_B T}{\langle q^2 \rangle} \quad (2.6)$$

where k_N is the normal stiffness of the cantilever, k_B the Boltzmann constant, T the temperature and $\langle q^2 \rangle$ is the mean-square displacement of the cantilever in normal mode.

Fluctuations in the displacement of the cantilever are obtained as a function of frequency (power spectra) to estimate the mean-squared displacement of the cantilever. While measuring the power spectra (chamber is isolated from the electronic and external noise), the background noise from the instrument is kept to a minimum. The measured voltage is converted into tip displacement by the normal deflection sensitivity of the cantilever, S_N (in volt/vertical distance). The latter is estimated by measuring a force-distance curve on a hard substrate and only on bare surfaces. The measurement of the piezo response as a function of cantilever displacement is performed when the tip is in contact with the sample. Deflection sensitivity is a function of laser intensity, PSD sensitivity and geometry of the optical setup. The refractive index of the medium changes with the medium and hence affects the intensity of the laser on the photodiode. Therefore, the deflection sensitivity for each solvent must be obtained. Finally, using the following equation the normal force can be estimated:

$$F_N = \frac{k_N}{S_N} \Delta V_N \quad (2.7)$$

where ΔV_N is the measured or applied set-point voltage (in volts) and F_N is the corresponding calibrated normal force (in Newtons).

2.2.6 Calibration of Lateral Forces

In order to convert the photo-diode response into a lateral or frictional force, the lateral stiffness of the cantilever and the lateral sensitivity due the torsional movement of the cantilever are determined, similar to normal force calibration. Sader's method[19] was used to calibrate the torsional spring constant of the cantilever k_φ, where the unloaded radial resonant frequency (ω_t) and the quality factor (Q_t) due to torsional vibrations of the cantilever are calculated by obtaining a power spectrum in torsional mode[20] (using crosspoint panel and changing Infast to lateral in Assylum AFM) . The thickness of at least one cantilever per batch was determined with the help of a scanning electron microscope. The torsional spring constant was obtained using Sader's equation for torsional mode:

$$k_\phi = 0.1592\rho b^4 L Q_t \omega_t^2 \Gamma_i^t(\omega_t) \qquad 2.8$$

where k_ϕ is the torsional spring constant, ρ the density of the fluid, L and b the dimensions of the cantilever and Γ is a hydrodynamic function and is the dependent on the viscosity of the fluid (η).

The lateral sensitivity S_L of the AFM cantilever was estimated using the 'test-probe' method[21] as described by Cannara et. al. In this method, a colloidal sphere is attached to the cantilever used for calibration, referred to as the 'test-cantilever'. The 'test-cantilever' is of similar width and thickness as the cantilever used for measurements or the 'target-cantilever'. The diameter of the colloidal sphere used for the test cantilever is larger than the width of the cantilever. The lateral signal sensitivity of the test cantilever is calibrated by obtaining 'lateral' force curves through lateral loading

of the colloidal sphere against a vertical sidewall (figure 2.7). A silica wafer is cut along its crystal plane <100> and is used as a wall to obtain lateral force curves. While obtaining the lateral force curves, the height of the piezo (or the cantilever) was adjusted to twist the cantilever against the wall at the center of the colloid and to avoid tipping off of the cantilever over the edge of the wall.

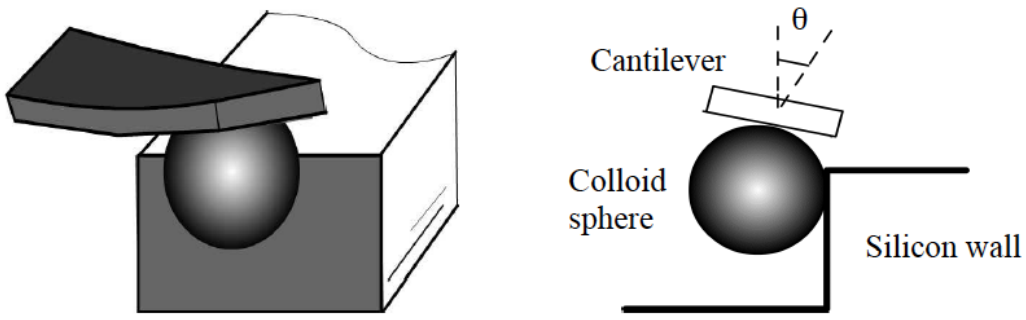

Figure 2.7: Schematic representation of obtaining lateral forces curves with a colloid probe to estimate the lateral deflection sensitivity[8,9].

The obtained lateral force curve and the corresponding torsional sensitivity due to the angular twist in the cantilever is depicted in figure 2.8. Subsequently, the lateral sensitivity for the target cantilever is corrected for the tip length, total signal strength, and in- plane bending of the cantilever[21].

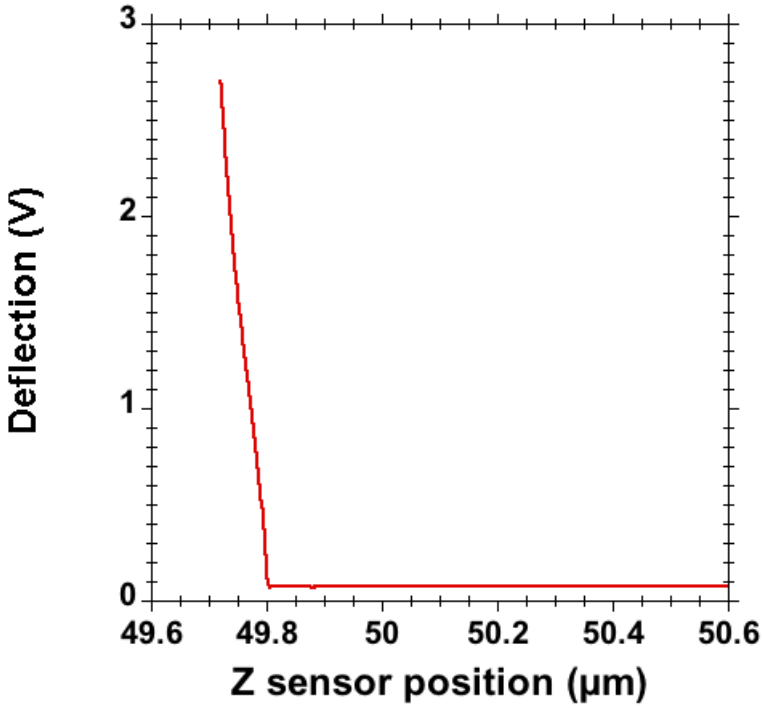

Figure 2.8: The lateral force curve obtained for a bare silica sphere against a silica wall in air.

In this work, the lateral-deflection sensitivities were obtained for different cantilevers used in the experiments. Both test and target cantilevers were tipless rectangular cantilevers from the same manufacturing batch for each set of experiments. Length and width of the cantilever and the diameter of the sphere were measured with an optical microscope with a 20X magnification zoom (AXIOXAM, Zeiss, US).

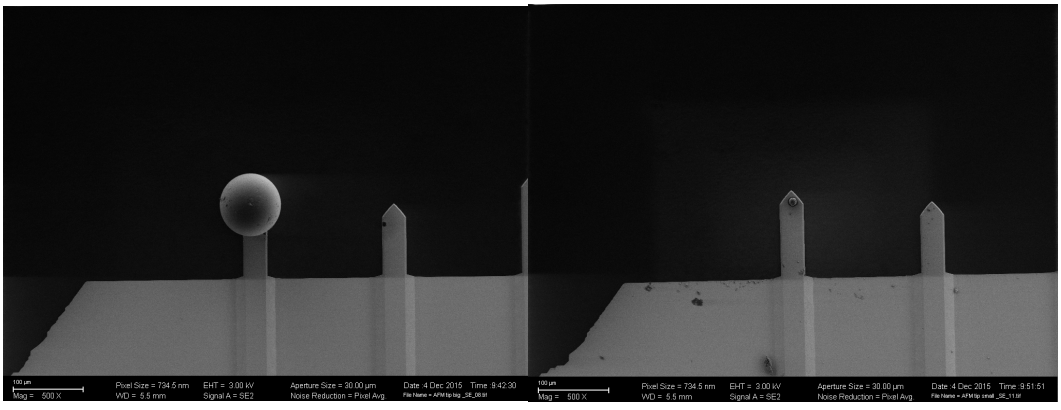

Figure 2.9: SEM images of the NSC 36 AFM cantilevers (a) for the test probe (silica sphere dia. 87 µm) (b) for the target probe (silica sphere dia 14 µm).

The lateral forces (F_L) were estimated using the obtained lateral sensitivity (S_L) and torsional stiffness (k_φ) values using the following equation:

$$F_L = \alpha \Delta V_L \quad (2.9)$$

$$\alpha = \frac{k'_{lat}}{S_L} \quad (2.10)$$

$$k'_{lat} = \frac{k_\phi}{h^2}\left(\frac{L}{L'}\right) \quad (2.11)$$

where α is the lateral calibration factor and h is the torsional arm length (diameter of the colloid thickness of the cantilever) and the factor (L/L') accounts for the fact that the forces in the experiment are applied at the tip position and not at the end of the cantilever.

2.2.7 Experimental Protocol

1. The width and the length of the tipless cantilever are measured using an optical microscope and the thickness of at least one cantilever from the batch is determined using a scanning electron microscope.

2. Force-distance curves are obtained on hard surfaces (bare silicon wafer) before attaching the colloidal probe. The normal stiffness of the cantilever is estimated from the deflection sensitivity in the normal direction.

3. The tipless cantilevers are calibrated using the thermal excitation method. Resonant frequencies and half-width (Q factor) are determined for both normal and lateral excitation modes. The torsional spring constant is obtained according to Sader's method (http://www.ampc.ms.unimelb.edu.au/afm/calibration.html).

4. The normal stiffness obtained by thermal excitation method is compared with that obtained using Sader's method.

5. The colloid is attached to the tipless cantilever (target probe cantilever).

6. Another colloid having a diameter larger than the width of the cantilever is attached to the test probe cantilever.

7. As described in the last section, the lateral sensitivity S_L was determined by taking lateral force curves against the silica wall using the test probe cantilever. The corresponding photodiode signal (SUM) was also recorded.

8. Lateral calibration constants α were obtained after applying all corrections as described in reference[21].

9. Load-dependence studies: The friction loops are measured for bare and polymer-covered surfaces at different loads keeping the speed constant for each of the polymer brushes and gels mentioned in the section 2.1.

The SUM and the deflection sensitivity (on a bare surface) for each solvent (with colloid sphere) are recorded to calibrate the force measurements later. The samples with polymer brushes are assumed to be laterally homogenous. After the beginning of the experiment, care is taken that the laser position is not altered.

Table 2.2: Table showing different materials and methods used in this thesis:

<table>
<tr><th colspan="2">Materials
(Dry Thickness in nm)</th><th>Solvent</th><th>Cantilever used
(Stiffness in N/m)</th><th>Colloidal Sphere</th><th>Diameter (µm)</th></tr>
<tr><td colspan="2">PLMA
(265 nm and 345 nm)</td><td rowspan="2">Hexadecane</td><td>CSC12
0.075</td><td>PE</td><td>5</td></tr>
<tr><td colspan="2"></td><td>CSC12
0.08</td><td>SiO_2</td><td>6</td></tr>
<tr><td colspan="2">PGMA
(93 nm)</td><td rowspan="7">Dimethyl Formamide (DMF)</td><td rowspan="7">NSC36
0.976</td><td rowspan="7">SiO_2</td><td rowspan="7">7</td></tr>
<tr><td rowspan="3">PGMA Gel (C_2)</td><td>5%
(94 nm)</td></tr>
<tr><td>15%
(96 nm)</td></tr>
<tr><td>50%
(102 nm)</td></tr>
<tr><td rowspan="3">PGMA Gel (C_6)</td><td>3%
(94.5 nm)</td></tr>
<tr><td>18%
(100 nm)</td></tr>
<tr><td>36%
(107 nm)</td></tr>
</table>

C_2 and C_6 are used to express length of crosslinking chains having 2 Carbon and 6 Carbon chains respectively,

5, 15, 50, 3, 18 and 36 % express degree of crosslinking of the polymer brushes

2.3 References

(1) Huang, X. Y.; Wirth, M. J. Surface-Initiated Radical Polymerization on Porous Silica. *Analytical Chemistry* **1997**, *69* (22), 4577–4580.

(2) Kang, C.; Crockett, R. M.; Spencer, N. D. Molecular-Weight Determination of Polymer Brushes Generated by SI-ATRP on Flat Surfaces. *Macromolecules* **2014**, *47* (1), 269–275.

(3) BINNIG, G.; QUATE, C. F.; GERBER, C. Atomic Force Microscope. *Phys. Rev. Lett.* **1986**, *56* (9), 930–933.

(4) BINNIG, G.; GERBER, C.; STOLL, E.; ALBRECHT, T. R.; QUATE, C. F. Atomic Resolution with Atomic Force Microscope. *Europhys. Lett.* **1987**, *3* (12), 1281–1286.

(5) Perry, S. S. Scanning Probe Microscopy Measurements of Friction. *MRS Bull.* **2011**, *29* (07), 478–483.

(6) Carpick, R. W.; Salmeron, M. Scratching the Surface: Fundamental Investigations of Tribology with Atomic Force Microscopy. *Chemical Reviews* **1997**, *97* (4), 1163–1194.

(7) Nalam, P. C.; Ramakrishna, S. N.; Espinosa-Marzal, R. M.; Spencer, N. D. Exploring Lubrication Regimes at the Nanoscale: Nanotribological Characterization of Silica and Polymer Brushes in Viscous Solvents. *Langmuir* **2013**, *29* (32), 10149–10158.

(8) Ramakrishna, S. N. *Adhesion and Tribology on Well-Defined, Nano-Scale Rough Surfaces: a Gradient Approach*; 2013.

(9) Nalam, P. C. *Polymer Brushes in Aqueous Solvent Mixtures: Impact of Polymer Conformation on Tribological Properties*; 2012.

(10) DUCKER, W. A.; SENDEN, T. J.; PASHLEY, R. M. Direct Measurement of Colloidal Forces Using an Atomic Force Microscope. *Nature* **1991**, *353* (6341), 239–241.

(11) Pasche, S.; Textor, M.; Meagher, L.; Spencer, N. D.; Griesser, H. J. Relationship Between Interfacial Forces Measured by Colloid-Probe Atomic Force Microscopy and Protein Resistance of Poly(Ethylene Glycol)-Grafted Poly(L-Lysine) Adlayers on Niobia Surfaces. *Langmuir* **2005**, *21* (14), 6508–6520.

(12) Cappella, B.; Dietler, G. Force-Distance Curves by Atomic Force Microscopy. *Surface Science Reports* **1999**, *34* (1-3), 1–.

(13) DUCKER, W. A.; SENDEN, T. J.; PASHLEY, R. M. Measurement of Forces in Liquids Using a Force Microscope. *Langmuir* **1992**, *8* (7), 1831–1836.

(14) Sui, X.; Chen, Q.; Hempenius, M. A.; Vancso, G. J. Probing the Collapse Dynamics of Poly(N-Isopropylacrylamide) Brushes by AFM: Effects of Co-Nonsolvency and Grafting Densities. *Small* **2011**, *7* (10), 1440–1447.

(15) Li, A. *Structure-Property Relationships of Surface-Grafted Polymeric Architectures: From Ultra-Thin Films to Quasi-3D Polymer Assemblies*; 2013.

(16) Ogletree, D. F.; Carpick, R. W.; Salmeron, M. Calibration of Frictional Forces in Atomic Force Microscopy. *Rev. Sci. Instrum.* **1996**, *67* (9), 3298–3306.

(17) Palacio, M. L. B.; Bhushan, B. Normal and Lateral Force Calibration Techniques for AFM Cantilevers. *Critical Reviews in Solid State and Materials Sciences* **2010**, *35* (2), 73–104.

(18) HUTTER, J. L.; BECHHOEFER, J. Calibration of Atomic-Force Microscope Tips. *Rev. Sci. Instrum.* **1993**, *64* (7), 1868–1873.

(19) Sader, J. E.; Chon, J. W. M.; Mulvaney, P. Calibration of Rectangular Atomic Force Microscope Cantilevers. *Rev. Sci. Instrum.* **1999**, *70* (1), 3967–3969.

(20) Green, C. P.; Lioe, H.; Cleveland, J. P.; Proksch, R.; Mulvaney, P.; Sader, J. E. Normal and Torsional Spring Constants of Atomic Force Microscope Cantilevers. *Rev. Sci. Instrum.* **2004**, *75* (6), 1988–1996.

(21) Cannara, R. J.; Eglin, M.; Carpick, R. W. Lateral Force Calibration in Atomic Force Microscopy: a New Lateral Force Calibration Method and General Guidelines for Optimization. *Rev. Sci. Instrum.* **2006**, *77* (5).

Chapter 3

Experimental Results and Discussions

In this chapter the experimental results of colloidal-probe lateral force microscopy (LFM) experiments[1-4] on PLMA brushes and PGMA brushes are discussed. The friction forces were measured at constant speed and varying normal loads. This chapter also contains the results for AFM-based nanoindentation experiments[5-7] on PGMA brushes and gels in DMF. The synthesis protocol was described in **Chapter 2**. All the experiments with bare silica surfaces and polymer-grafted surfaces were performed with a bare microsphere countersurface. Asymmetric contact (i.e. brush against bare microsphere) was used, in order to obtain a measurable friction value, because friction in symmetric contact (brush-against-brush contact system) is at the limit of the resolution of LFM measurements.

3.1 PLMA Brushes in Hexadecane

3.1.1 Colloidal-Probe Lateral Force Microscopy

Tribological experiments on PLMA brushes in hexadecane were carried out using polyethylene (PE) and silica (SiO_2) spheres using colloidal-probe-based lateral force microscopy experiments to replicate soft-against-soft and hard-against-soft contact at the interface. The sliding surfaces in nature (e.g. digestive system, eyes, articulating joints, etc.) are all soft. Traditionally, hard probes are used in tribological experiments, also when measuring the friction of soft materials.

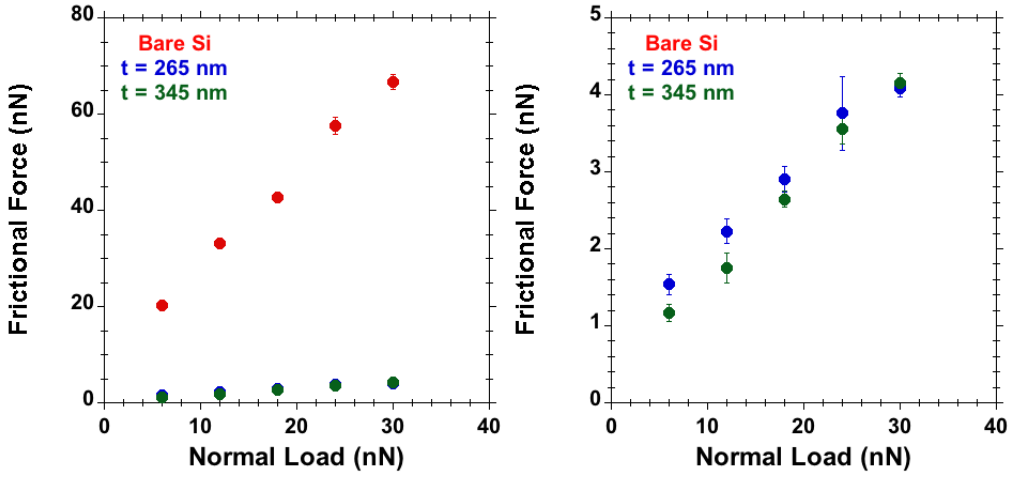

(a) (b)

Figure 3.1: Friction force against normal load from colloidal-probe lateral force microscopy experiments at 4 µm/sec with tipless cantilever (0.075 N/m stiffness) equipped with a polyethylene (PE) colloid sphere of 10 µm diameter (a) Friction force vs normal load for bare silicon surfaces with surface-grafted PLMA brushes of different thicknesses in hexadecane (b) Friction force vs normal load for PMLA brushes on silicon surfaces of different thicknesses in hexadecane

Figure 3.1 shows the friction force between a polyethylene colloidal sphere and surface-grafted PLMA brushes in hexadecane as a function of the load. The experiments were carried out at a constant speed of 4 µm/sec. In Figure 3.1(a), it can be clearly seen that the presence of polymer brushes on silicon surfaces reduces friction when compared to bare silicon surfaces in hexadecane solvent. Polymer brushes are known to reduce friction in a good solvent. A strong entropic repulsive force prevents interdigitation of polymer chains even at high compressions, enabling the development of a thin fluid film between opposing brushes[8]. This thin fluid film assists in reducing friction at the interface. In Figure 3.1(b) the friction force vs load curves for PLMA brushes of different thicknesses are presented. Friction force is found to be decreasing with increase in brush thickness at all normal loads applied.

Figure 3.2 shows the load-dependent friction force between a silica sphere and surface-grafted PLMA brushes in hexadecane. The experiments were performed at a speed of 4 µm/sec. In Figure 3.2(a), it can be seen that silicon surfaces bearing PLMA brushes lead to lower friction when compared to bare silicon surfaces—similar to the

results obtained with a polyethylene colloidal sphere. A small decrease in friction force was observed with increasing brush thickness at all the normal loads, except at 18 nN load.

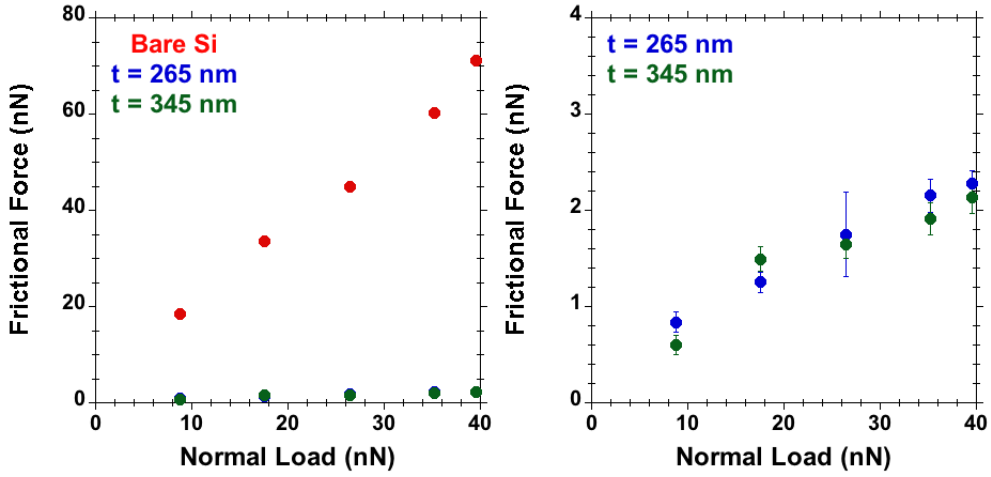

(a) **(b)**

Figure 3.2: Friction force against normal load from colloidal-probe lateral force microscopy experiments at 4 µm/sec with tipless cantilever (0.075 N/m stiffness) with a silica colloid sphere of 12 µm diameter (a) Comparison of results for bare silicon surfaces with surface-grafted PLMA brushes of different thicknesses in hexadecane (b) Comparison of results of PMLA brushes on silicon surfaces of different thicknesses in hexadecane

The extrapolation of friction force against normal load shows a deviation from Amontons' law, as a non-zero friction force is observed at zero normal loads. This is because of adhesion between the polymer brushes and microsphere. The observed friction force can be expressed as:

$$F = F_0 + \mu L \qquad 3.1$$

where F is friction force, µ is coefficient of friction, L is applied normal load and F_0 is the friction force at 0 normal load or adhesion force and depends upon the area of contact[9].

PLMA polymer brushes exhibited higher adhesion with the polyethylene colloidal sphere in comparison to the silica colloidal sphere.

Table 3.1: Coefficients of friction for different combinations of PLMA brush thicknesses and probe spheres.

PLMA brush thickness	PE Colloidal Sphere	SiO_2 Colloidal Sphere
265 nm	0.11	0.048
345 nm	0.13	0.044

Table 3.1 shows the coefficient of friction for PLMA brushes of different thicknesses in hexadecane for different colloidal-sphere countersurfaces. Coefficients of friction were calculated from the slope of the friction force vs normal load curves. The soft-against-soft combination of PLMA brushes against PE spheres shows a higher coefficient of friction than the soft-against-hard contact of PLMA brushes against SiO_2 spheres in hexadecane.

3.2 PGMA Brushes and Gels in DMF

3.2.1 Colloidal-Probe Lateral Force Microscopy

Figure 3.3 (a) and (b) shows the friction force against normal load for PGMA brushes and gels (crosslinked brushes) in DMF at 1 μm/sec and 5 μm/sec respectively and are compared with the corresponding results for a bare silicon surface. The crosslinkers are C_2 chains long and have different degrees of crosslinking. PGMA brushes on silicon surfaces in DMF reduce friction significantly when compared to bare silicon surfaces. The friction is found to increase with higher degree of crosslinking.

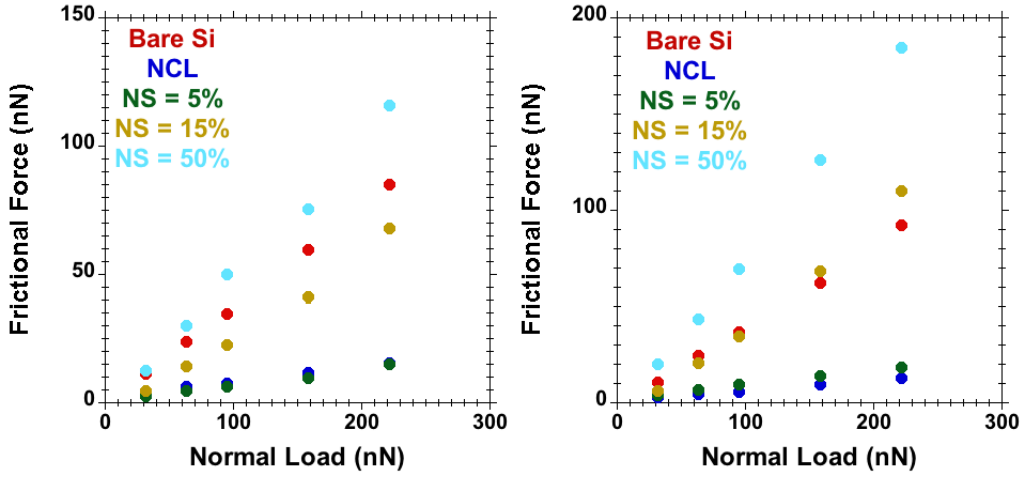

(a) (b)

Figure 3.3: Friction force against normal load for bare silicon surfaces and silicon surfaces bearing PGMA brushes and gels measured by colloidal-probe lateral force microscopy experiments with a tipless cantilever (0.976 N/m stiffness) and a silica colloid sphere of 14 µm diameter attached. PGMA gels have C_2 crosslinkers with degrees of crosslinking 5%, 15% and 50%. Experiments were performed at speeds of (a) 1 µm/sec and (b) 5 µm/sec.

Friction was found to increase with increase in speed at all crosslinking degrees. The measured friction for a 50% degree of crosslinking at 1 µm/sec, and for 15% and 50% at 5 µm/sec, was found to be larger than on bare silicon surface. The observed higher friction (in comparison to bare silicon surface) can be attributed to increase in contact area between the colloidal sphere and gels.

Figure 3.4 (a) and (b) present frictional force against normal load for PGMA brushes and gels (having C_6 chain long crosslinkers) and for bare silicon surface at speeds of 1 µm/sec and 5 µm/sec, respectively. As before, the experiments were performed in DMF with a tipless cantilever of stiffness 0.976 N/m with a silica colloidal sphere of diameter 14 µm attached to it.

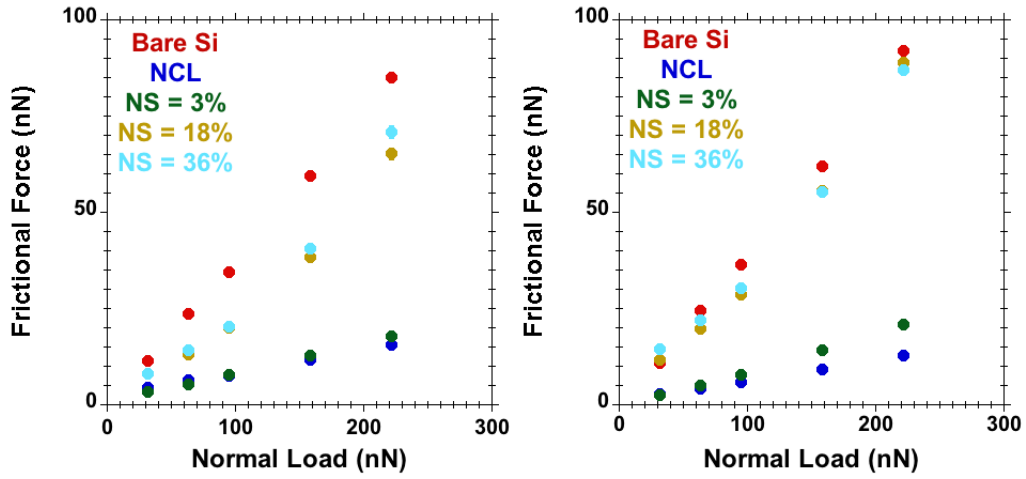

Figure 3.4: Friction force against normal load for bare silicon surfaces and silicon surfaces bearing PGMA brushes and gels measured by colloidal-probe lateral force microscopy experiments with tipless cantilever (0.976 N/m stiffness) with a silica colloid sphere of 14 µm diameter attached. PGMA gels have C_6 crosslinkers with a degree of crosslinking of 3%, 18% and 36%. Experiments were performed at constant speeds of (a) 1 µm/sec and (b) 5 µm/sec.

Friction is also found to increase with crosslinking degree. At 3% degree of crosslinking, the friction force is only slightly larger than that measured on (noncrosslinked) PGMA brushes. At 18% degree of crosslinking, friction is notably greater than that on (noncrosslinked) PGMA brushes and PGMA gels with 3% degree of crosslinking. With further increase in degree of crosslinking to 36%, no significant further increase in friction was observed compared to the results obtained with a degree of crosslinking of 18%. This is in contrast to the results for PGMA gels with shorter crosslinkers where we observed a significant increase in friction with increase in degree of crosslinking at all levels of degree of crosslinking.

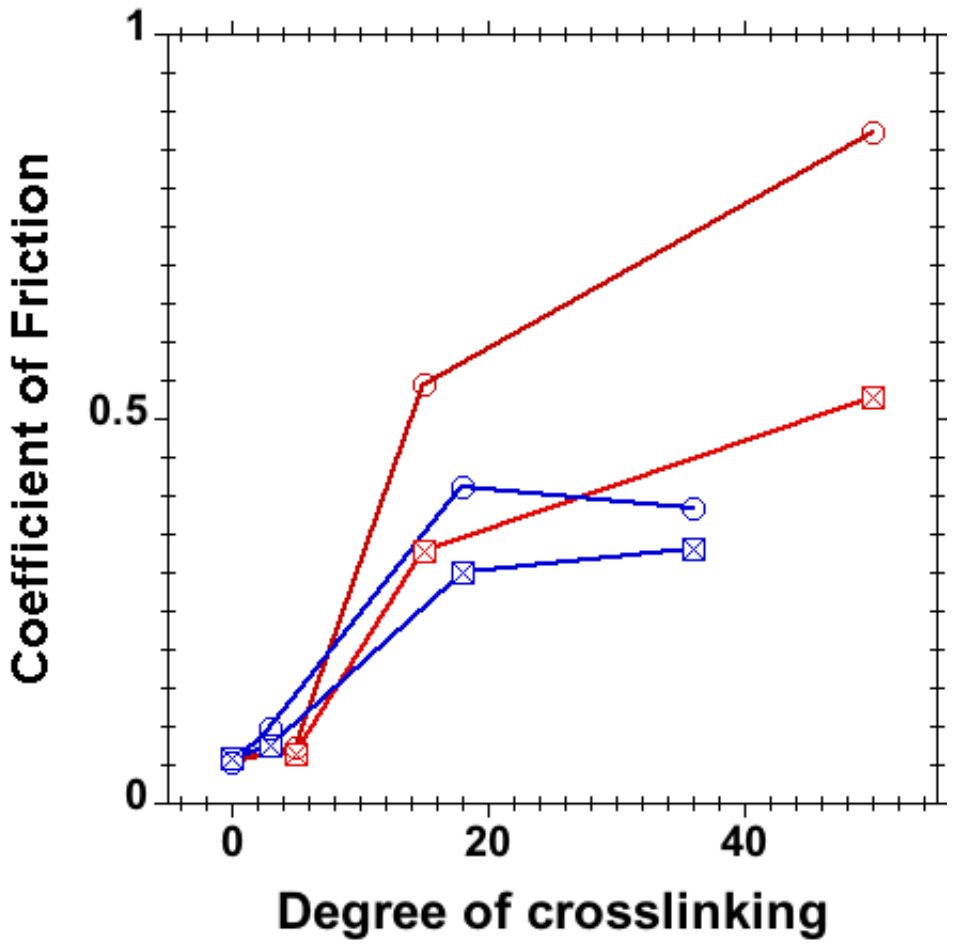

Figure 3.5: Coefficient of friction vs degree of crosslinking of PGMA gels grafted to silicon surfaces measured by colloidal-probe atomic force microscopy experiments with a 10 µm diameter silica colloid attached to a tipless cantilever (0.6 N/m stiffness) Red color for C_2 croslinkers and blue for C_6 crosslinkers. Open circles correspond to experiments carried out at 5 µm/sec and squares are experiments performed at 1 µm/sec.

Figure 3.5 shows the coefficient of friction as a function of the degree of crosslinking measured by lateral force microscopy at two different speeds for different lengths of crosslinkers. As mentioned before we see an increase in coefficient of friction with speed for both crosslinking lengths studied here. We also see an increase in coefficient of friction with increase in degree of crosslinking for both crosslinker lengths studied here, however the coefficient of friction value does not change significantly beyond a degree of crosslinking of 18% for C_6 crosslinkers. The coefficient of friction was found to be larger for the longer crosslinking length for lower degree of crosslinking but at higher degree of crosslinking (> 15%), friction was found to be smaller for the gel with longer crosslinkers.

3.2.2 Atomic-Force-Microscopy-Based Nanoindentation

AFM-based nanoindentation was employed to study the effect of crosslinking on the mechanical behavior of PGMA brushes and gels. The brushes and gels in DMF were indented with an AFM cantilever bearing silica colloidal sphere of 10-µm dia. The applied load against penetration depth is presented in Figure 3.6.

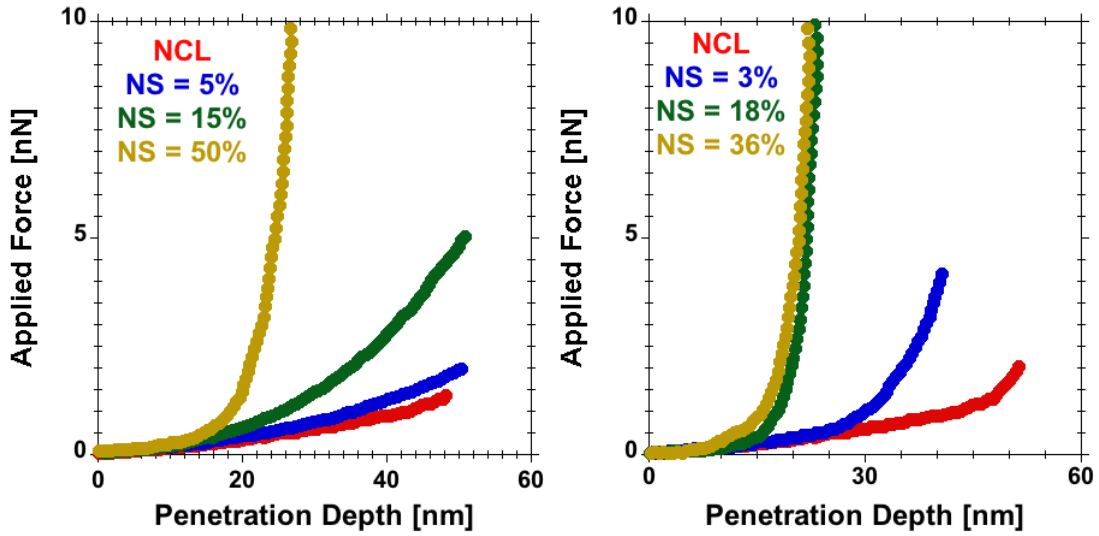

(a) (b)

Figure 3.6: Applied force against penetration depth measured by colloidal-probe atomic force miccroscopy with a 10 µm silica sphere glued to a tipless cantilever (0.6 N/m stiffness). For (a) PGMA gels with C_2 crosslinkers and (b) PGMA gels with C_6 crosslinkers. NCL stands for non-crosslinked and % values show the degree of crosslinking in each system.

Figure 3.6(a) and 3.6(b) show the applied load against indentation depth for different PGMA gels with different crosslinking degrees for C_2 and C_6 crosslinkers respectively. A change in the slope of the force-vs-depth curve occurs at the depth where the AFM cantilever begins to be noticeably influenced by the substrate; the steep part is just caused by substrate effect (substrate is close and the brush appears stiffer). Substrate influence begins to be felt at 10% indentation of the unperturbed brush height[10]. Hence, we can approximate the height of the PGMA brushes and gels by the penetration depth before this sudden change of the indentation force. With C_2 crosslinkers, as the degree of crosslinking increases from 5% to 50% the substrate effect is shown at a lesser depth, which indicates a decrease in the swelling ratio with

increase in degree of crosslinking. The indentation curve for PGMA gels with 5% crosslinking and brushes are similar; this coincides with the similar coefficient of friction measured by LFM (Fig3.5). The plausible decrease in swelling ratio with an increase in the degree of crosslinking could explain the increase in coefficient of friction: with the increase in degree of crosslinking, there are less brush-forming chains available at the outer film layer, which in fact facilitate the low friction behavior in polymer-brush based lubrication[5,11,12].

The indentation curves for PGMA gels with C_6 crosslinkers also reflect the tribological behavior of gels observed in LFM experiments. At a degree of crosslinking of 3%, the substrate effect is already significant at penetration depths above 30 nm (implying a decrease in swelling ratio compared to PGMA brushes), which correlates with the increase in coefficient of friction. As the degree of crosslinking is increased to 18%, there is a further decrease in swelling ratio and an increase in coefficient of friction was observed (Fig. 3.5). But with further increase in degree of crosslinking to 36% there is no significant change in the indentation behavior; similarly we did not see any significant change in the coefficient of friction.

3.3 Conclusions

AFM-based colloidal probe lateral force microscopy experiments were performed on PLMA brushes of different thicknesses in hexadecane and PGMA brushes and gels in DMF solvent. For the PLMA brushes two kind of tips were used: polyethylene (dia. 10μm) and silica (12 μm). The tribological experiments on PGMA brushes and gels were performed with a silica sphere of 14 μm dia. All the polymer brushes showed a remarkable decrease in friction forces when compared to bare silicon surfaces. We also observed a general increase in friction with crosslinking in PGMA brushes in DMF. An increase in coefficient of friction was observed with increase in degree of

crosslinking and decrease in coefficient of friction was observed with increase in length of crosslinkers above a certain degree of crosslinking. AFM-based indentation of PGMA brushes and gels in DMF solvent showed a decrease in swelling ratio with increase in degree of crosslinking and can very well explain the tribological response of gels at different degrees of crosslinking for different length of crosslinkers.

3.4 References

(1) Perry, S. S. Scanning Probe Microscopy Measurements of Friction. *MRS Bull.* **2011**, *29* (07), 478–483.

(2) Carpick, R. W.; Salmeron, M. Scratching the Surface: Fundamental Investigations of Tribology with Atomic Force Microscopy. *Chemical Reviews* **1997**, *97* (4), 1163–1194.

(3) Ramakrishna, S. N. *Adhesion and Tribology on Well-Defined, Nano-Scale Rough Surfaces: a Gradient Approach*; 2013.

(4) Nalam, P. C.; Ramakrishna, S. N.; Espinosa-Marzal, R. M.; Spencer, N. D. Exploring Lubrication Regimes at the Nanoscale: Nanotribological Characterization of Silica and Polymer Brushes in Viscous Solvents. *Langmuir* **2013**, *29* (32), 10149–10158.

(5) Li, A.; Benetti, E. M.; Tranchida, D.; Clasohm, J. N.; Schönherr, H.; Spencer, N. D. Surface-Grafted, Covalently Cross-Linked Hydrogel Brushes with Tunable Interfacial and Bulk Properties. *Macromolecules* **2011**, *44* (13), 5344–5351.

(6) Oliver, W. C.; Pharr, G. M. An Improved Technique for Determining Hardness and Elastic Modulus Using Load and Displacement Sensing Indentation Experiments. *Journal of Materials Research* **1992**, *7* (6), 1564–1583.

(7) Tranchida, D.; Kiflie, Z.; Acierno, S.; Piccarolo, S. Nanoscale Mechanical Characterization of Polymers by Atomic Force Microscopy (AFM) Nanoindentations:

Viscoelastic Characterization of a Model Material. *Measurement Science and Technology* **2009**, *20* (9), 095702.

(8) Klein, J.; Perahia, D.; Warburg, S. Forces Between Polymer-Bearing Surfaces Undergoing Shear. *Nature* **1991**.

(9) Bowden, F. P.; Tabor, D. The Area of Contact Between Stationary and Between Moving Surfaces. *Proceedings of the Royal Society of London Series a-Mathematical and Physical Sciences* **1939**, *169* (938), 391–413.

(10) Espinosa-Marzal, R. M.; Bielecki, R. M.; Spencer, N. D. Understanding the Role of Viscous Solvent Confinement in the Tribological Behavior of Polymer Brushes: a Bioinspired Approach. *Soft Matter* **2013**, *9* (44), 10572.

(11) Lee, S.; Spencer, N. D. Sweet, Hairy, Soft, and Slippery. *Science* **2008**, *319* (5863), 575–576.

(12) Chen, M.; Briscoe, W. H.; Armes, S. P.; Klein, J. Lubrication at Physiological Pressures by Polyzwitterionic Brushes. *Science* **2009**, *323* (5922), 1698–1701.

Chapter 4

Simulation Approach

Simulations were performed using a variant of a well-established, molecular coarse-grained brush model.[1-4] The advantage of using a coarse-grained description of polymers for the questions addressed in this work lies in the length and time scales that can be reached at moderate computational cost, compared with fully atomistic simulations. This approach allows the dynamical evolution of a brush system to be explored in the absence of the assumptions inherent in more macroscopic models, such as self-consistent, mean-field theories.[5-8] We have used the open-source code LAMMPS (Large-scale Atomic/Molecular Massively Parallel Simulator)[9] for our work. The calculated chain trajectories provide, together with the force field, complete information about chain alignment, density profiles, and the stress tensor. Quantities of interest to be extracted from the simulations are the density profiles, chain alignment, radius of gyration tensor, chain overlap, stress tensor, kinetic friction coefficient, as a function of relative shear velocity, load, grafting density, chain length, solvent quality, persistence length and cross-linking architecture. The corresponding results would allow us to shed light on brush systems including semi-flexible and cross-linked chains, which have so far not been investigated in detail.

4.1 Polymer-Brush Modelling

The polymer brushes were modeled using a set of semi-flexible, multi-bead-spring chains exhibiting excluded volume, where each chain is permanently fixed at one of its ends at a random position on planar surfaces. In this way we model chemisorbed polymer chains on substrates of infinite mass. Periodic boundary conditions were applied only along the axes parallel to the sliding surfaces. Interactions between

bonded beads were modeled using a finitely extendable, non-linear elastic (FENE) force law. The FENE potential U_{FENE} is given by

$$U_{\mathrm{FENE}}(r) = -0.5KR_0^2 \ln\left[1 - \left(\frac{r}{R_0}\right)^2\right] \qquad 4.1$$

The coefficient KR_0^2 sets the energy scale of interaction (we use the typical values K = 30, and R_0= 1.5), and R_0 is the maximum bond length, while r is the variable bond length. The FENE multibead-spring model is a coarse-grained approach that captures the basic physical behavior of polymeric systems successfully.[1,10] Excluded-volume interactions between all pairs of beads are modeled using classical Lennard-Jones (LJ) interactions, whose cutoff is chosen for bonded pairs to ensure a purely repulsive interaction (WCA potential). Due to the FENE + LJ interactions the polymer is not completely flexible but exhibits a persistence length of the order of 1.32 times bond length.[28] To ensure that beads do not cross the grafting surface, an additional 9/3 repulsive wall potential U_{wall} is added

$$U_{\mathrm{wall}}(z) = \epsilon\left[\frac{2}{15}\left(\frac{\sigma}{z}\right)^9 - \left(\frac{\sigma}{z}\right)^3\right], \qquad z < z_c \qquad 4.2$$

where z is the distance of the polymer bead to the nearest grafting surface, and z_c denotes the cut-off distance of the wall potential.

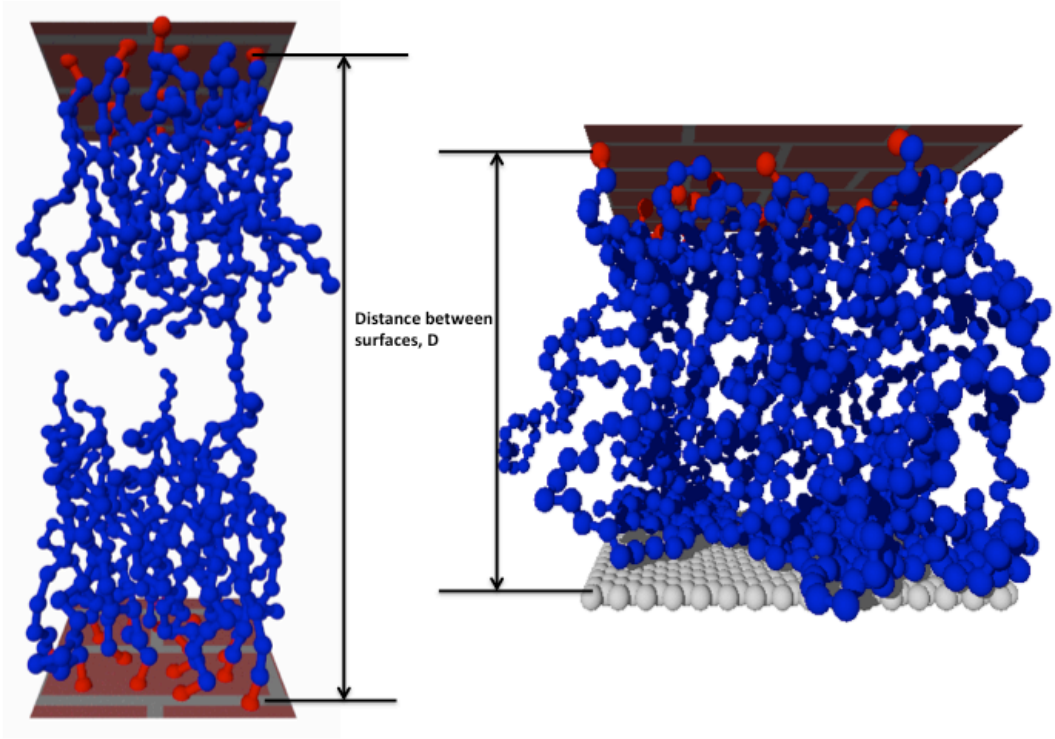

Figure 4.1: Snapshots of polymer-brush systems with M=20 chains tethered on each grafting surface (a) Symmetric brush-brush configuration and (b) asymmetric brush-against-wall configuration. Red beads are tethered, blue beads are non-tethered, grey beads are explicit wall beads and flat walls are flat (indicated as "brick walls").

We have performed simulations with randomly grafted polymer chains on a flat surface. To study brushes at rest and under shear we will follow standard recipes for the implementation. The simulations have been carried out for two kinds of systems. The MD simulations have been performed for a brush-brush system (Fig: 4.1a). Two types of polymer beads—non-tethered and tethered—are used. The second system is a brush-wall setup (Fig: 4.1b) studied. Here, three types of particles are used: non-tethered and tethered polymer beads as well as explicit wall particles.

4.2 Explicit-Wall Modelling

```
i=0;
for ix=1:nx
    for iy=1:ny
        for i3=1:2
            i=i+1;
            xw(i) = xw(i3) + a*(ix-1);
            yw(i) = yw(i3) + a*(iy-1);
            zw(i) = 0.5;
            %rn = randi([-1 1]);
            %zw(i) = 0.5*rn;
        end
    end
end
```

```
i=0;
for ix=1:nx
    for iy=1:ny
        for i3=1:2
            i=i+1;
            xw(i) = xw(i3) + a*(ix-1);
            yw(i) = yw(i3) + a*(iy-1);
            rn = randi([-1 1]);
            zw(i) = 0.5*rn;
        end
    end
end
```

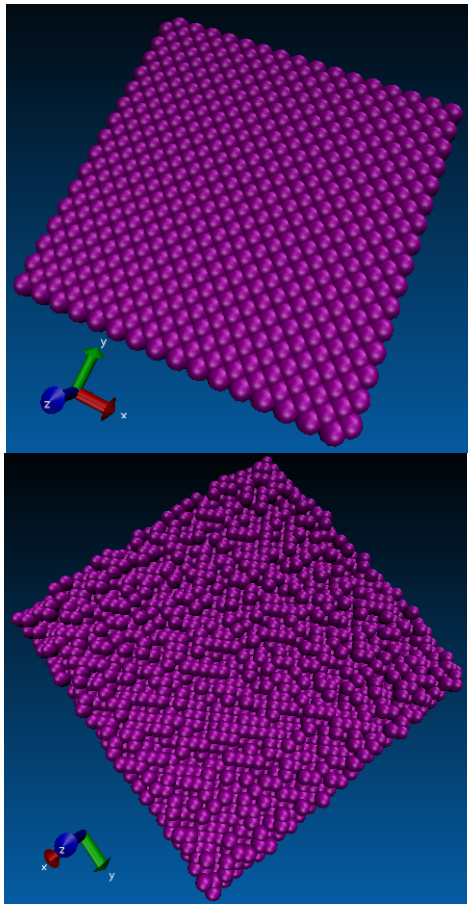

Figure 4.2: Planar smooth explicit-wall (top) and Rough explicit wall (bottom) and corresponding changes made in codes.

4.2.1 Planar Smooth Wall

The explicit-wall beads are fixed at regular 2-D lattice positions (lattice constant ~ 1) and interact with polymer beads via the LJ potential (4.3) with cut-off R_{cw}. Here (Fig:1.2 (top)) the counter wall is modeled as rigid and basically flat with a corrugation at the sub-nanometer scale.

4.2.2 Rough Wall

Here the spherical beads are placed in similar way as for planar wall in the xy-plane, but along the z-axis direction it has been randomly placed at (D – 1) or (D -1) ±0.5 to give the roughness effect to the rigid wall as shown in Fig 1.2 (bottom). The number

of beads in each of the walls is the same and the interaction of the wall with the polymer and solvent beads are the same in both the cases.

4.3 Solvent-Quality Modeling

The solvent quality can be modeled (i) implicitly by incorporating an attractive component to the Lennard-Jones interaction (Fig. 4.3) between non-bonded pairs. (ii) Alternatively, explicit solvent molecules can be incorporated in the simulation system as done by Galuschko et al. by using Lenard-Jones monomers or dimers.[2]

4.3.1 Implicit-Solvent Modelling

Good solvent quality has been modeled implicitly by incorporating only the repulsive part of the LJ interaction between non-bonded pairs,

$$U_{\mathrm{LJ}}(r) = 4\epsilon \left[\left(\frac{\sigma}{r}\right)^{12} - \left(\frac{\sigma}{r}\right)^{6} \right], \qquad r \leq R_c \tag{4.3}$$

and nothing else, where R_c is the cut-off distance for non-bonded interactions; σ and ϵ set the length and energy units, respectively. The value of Rc = $2^{1/6}$ = 1.12246 is taken to ensure good solvent conditions (WCA potential).

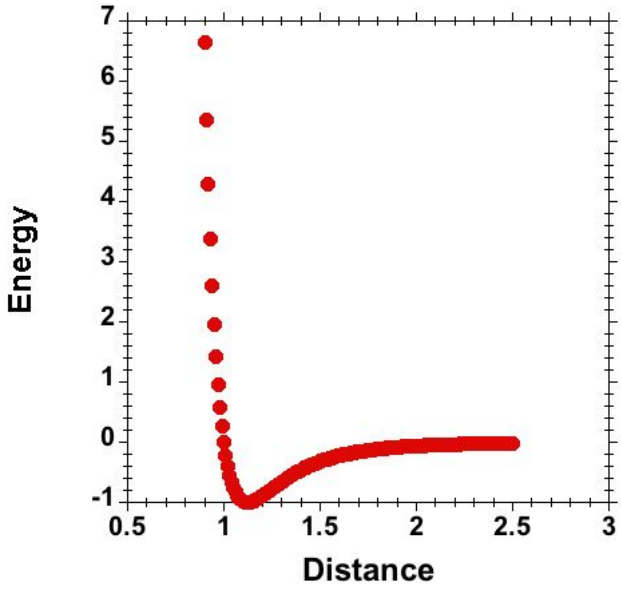

Figure 4.3: Potential against distance for Lennard-Jones 12/6 potential. For our implicit-solvent-based simulations we have kept the cut-off as 1.12246 to ensure good solvent conditions.

The dynamics of such a molecular model at constant temperature were explored by solving modified (thermostatted) Newton's equations with an implicit solvent (Langevin equations).

4.3.2 Explicit Solvent Modelling

As mentioned earlier we have also used explicit solvent beads for the simulation studies presented in this thesis. We have used an explicit solvent model as used by Binder et. al[11] in their previous work. They have followed Soddemann[12] to truncate the Lennard-Jones (LJ/12-6) potential at its minimum point and shift it to some desired depth (ϵ_{pp} , ϵ_{ps}), continuing from its minimum to zero with a potential having a cosine form and thus providing a potential that is both continuous and has a continuous derivative too. Thus our potential is

$$U_{LJ\,cos}\,(r) \;= 4\epsilon_{LJ}\left[\left(\frac{\sigma_{\alpha\beta}}{r}\right)^{12} - \left(\frac{\sigma_{\alpha\beta}}{r}\right)^{6} + \frac{1}{4}\right] - \epsilon_{\alpha\beta}\,,\; r \leq \sigma_{\alpha\beta}2^{\frac{1}{6}} \qquad 4.4$$

where (αβ) stands for the different types of pairs: polymer-polymer (*pp)*, polymer-solvent (*ps)*, and solvent-solvent (*ss)*, respectively, and we choose the range parameters identical, $\sigma_{pp} = \sigma_{ps} = \sigma_{ss}$. Scales for length and energy (and temperature) are chosen such that both $\sigma_{pp} = 1$ and $\epsilon_{\mathrm{LJ}} = 1$ (Boltzmann's constant $k_B = 1$). For $r \geq \sigma_{\alpha\beta}2^{1/6}$ we choose the cosine potential[11,12] as follows (Fig. 4.4)

$$U_{LJ\,cos}\,(r) = \begin{cases} \frac{1}{2}\epsilon_{\alpha\beta}\left\{cos\left[a\left(\frac{r}{\sigma_{\alpha\beta}}\right)^{2} + b\right] - 1\right\}, & 2^{\frac{1}{6}} \leq {}^{r}/_{\sigma_{\alpha\beta}} \leq 1.5 \\ 0, & r \geq 1.5\sigma_{\alpha\beta} \end{cases} \qquad 4.5$$

As explained in detail in the paper[11] we have used value of a = 3.1730728678 and b = -0.85622864544 to ensure that the potential ($U_{\mathrm{LJcos(r)}}$) and its derivative is continuous at potential minimum point ($r_{c,in} = \sigma_{\alpha\beta}2^{1/6}$) and at the potential cut-off point $r_{c,out} = 1.5\sigma_{\alpha\beta}$.

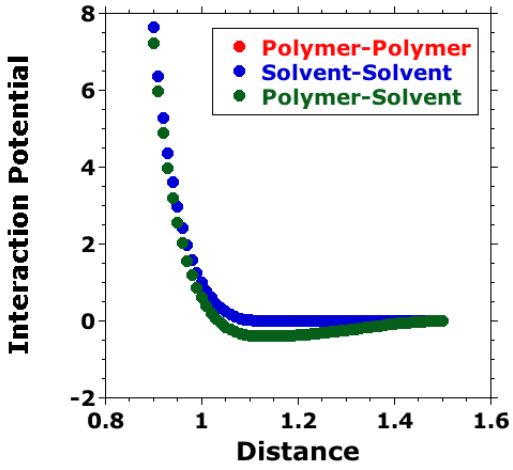

Figure 4.4: Energy-vs-distance plot for modified Lennard-Jones 12/6 potential with $\epsilon_{pp} = \epsilon_{ss} = 0$ and $\epsilon_{ps} = 0.4$. The polymer-polymer curve is identical with the solvent-solvent curve and therefore invisible.

The temperature was maintained constant by resetting the temperature of a group (all the beads except tethered beads) of atoms by explicitly rescaling their velocities. Any bias velocity (due to shear speed applied during shearing) is removed before thermostatting. When a temperature is computed, the center-of-mass velocity for the set of beads that is under thermostatting is calculated. This bias velocity is then subtracted from the velocities of individual beads to yield a thermal velocity for each bead. The thermal velocity is rescaled to the desired value and subsequently the bias speed is added. The velocity profile was determined by calculating the mean velocity in different layers.

4.4 Chain-Stiffness Modelling

For chain-stiffness modeling we have used the following potential:

$$U_s = K_s[1 + \cos(\theta)] \qquad 4.6$$

for all sets of 3 consecutive beads in each polymer chain. Here K_S (energy) is the bending rigidity and θ is the angle between consecutive segment vectors. It is one of the simplest models to implement chain stiffness and only the K_S value needs to be declared. The higher the value of K_S, the stiffer the chain is (Fig. 4.5).

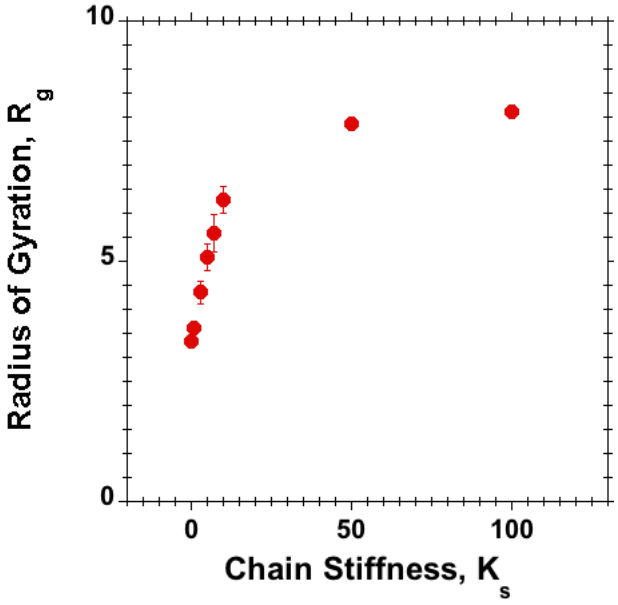

Figure 4.5: Radius of gyration against chain stiffness parameter, K_s for a single chain with N = 50 beads under good solvent conditions (WCA interactions between non-bonded beads).

4.5 Crosslinking Modelling

Crosslinking between chains in polymer-brush systems can be generated using various approaches: (i) In-situ method where polymer chains are crosslinked while growing from tethered beads if the terminal beads of any of two polymer chains at any stage are within pre-defined length of crosslinkers, (ii) Addition of explicit crosslinkers to an existing polymer brush. Within this method crosslinkers are allowed to equilibrate and to get bonded with different chains via their terminal ends. In this way crosslinking can be achieved between different chains in the system, (iii) After generating a polymer brush system we can choose randomly from those pairs of beads that are not yet crosslinked and separated by a distance (nearly) identical with the length of a crosslinker chain and then insert the crosslinker chain if it does not overlap with existing beads until all crosslinker chains have been inserted.

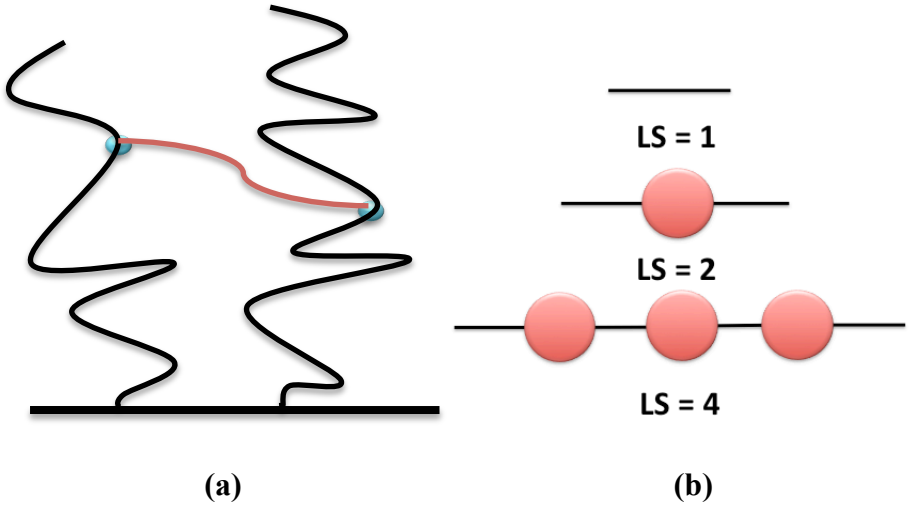

Figure 4.6: Schematic showing a crosslinker chain between two crosslinked chains (b) Explicit crosslinkers of different lengths

We have employed the third approach for our study of a crosslinked polymer brush system. The crosslinked polymer brush system was generated for different numbers of crosslinkers/spacers (NS) for a fixed length of crosslinker/spacer (LS) and vice-versa. Figure 4.6 shows a typical crosslinked chains in the system of crosslinked polymer brushes. Figure 4.6 (b) shows the explicit crosslinkers, where LS = 1 means that there is no explicit bead in a crosslinker but that it is represented by a single bond between crosslinked beads, LS = 2 means that the explicit crosslinker chain has a single explicit bead which is bonded to a bead in the respective chains to be crosslinked and similarly a LS = 4 explicit crosslinker has 3 explicit beads which are bonded to form a linear chain and each end is bonded to a bead in the crosslinked chains (Fig. 4.6).

For bonding within crosslinkers/spacers and bonding between crosslinkers/spacers and chains in the polymer brush system we have used a harmonic bond potential:

$$E_H = K_H(r - r_0)^2 \qquad 4.7$$

where K_H is the bond strength factor, r_0 is the equilibrium bond length and r is the distance between bonded atoms at any given time. We use typical values $K_H = 100$ and $r_0 = 1$.

4.6 Shear modeling

In a next step the equilibrated systems are subjected to shear. The calculated chain trajectories provide, together with the force field, the complete information about chain alignment, density profiles, and the stress tensor, in particular. The coefficient of friction (CoF) is extracted from the ratio between shearing and normal forces exerted onto the surfaces to maintain a constant shear speed and gap size, or alternatively, by the ratio between two components of the measured stress tensor $\boldsymbol{\tau}$, using the Irving-Kirkwood expression.[13,14] The load is measured at fixed gap size and the relative shear velocity is held fixed during individual simulation runs.

Coefficient of Friction = Shear Stress/Normal Stress

$$= \langle\tau_{xz}\rangle/\langle\tau_{zz}\rangle \qquad 4.8$$

4.7 References

(1) Grest, G. Interfacial Sliding of Polymer Brushes: a Molecular Dynamics Simulation. *Phys. Rev. Lett.* **1996**, *76* (26), 4979–4982.

(2) Galuschko, A.; Spirin, L.; Kreer, T.; Johner, A.; Pastorino, C.; Wittmer, J.; Baschnagel, J. Frictional Forces Between Strongly Compressed, Nonentangled Polymer Brushes: Molecular Dynamics Simulations and Scaling Theory. *Langmuir* **2010**, *26* (9), 6418–6429.

(3) Grest, G. S. Normal and Shear Forces Between Polymer Brushes. *Adv. Polym. Sci.* **1999**, *138*, 149–183.

(4) Kremer, K.; Grest, G. S. Dynamics of Entangled Linear Polymer Melts: a Molecular-Dynamics Simulation. *J. Chem. Phys.* **1990**, *92* (8), 5057–5086.

(5) Halperin, A.; Zhulina, E. B. Atomic Force Microscopy of Polymer Brushes: Colloidal Versus Sharp Tips. *Langmuir* **2010**, *26* (11), 8933–8940.

(6) Zhulina, E. B.; Borisov, O. V.; Priamitsyn, V. A. Theory of Steric Stabilization of Colloid Dispersions by Grafted Polymers. *J. Colloid Interf. Sci.* **1990**, *137* (2), 495–511.

(7) Halperin, A.; Kröger, M.; Zhulina, E. B. Colloid-Brush Interactions: the Effect of Solvent Quality. *Macromolecules* **2011**, *44* (9), 3622–3638.

(8) Wijmans, C. M.; Scheutjens, J. M. H. M.; Zhulina, E. B. Self-Consistent Field Theories for Polymer Brushes: Lattice Calculations and an Asymptotic Analytical Description. *Macromolecules* **1992**, *25*, 2657–2665.

(9) Plimpton, S. Fast Parallel Algorithms for Short-Range Molecular Dynamics. *J. Comput. Phys.* **1995**, *117* (1), 1–19.

(10) Kröger, M. Simple Models for Complex Nonequilibrium Fluids. *Phys. Rep.* **2004**, *390* (6), 453–551.

(11) Dimitrov, D. I.; Milchev, A.; Binder, K. Polymer Brushes in Solvents of Variable Quality: Molecular Dynamics Simulations Using Explicit Solvent. *J. Chem. Phys.* **2007**, *127* (8), 084905.

(12) Soddemann, T. Non–Equilibrium Molecular Dynamics Study of an Amphiphilic Model System. **2001**.

(13) Hess, S.; Kröger, M. Elastic and Plastic Behavior of Model Solids. *Technische Mechanik* **2002**.

(14) Kröger, M. *Models for Polymeric and Anisotropic Liquids*; Berlin Heidelberg, 2005; Vol. 675.

Chapter 5

MD Simulation of Polymer Brushes under Shear Compared with Experimental Results[1]

5.1 Simulation Details

The goal of the current study was to model the dextran polymer-brush system in aqueous buffer, and to interpret the behavior observed experimentally.[1,2] In particular, the objective of the molecular dynamics (MD) simulations was to investigate the relevant mechanisms underlying the frictional response of polymer brushes at the molecular scale from a coarse-grained model. Our model aims not only at a qualitative but also at a quantitative description of the behavior of a particular brush under a given solvent. We simulated a polymer brush system using a coarse-grained, multibead spring model. In a first step, simulation parameters, such as bead size (σ) and number of beads (N) per chain were obtained from comparison between simulated and experimentally determined gyration radii.

Using the calculated parameters, we then carried out an equilibrium molecular dynamics simulation, in which we slowly compress opposite surfaces carrying polymer chains against each other. The concentration profiles under various conditions, including non-compressed brushes, marginally compressed brushes, and highly compressed brushes, were compared with results from self-consistent field (SCF) theory, because corresponding experimental results were not available. Simulated force-distance isotherms were compared with existing experimental results

[1] Most part of this chapter is taken from my already published work: "Polymer Brushes under Shear*: Molecular Dynamics Simulation Compared to Experiments" Langmuir 2015, (31) 4798-4805.* I carried all the simulation work and writing and co-authors participated in discussions and interpretation of data and editing of the paper.

for dextran polymer brushes obtained with an extended surface forces apparatus (eSFA)[1].

Next, by employing non-equilibrium molecular dynamics simulations, the equilibrated polymer-brush system was sheared. Such simulations were carried out for a polymer brush sliding against a bare surface. Shear (friction) stresses at different speeds were calculated and compared with the corresponding experimental results for dextran brushes[2] that were obtained from colloidal-probe lateral force microscopy (LFM) experiments. We find that the experimentally observed leveling-off in the coefficient of friction in the so-called "boundary-like" regime at low speeds [2-4] can be interpreted by an effective attractive force between brush and opposing wall.

We have carried out the simulations for two kinds of systems. The equilibrium MD simulations have been performed for a brush-brush system (Fig. 4.1(a)). Two types of beads—non-tethered and tethered—are used. The second system is a brush-wall setup (Fig. 4.1(b)) studied via non-equilibrium MD simulations. Here, three types of particles are used: non-tethered and tethered beads as well as explicit wall particles. The latter are fixed at regular lattice positions and interact with polymer beads via the LJ potential (Eq. 4.3) with cut-off R_{cw}. We therefore model the counter wall as rigid and basically flat with a corrugation at the subnanometer scale. We have performed simulations with randomly grafted polymer chains on a flat surface. The system consists of $M = 20$ chains on each side, with every chain having $N = 50$ beads and grafting density, $\rho = 0.075$ (LJ units, the corresponding dimensional value is $\rho = 0.075/\sigma^2 \approx 0.3$ nm^{-2}). Similar results were obtained with $M = 50$, $N = 50$ and $\rho = 0.075$, which indicates that system size has no bearing on the outcome. The cut-off distance, $R_c = 2^{1/6} \approx 1.122$ (0.561 nm) was kept for interactions between non-bonded beads for all simulations unless otherwise stated. The cut off, $z_c = 0.5$ was used for

wall potential (Eq. 4.2). The Langevin thermostat parameters used were T = 1.2 and damping coefficient ξ = 0.1.

5.2 Experiments

The polyelectrolyte copolymers PLL(20 kDa)-*g*[3.5]-dextran(5 kDa) (PLL-g-dextran), purchased from SuSoS AG (Dübendorf, Switzerland) were characterized in HEPES (aqueous buffer, pH = 7.4, 10 mM of 4-(2-hydroxyethyl)-1-piperazine-1-ethanesulfonic acid, St. Louis MO, USA). The radius of gyration, R_g of a 5 kDa dextran chain is 2.35 nm[5] and degree of polymerization of the dextran ≈ 33. PLL-g-dextran adsorbs onto negatively charged substrates (in aqueous buffer) via the positively charged poly(L-lysine) backbone, forming brush-like structures. From adsorption measurements, which showed a dry thickness of 2.06 nm, the grafting density of the dextran brush was determined to be ≈ 0.31 ± 0.02 chains per nm^2, which corresponds to a grafting distance between the dextran chains d_0 of 1.9 ± 0.10 nm, assuming hexagonal packing.

Espinosa-Marzal *et. al.*[1] used extended surface forces apparatus (eSFA) measurements to determine forces between dextran-brush-bearing surfaces as a function of the surface separation (D), as measured by multiple-beam interferometry. The forces were measured during the approach of surfaces at a constant speed of 3 Å s^{-1}. The slow surface approach ensured the exclusion of any hydrodynamic effects.

Friction measurements were reported by Nalam *et al.*[2] using an atomic force microscope (MFP-3D, Asylum Research, Santa Barbara, CA). Lateral force measurements were performed with a bare silica colloid probe against a dextran-brush-bearing silicon surface in HEPES solvent. Tipless, gold-coated cantilevers (CSC12, MikroMasch, Estonia) with a normal stiffness of 0.5−0.7 N/m were used to measure lateral forces. Silica microspheres (EKA Chemicals AM, Kormasil), with

diameters ranging from 15 to 20 μm, were attached to the tip-less cantilever using UV-glue (NOA 63, Norland Optical Adhesive, Cranbury, NJ). The friction-force measurements were carried out at a constant load of 100 nN over a range of speeds between 0.1 – 500 μm s^{-1}. According to previous studies[6,7] the effect of residual silica surface charges not counterbalanced by lysine is screened at high ionic strength (10 mM). While dextran is a neutral polymer, which had been studied as such in previous simulation works,[8] the influence of residual silica surface charge on the electrostatic contribution to net force had been found to be negligible.[6,7]

5.3 Calculating simulation parameters

The number of beads in each chain, *N,* and bead size, σ, were calculated by comparing the experimentally available radius of gyration, R_g, and the length of a fully extended polymer chain, R_{max}, with corresponding results from our simulations of a single linear chain. Small side-chains that may be present to a small (< 5%) amount in dextran are part of the assumed spherical "bead". Larger amounts of sidechains could be modeled by considering either nonspherical beads or a a more detailed model. In Fig. 5.1, the radius of gyration, R_g is plotted as a function of *N*. Our simulation results are well captured by

$$R_{\max} = N\sigma \tag{5.1}$$

$$R_g = 0.49 \times N^{0.59}\sigma \tag{5.2}$$

where the exponent agrees with that for a self-avoiding walk. Inserting the experimental values[1] R_g = 2.35 nm and R_{max} = 23.43 nm for the reference system into Eqs. (5.1) and (5.2) we obtain $N \approx 50$ and $\sigma \approx 0.5$ nm for the corresponding model system. Notice that three beads are thus required to represent approximately two dextran monomers. In the oligosaccharide range (molecular weight M_w < 2 kDa) a dextran polymer chain is known to assume a rather stiff, rodlike conformation. This

range is followed by a transition from rod-like to coil-like conformations at M_w > 2 kDa, where the dextran polymer chains become very flexible[9]. Due to excluded volume incorporated in the multibead-spring model and the accompanying finite persistence length, more than a single bead is required to model a monomer of a 5 kDa dextran chain. There are previous MD-simulation studies that eventually used three beads of size 0.3 nm to represent a single dextran monomer.[8]

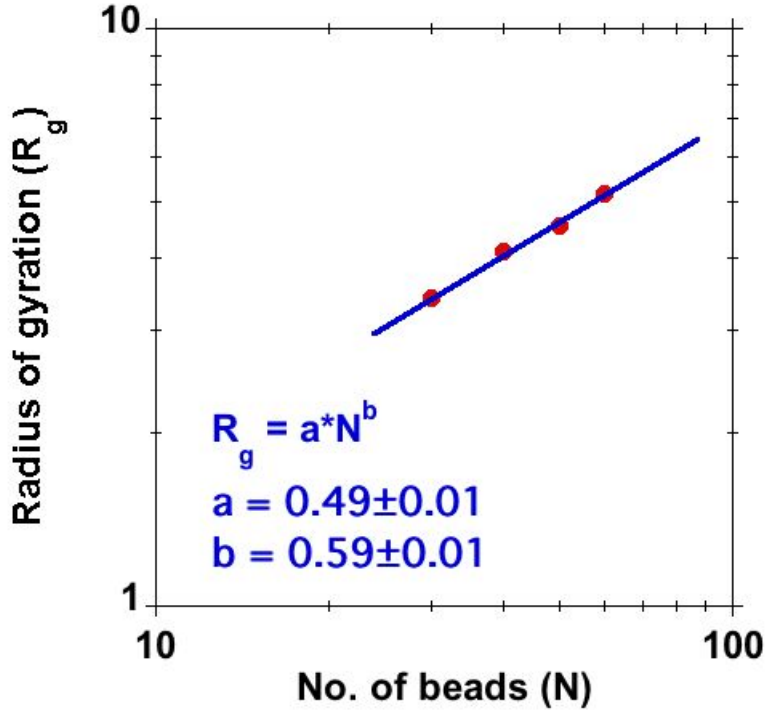

Figure 5.1. R_g versus N from MD simulation (red circles) and curve-fitting using least square method (blue line).

An energy scale ϵ of the potential is needed to calculate the dimensional load at different surface separations. It can be estimated using two different approaches: (i) Using $\epsilon = k_B T$ where k_B denotes Boltzmann's constant yields $\epsilon = 4.14 \times 10^{-21}$ J at room temperature, T = 300 K. (ii) Matching our simulation results for loads with the corresponding experimental results[1] we obtain $\epsilon = 4.8 \times 10^{-21}$ J in agreement with the value reported by de Beer[10]. Both values are comparable in magnitude; we are going to apply the latter value to calculate dimensional quantities in this chapter.

5.4 Density Profile

In the equilibrium MD simulation**,** polymer brushes attached to opposite planar surfaces were compressed quasi-statically as follows: (i) One surface was kept fixed and the other was moved a distance σ towards the fixed surface at constant velocity 0.01, using an integration time step of $\Delta t = 0.001$. (ii) The distance was kept fixed and data collected for the following 3×10^6 time steps using $\Delta t = 0.0025$. This procedure was repeated, starting with (i).

In Fig. 5.2, simulation results for the concentration profile (expressed as volume fraction vs. distance) for uncompressed (3a), marginally compressed (3b) and highly compressed (3c) brushes are plotted and compared with results calculated according to the SCF theory.[11]

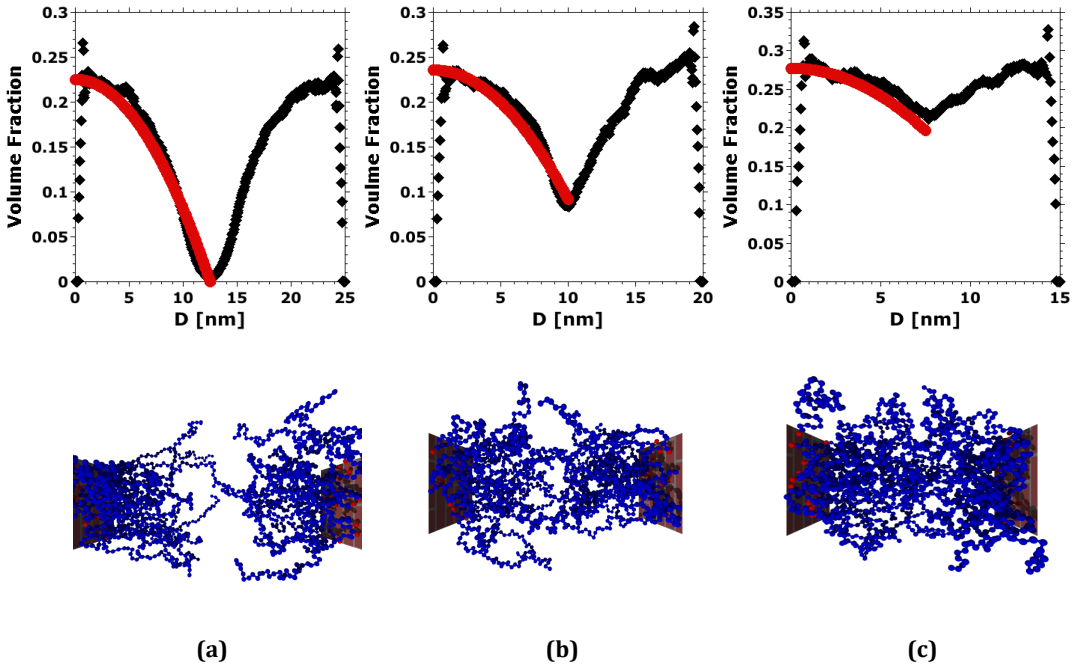

Figure 5.2. Comparison of MD simulation results (black symbols) and SCF theory results (red lines) for a brush-brush system. Concentration profile and images obtained (Pro-v software) for an (a) uncompressed brush (*D*=25 nm), (b) marginally compressed brush (*D*=20 nm) and (c) highly compressed brush (*D*=15 nm).

The simulation results were found to be in good agreement with the SCF theory results, while the deviations close to the tethering surface are due to the mesoscopic features of the model used.

5.5 Compression Curve

The compression curve (force against distance) obtained from MD simulations was compared with experimental eSFA[1] results for a brush-brush system (Fig. 4.1a). Within the MD simulation, the brushes were quasi-statically compressed, and the normal stress at each distance obtained from the expression for the stress tensor[12], where the dimensional stress is obtained from the dimensionless value by multiplying with $\epsilon/\sigma^3 \approx 40$ MPa. The normal stresses were integrated with respect to distance between the walls to obtain the experimental F/R against D (separation between brushes) curve, as explained below.

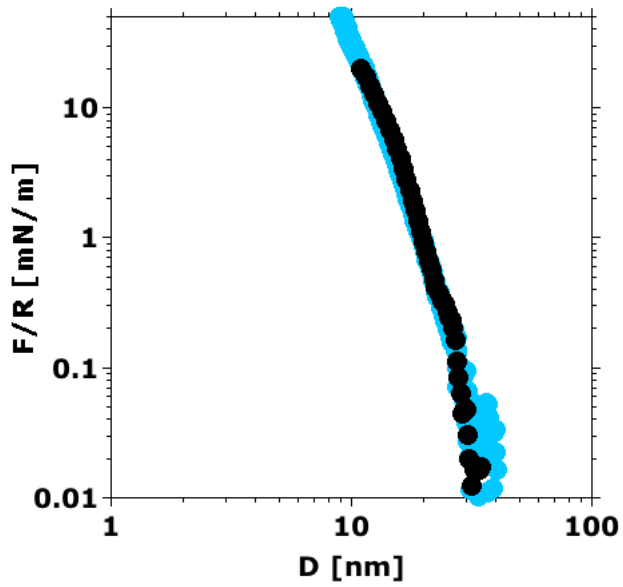

Figure 5.3. Comparison between MD (black circles) and experimental (cyan circles) results for a brush-brush system. Normal forces versus the surface separation (D) for 20 chains with N = 50 beads on each grafting side at a grafting density ρ = 0.075 (0.3 nm^{-2}). Experimental results of Espinosa-Marzal *et al.*[1] for the normal forces of mica surfaces bearing dextran brushes in HEPES during approach at a constant speed of 3 Å s^{-1}. The experimental force is normalized by the radius of curvature $R \approx 20$ mm of the crossed cylindrical surfaces. A similar plot comparing the results with SCF theory prediction is shown in the Appendix I.

Figure 5.3 shows that our simulation results are in good agreement with available experimental results.[1] The agreement is worst at the onset of repulsion, i.e. as the opposite polymer chains just start to interact with each other. The deviations in the result at a lower force regime could be due to the different geometry used.[13,14] The experiments were carried out with polymer chains attached on opposed, crossed cylinders, whereas the simulations were performed with polymer chains attached to flat surfaces. Using the Derjaguin approximation, when the radii of curved surfaces (R) are much larger than the separation (D) between the surfaces, the following relation is fulfilled

$$F(D) = 2\pi R E(D) \qquad \text{for} \qquad R \gg D \tag{5.3}$$

The measured force F between the two curved surfaces is related to the surface energy E of two flat surfaces at a separation D. Accordingly, the interaction energy E calculated from simulations is related to the measured force between the curved surfaces by a factor equal to $2\pi R$ [13].

Polydispersity of chain lengths (in the experiment) can also affect the results in the lower force regime[15,16]. Thus, the polymer chains start interacting with the opposite chains at different separations in the experiment, whereas in the simulations of monodisperse chains, all the chains start interacting at a comparable separation. When the polymer brushes are compressed further, experiment and simulation results coincide, since all the polymer chains are compressed, both in experiment and in simulation.

5.6 Shear and Friction

Equilibrated asymmetric brushes were subjected to shear against a counter-wall surface (Fig. 4.1(b)). Simulations were carried out at fixed separation, *D=7 (3.5* nm) while applying shear speeds in the range of v = 0.0003 to 0.1 (LJ units) on the wall

carrying the permanently tethered beads. The surface separation (D) was held constant to calculate normal and shear stress as a function of the different speeds. For every chosen speed, the normal and shear stresses were sampled at each time step (Δt = 0.0025) over an interval of at least 3×10^6 steps (for the highest speeds, more steps at lower speeds). The first 5×10^5 time steps belonging to the startup phase preceding the sampling period, each of duration Δt = 0.001, were ignored for the analysis of stationary quantities.

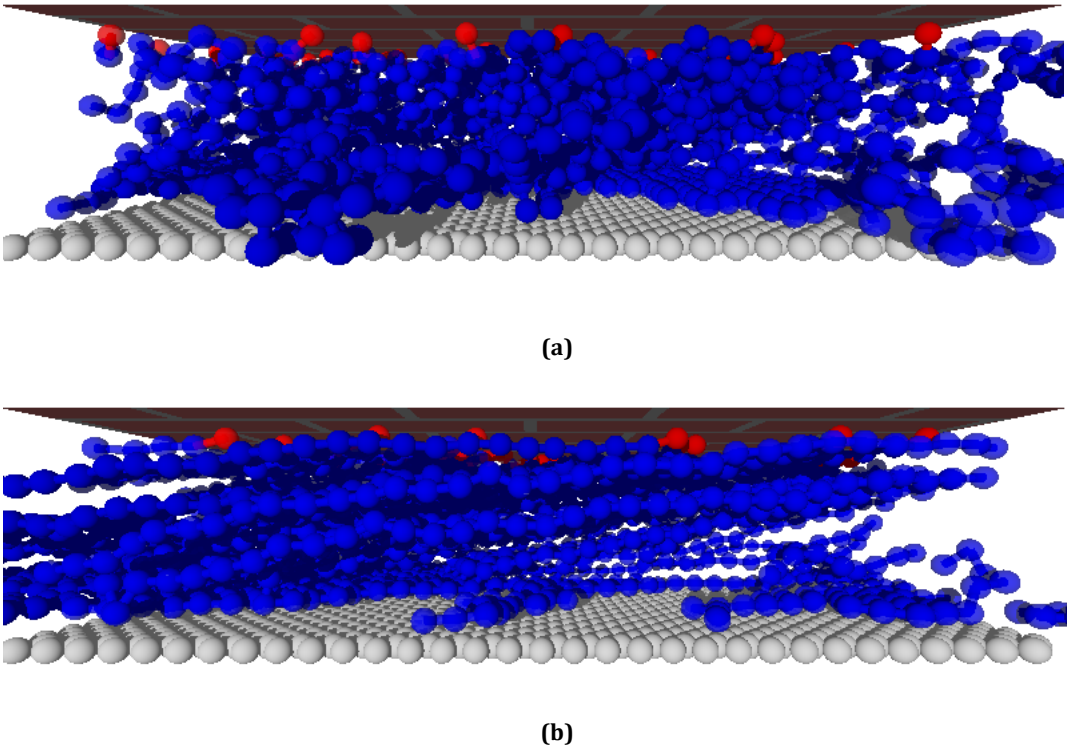

(a)

(b)

Figure 5.4. Visualization of sheared brush at relative wall speed (a) v = 0.0003 and (b) v = 0.01. The brush consists of M = 20 chains with N = 50, the separation is D = 8 (4 nm).

The MD-simulation results were compared with the experimental results in Fig. 5.4(a). It is worth mentioning that contrary to the constant-separation conditions we chose for the MD simulations, in the LFM experiments[2] a constant normal load was applied and shear (friction) forces were measured at different speeds; the film thickness or surface separation (D) might have changed with speed during the experiment, but it was not measured. Within a stationary situation, the normal stress

that we measure for a given D can also be interpreted as the applied normal stress resulting in the surface separation D. If we compare such an experimental curve with a simulated one for a single separation, both recorded versus shear speed, a direct comparison is only possible over the range of speeds for which the simulated normal stress remains constant.

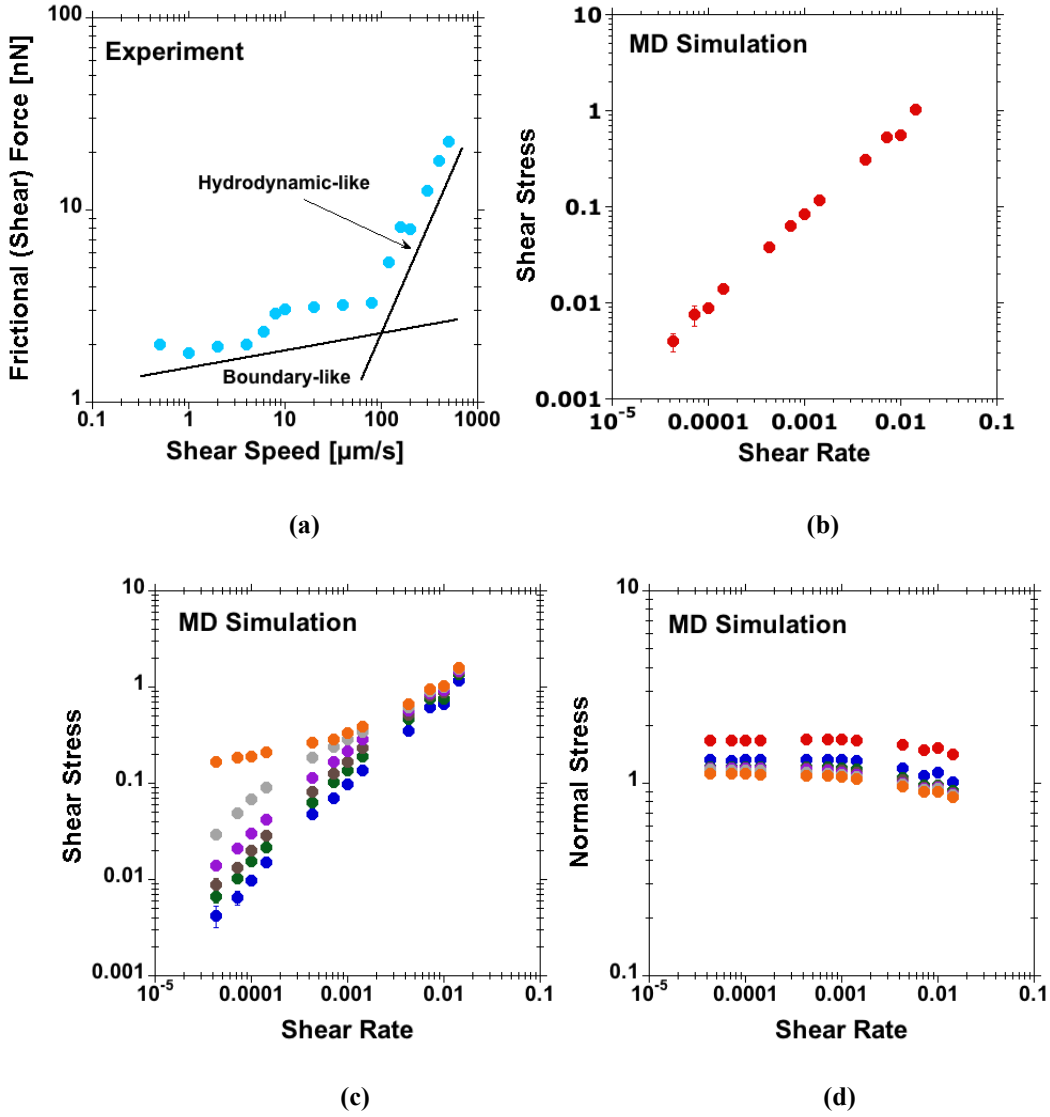

Figure 5.5. Forces and stresses against shear speed in (a) and shear speed divided by gap distance, ie. shear rate in (b-d), for brush-against-wall systems. (a) LFM experiment results[2] for dextran polymer brushes in HEPES, (b) MD simulation results for purely repulsive (LJ/12-6 cut-off, $R_{cw} = 2^{1/6}$ and depths of the potential well parameter, $\epsilon = 1$) brush-wall interaction. (c) MD simulation results for modified brush-wall interaction, $R_{cw} = 2.5$ and $\epsilon = 1$ (blue), $\epsilon = 2$ (green), $\epsilon = 2.25$ (brown), $\epsilon = 2.5$ (pink), $\epsilon = 2.75$ (gray) and $\epsilon = 3$ (orange). (d) Simulation results for normal stress against shear rate for the different brush-wall interaction.

The LFM experiment results[2] presented in Fig. 5.5(a) were performed with dextran brushes in HEPES and carried out at a constant load of 100 nN over a range (0.5-500

μm/s) of shear speeds while measuring the friction (shear) force. There are two regimes observed in the experiments. A "boundary-like" regime at low speeds for which the force is quite insensitive to rate, followed by a "hydrodynamic-like" regime at high speeds characterized by a significant increase of shear force with speed. Similar trends were observed in related experimental studies[3,4]. In Fig. 5.5(b) simulation results are presented for shear stress versus shear rate ($\dot{\gamma} = v/D$), again for a brush-against-wall system (Fig. 1b), where the model maintains a purely repulsive interaction (eq. 4.3 in Chapter 4 with $R_{cw} = 2^{1/6}\sigma$) between the polymer chains and the opposing wall. This model captures the experimental results at high speeds ("hydrodynamic-like" regime) but there is no sign of a boundary-like regime at low speeds. Assuming that the lowest speeds analyzed in the simulation correspond to speeds characterizing the boundary-like regime in the experiments, and in view of results to be discussed below, the absence of the boundary-like regime can be interpreted as being caused by the purely repulsive interaction between walls and brush in the simulations.

Previous experimental studies[17,18] suggest that lubrication in the boundary-like regime is not predominantly caused by the presence of solvent, but instead by asperity-asperity contacts or by the attractive van der Waals interaction between the polymer chains and the opposing wall in our case. Other experimental studies[19-22] focused on the effect of shear speed on boundary lubrication, the authors arguing that depending upon the time available for rupture and reformation of physical bonds at the contact, the coefficient of friction may exhibit various behaviors: it can increase, remain constant or even decrease with speed. We note that the terms "bond" or "link" are used synonymously for an attractive interaction that results in weak adhesion (cf. Ref. 22), while there is no chemical bond formation or rupture.

We then modified the interaction between the wall and the polymer chains to incorporate a short ranged attractive to the existing repulsive component reflecting van der Waals interactions also termed non-specific "bridging forces"[13] between polymer and wall. To this end, the cut-off (R_{cw}) is changed from $2^{1/6}$ (purely repulsive) to 2.5 (to incorporate an attractive tail) and the simulation is run for different depths of the corresponding potential well parameter (ϵ) in Eq. (4.3) in Chapter 4. Except for the polymer beads and wall particles, interactions among all other particles are kept unchanged. Previously, Galuschko et al.[23] used a large $\epsilon = 100$ value of the LJ attraction to attach end-monomers of chains permanently to the wall surface. The ϵ values explored by us are considerably smaller and tend to favor temporary rather than permanent contacts. Corresponding results for the shear stress versus shear rate are plotted in Fig. 5.5(c). Beyond a certain strength of the attractive interaction, a leveling-off in the shear stress (friction force) appears at low speeds, similar to that observed in experiments. For $\epsilon = 1$, leveling is not yet observed in shear stress (force), but the stress significantly increases with increasing ϵ for all speeds. At and beyond $\epsilon=3$ leveling-off in the shear stress (friction) is observed at lower speeds, resembling the experimental studies. See section AI.2 of the AppendixI for a comment on attractive interactions in brush-brush systems.

At low speeds there is almost no or very little tilt or stretching observed in the conformations of the polymer chains (Fig. 5.4(a)). In this case, the polymer chains have enough time to interact with individual sites of the structured counter-wall surface. The effective attractive interaction between the chains and counter-surface results in a constant shear stress (friction) at lower speeds. At high speeds, accompanied by significant stretch and tilt (Fig. 5.4(b)), there is insufficient time for the chains to form physical bonds with the wall particles. When the effective

attraction between polymer beads and wall particles is too weak or absent, the polymer chains slide easily relative to the counter wall. This 'hydrodynamic effect' at high speeds gives rise to a linear increase in shear stress (or friction) as a function of shear rate.

To be more specific, in the absence of attraction, the purely repulsive interaction between polymer chains and the counter wall-surface ensures a separation or gap between the chains and the wall surface at all shear rates. In reality this gap is filled by a thin solvent layer, while it is represented by implicit solvent in our simulation. In both cases lubrication is dominated by the solvent's behavior under shear and thus exhibits a "hydrodynamic-like" regime only. In other words, the absence of direct contact between polymer chains and the wall surface due to a purely repulsive interaction between counter wall-surface and polymer results in a missing "boundary-like" regime at lower speeds as well.

The normal stress against shear rate calculated from simulations is plotted for different brush-wall interactions in Fig. 5.5(d). Whereas the shear stress (Fig. 5.5(c)) increases with increasing attractive strength for all shear rates, the normal stress decreases with increasing strength of attraction between brush and opposing wall, again for all shear rates. This result is enforced by the constraint of constant separation (D). As the attraction between wall and polymer chains increases, less normal force is required to maintain a particular separation. Furthermore, the normal stress varies only moderately over a range of speeds, and starts to drop at speeds that already correspond to the hydrodynamic regime. As is well known from previous studies of coarse-grained models[24], we cannot simply calculate a dimensional speed using LJ units without introducing an extra correction factor that is related to the

relaxation time of the brush. This factor can be estimated by comparing the speeds at the onset of the plateaus in Figs. 5.5(a) and 5.5(c) and it comes as 10^4 approximately.

5.7 Effect of Wall-Roughness

The results in Section 5.6 were for a smooth wall against brush system. Figure 5.6 shows the effect of wall roughness on normal and stresses against speed at different separation distances between the explicit wall and brush bearing surfaces for a brush-against-wall system. Modelling of smooth and rough walls is discussed in Section 4.2**.** No significant change in the normal stress trend against speed was observed for a rough wall in comparison to smooth counter wall surface. At each separation the normal stress remains constant over the range of speeds studied for both the smooth and rough wall systems. An increase in normal stress is observed for both the systems with rough and smooth counter wall with decrease in separation. The normal stress at each separation is greater for the rough wall than for the smooth wall at all the shear speeds applied on the tethered beads. This can be explained as the effective separation between the brush-bearing surface and the explicit wall being less for the system with the rough wall than for the system with the smooth wall. All the beads in the smooth wall are placed at the D – 0.5 positions, whereas, in the rough wall, the beads are placed randomly at D – 1.5, D -1 or D - 0.5 positions.

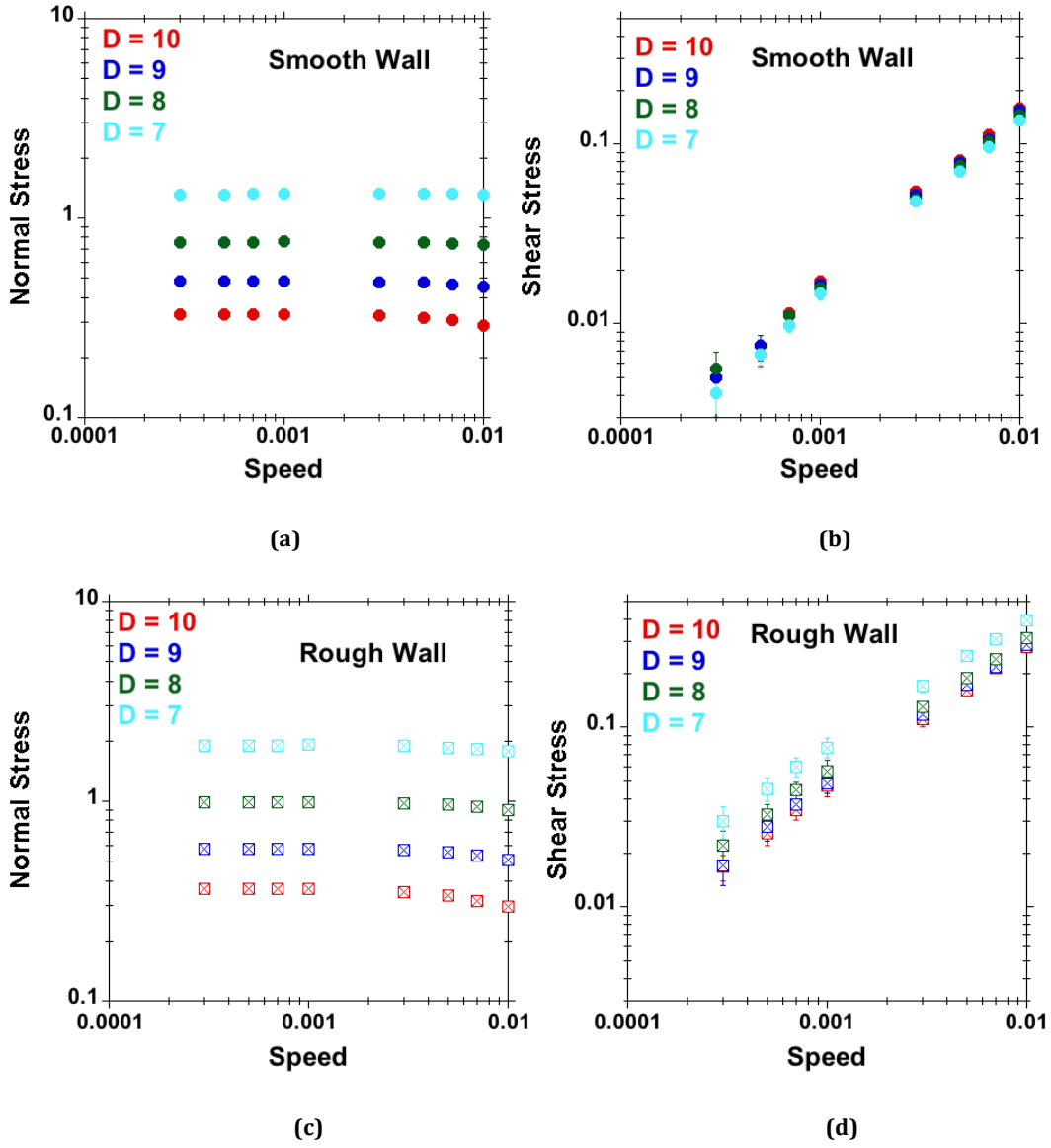

Figure 5.6: Stresses against shear speed: (a) normal stress against speed and (b) shear stress against speed for smooth wall, and (c) normal stress against speed and (d) shear stress against speed for rough wall. MD simulation results for LJ/12-6 cut-off, R_{cw} = 2.5 and depths of the potential well parameter, ϵ = 1 brush-wall interaction. MD simulation results for different separation D = 10 (red), D = 9 (blue), D =8 (green) and D = 7 (cyan). Simulations were performed for M = 20 chains, N = 50 beads per chain and grafting density, ρ = 0.075.

The effect of wall roughness is more predominant on the shear stress against speed at different separation distances. The trend in shear stress against speed is the same for all the separations for the systems having rough or smooth walls. The shear stress increases linearly (on a log-log scale) with increase in shear speeds for the both systems. At each speed, the shear stress is observed to be decreasing or remaining constant with decreasing separation for brush-against-wall systems having smooth walls. For the brush-against-wall system having a rough wall, the shear stress is

observed to be increasing with decreasing separation at each shear speed applied to the tethered beads. This can be explained in terms of an increase in contact area for the rough wall in comparison to the smooth wall (remember the beads in the smooth wall are placed at the $D - 0.5$ positions, whereas, in the rough wall, the beads are placed randomly at $D - 1.5$, D -1 or D - 0.5 positions). As the separation between brush and counter wall surface decreases, the area of contact between brush and wall at the interface increases (for the rough-wall system) and due to the attractive interaction between wall and brush (LJ/12-6 cut-off, $R_{cw} = 2.5$) this leads to an increase in shear stress.

5.8 Comparison with the Explicit-Solvent-Based Approach

In this section, a brief comparison of implicit and explicit solvent-based MD simulations is made. Modelling of good solvent quality using implicit and explicit solvent approaches was discussed in the Section 4.3. For the implicit solvent, a LJ/12-6 potential (eq 4.3) was used with a cut-off $R_{cw} = 2^{1/6}$. The explicit solvent was modeled using a modified LJ/12-6 potential (eq 4.4 & 4.5) with $\epsilon_{pp} = \epsilon_{ss} = 0$ and $\epsilon_{ps} = 0.4$.

5.8.1 Density Profile

Figure 5.7 shows the density profile from the implicit and explicit solvent based approach equilibrium MD simulations for a brush-against-wall system. The monomer concentration profiles for both the systems largely overlap and the brush height is also similar.

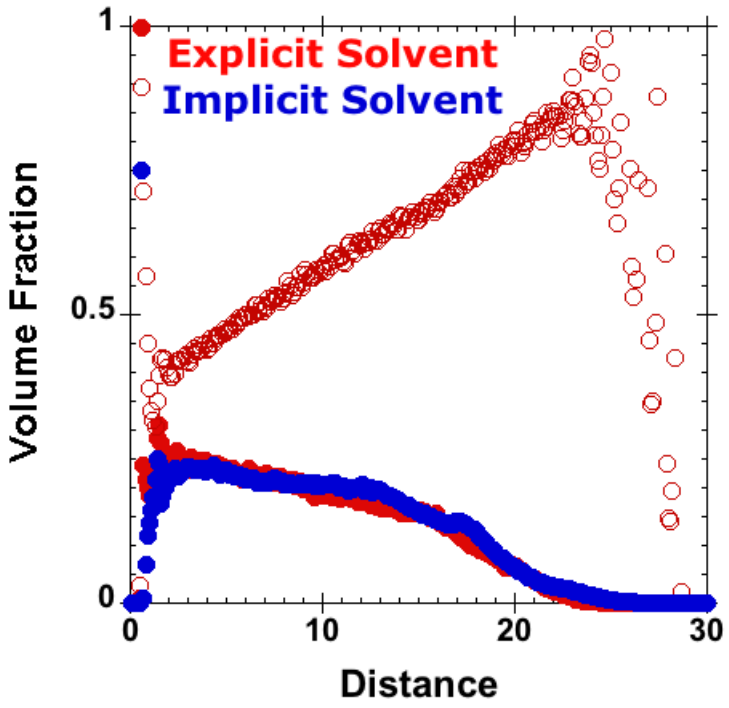

Figure 5.7: Comparison of implicit and explicit solvent based approaches. Blue circles present the monomer density profile obtained from implicit solvent based MD simulations and red filled and open circles present monomer and solvent density profiles, respectively, from explicit solvent based MD simulations. Simulations were performed for systems composed of M = 20 chains, N = 50 beads per chain, and at a grafting density ρ = 0.075. The tethered beads are at D = 0.5 positions and wall beads are at D = 28.5, 29 or 30.

5.8.2 Speed Dependence

Figure 5.8 shows results for shear and normal stresses against speed obtained from implicit and explicit solvent based nonequilbrium MD simulations at a fixed separation, D = 8. The normal stress is found to remain constant for both the systems (implicit and explicit solvent based simulation) over the range of speeds studied and normal stress was higher for the explicit solvent at all the speeds in comparison to the implicit solvent based system. It is important to mention here that normal stress calculated from explicit-solvent-based simulation contains solvent pressure as well. The shear stress is found to be increasing linearly (on a log-log scale) with speed, for both systems. At lower speed, S $\leq$ 0.001, the system with explicit solvent shows a higher shear stress compared with the implicit solvent case but only within the range of error bars. Galuschko et al.[23] compared their results for implicit and explicit solvent

based nonequilibrium MD simulations and found that the explicit solvent-based approach tends to show lower coefficients of friction (ratio of shear and normal stress) than the implicit solvent based approach for systems with same grafting density. They carried out their studies for a brush-against-brush system and also found that results from implicit and explicit solvent-based approaches converge at higher grafting density.

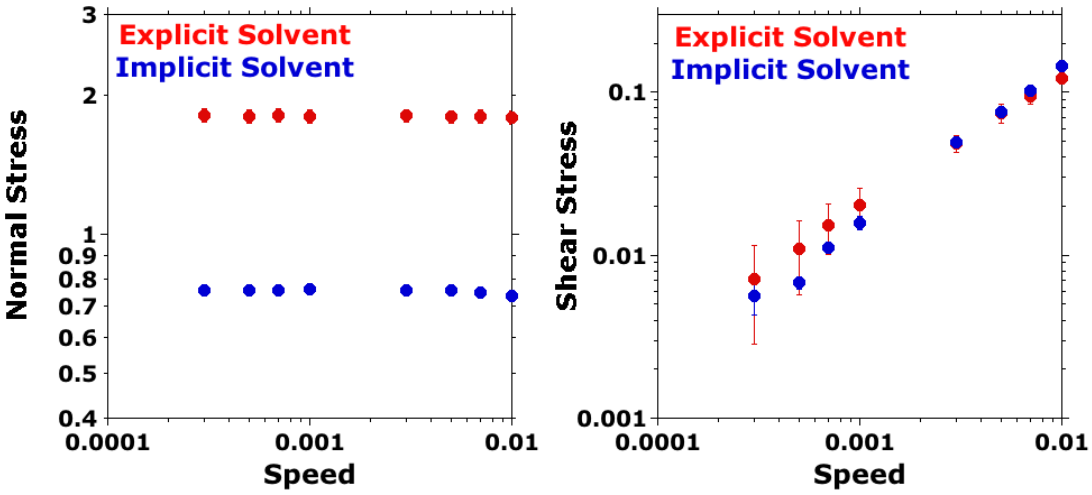

Figure 5.8: (a) Normal and (b) shear stresses against speed from implicit solvent (blue circles) and explicit solvent (red circles) based simulation. Simulation were done for M = 20 chains, N = 50 beads per chain and grafting density, ρ = 0.075.

5.8.3 Separation Dependence

In Fig. 5.9 results from implicit and explicit solvent based nonequilibrium MD simulations for normal and shear stresses against separation distance are compared at a fixed shear speed, S = 0.001, which was applied on the tethered beads in brush-against-wall systems.

The normal stress is found to be increasing with decreasing separation distance for both the implicit and explicit solvent based simulations. The normal stress from explicit solvent-based simulation was higher in comparison to that for implicit solvent-based simulation at all separations. From the density profiles in Fig. 5.7 we

extract basically identical equilibrium brush heights h ~25 for both systems. At the onset of brush deformation (D ~25) the normal stress value in the implicit solvent system remains close to zero whereas a non-vanishing stress of magnitude 0.8 is observed in the explicit solvent based system.

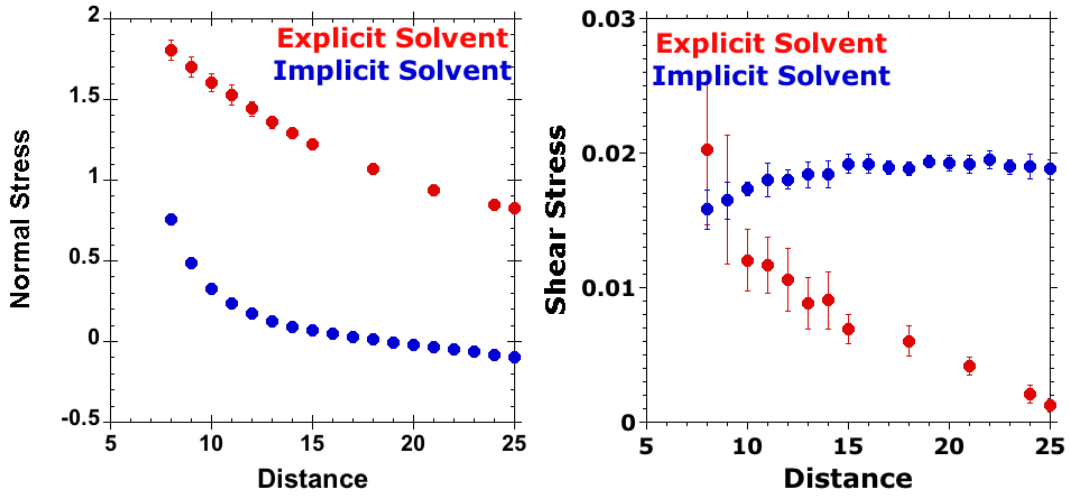

(a) (b)

Figure 5.9: (a) Normal and (b) shear stresses against separation distance from implicit solvent (blue circles) and explicit solvent (red circles) based simulation. Simulations were performed for M = 20 chains, N = 50 beads per chain, grafting density, ρ = 0.075 and shear speed, S = 0.001.

The shear-stress values from implicit solvent based simulations do not show any significant change upon variation of the separation between the surfaces, whereas it increases with decreasing separation distance between the brush-carrying surface and the counter-wall surface in the explicit solvent based simulation. When shear stress is plotted against normal stress (not shown here), in the implicit-solvent based system, the shear stress remains constant with increasing normal stress (decrease in separation) while it increases linearly with increasing normal stress (decrease in separation) for the explicit solvent case. The trends observed in the latter case are consistent with our experimental results in Chapter 3 and previously published experimental results[2,25].

With careful selection of potential parameters, similar concentration profiles (of monomers) and brush height (h) were ensured for both the implicit and explicit solvent-based simulations. From the comparison of implicit and explicit solvent based simulations we see that they show similar trends (for both normal and shear stresses) in speed-dependent studies. In separation-dependent (load-dependent) studies, explicit-solvent-based simulation shear stress results reflect the trends in the experimental work, whereas in the implicit solvent based simulations, shear stress did not show any significant effect of separation (load) over the range of separations and speeds studied.

5.9 Conclusions

In an attempt to understand the underlying principles and molecular mechanisms in polymer-brush-based aqueous lubrication, we have modeled polymer brushes using a multibead-spring, coarse-grained molecular-dynamics-simulation technique. We calculated the simulation parameters based on selected experimental results for dextran (5 kDa). Using these parameters, we carried out both equilibrium and nonequilbrium (sliding) molecular-dynamics simulations and compared the results with available theoretical and experimental results: (i) Density-profile (volume fraction) results were compared with SCF theory results, and found to be in good agreement. (ii) Compression-curve results obtained from MD simulations were found to be in good agreement with SFA experimental results except at the lowest force values, which may be due to experimental polydispersity effects. (iii) Shear stresses at different shear rates calculated from nonequilbrium MD simulations were compared with shear (friction) forces vs. speed, measured by colloidal-probe LFM. Here, we observed that when the interaction between polymer chains and the wall was modified

to incorporate an attractive force, the simulation was able to capture the experimental results in all regimes.

This work paves the way for predicting polymer-brushed-based lubrication for different brush architectures, chain lengths, grafting densities and under different experimental conditions (load and speed). When correlated with the experimental data, the proposed model is able to provide guidance in designing dextran-brush-based lubrication systems with desired tribological characteristics (combination of load, speed and friction behavior for different chain lengths and grafting densities). The simple model used here can be applied further to study the behavior of various polymer brushes under different solvent conditions, and the unmodified approach can be used to obtain model parameters, as well as rescaled results, without performing additional simulations.

5.10 References

(1) Espinosa-Marzal, R. M.; Nalam, P. C.; Bolisetty, S.; Spencer, N. D. Impact of Solvation on Equilibrium Conformation of Polymer Brushes in Solvent Mixtures. *Soft Matter* **2013**, *9* (15), 4045.

(2) Nalam, P. C.; Ramakrishna, S. N.; Espinosa-Marzal, R. M.; Spencer, N. D. Exploring Lubrication Regimes at the Nanoscale: Nanotribological Characterization of Silica and Polymer Brushes in Viscous Solvents. *Langmuir* **2013**, *29* (32), 10149–10158.

(3) Tsujii, Y.; Nomura, A.; Okayasu, K.; Gao, W.; Ohno, K.; Fukuda, T. AFM Studies on Microtribology of Concentrated Polymer Brushes in Solvents. *J Phys. Conf. Ser.* **2009**, *184* (1), 012031.

(4) Nomura, A.; Okayasu, K.; Ohno, K.; Fukuda, T.; Tsujii, Y. Lubrication Mechanism of Concentrated Polymer Brushes in Solvents: Effect of Solvent Quality and Thereby Swelling State. *Macromolecules* **2011**, *44* (12), 5013–5019.

(5) Perrino, C. Poly(L-Lysine)-G-Dextran (PLL-G-Dex): Brush-Forming, Biomimetic Carbohydrate Chains That Inhibit Fouling and Promote Lubricity. **2009**.

(6) Heuberger, M.; Drobek, T.; Spencer, N. D. Interaction Forces and Morphology of a Protein-Resistant Poly(Ethylene Glycol) Layer. *Biophys. J.* **2005**, *88* (1), 495–504.

(7) Pasche, S. Mechanisms of Protein Resistance of Adsorbed PEG-Graft Copolymers, ETH, Zurich: Zurich, 2004.

(8) Zhang, X.; Wang, J. C.; Lacki, K. M.; Liapis, A. I. Construction by Molecular Dynamics Modeling and Simulations of the Porous Structures Formed by Dextran Polymer Chains Attached on the Surface of the Pores of a Base Matrix: Characterization of Porous Structures. *J. Phys. Chem. B* **2005**, *109* (44), 21028–21039.

(9) de Belder, A. N. *Dextran*, AA. Amersham Biosciences, 2003.

(10) de Beer, S. Switchable Friction Using Contacts of Stimulus-Responsive and Nonresponding Swollen Polymer Brushes. *Langmuir* **2014**, *30* (27), 8085–8090.

(11) Halperin, A.; Kröger, M.; Zhulina, E. B. Colloid-Brush Interactions: the Effect of Solvent Quality. *Macromolecules* **2011**, *44* (9), 3622–3638.

(12) Irving, J. H.; Kirkwood, J. G. The Statistical Mechanical Theory of Transport Processes. IV. the Equations of Hydrodynamics. *J. Chem. Phys.* **1950**, *18* (6), 817–829.

(13) Israelachvili, J. *Intermolecular and Surface Forces*; Academic Press: London, 1992.

(14) Grest, G. S. Computer Simulations of Shear and Friction Between Polymer Brushes. *Curr. Opin. Colloid Interface Sci.* **1997**, *2* (3), 271–277.

(15) Milner, S. T.; Witten, T. A.; Cates, M. E. Effects of Polydispersity in the End-Grafted Polymer Brush. *Macromolecules* **1989**, *22* (2), 853–861.

(16) Ruths, M.; Johannsmann, D.; Rühe, J.; Knoll, W. Repulsive Forces and Relaxation on Compression of Entangled, Polydisperse Polystyrene Brushes. *Macromolecules* **2000**, *33* (10), 3860–3870.

(17) Kaneko, D.; Oshikawa, M.; Yamaguchi, T.; Ping Gong, J.; Doi, M. Friction Coefficient Between Rubber and Solid Substrate –Effect of Rubber Thickness–. *J. Phys. Soc. Jpn.* **2007**, *76* (4), 043601.

(18) Wang, W.-Z.; Hu, Y.-Z.; Liu, Y.-C.; Wang, H. Deterministic Solutions and Thermal Analysis for Mixed Lubrication in Point Contacts. *Tribol. Int.* **2006**, *40* (4), 687–693.

(19) Schallamach, A. A Theory of Dynamic Rubber Friction. *Wear* **1963**, *6* (5), 375–382.

(20) Campen, S.; Green, J.; Lamb, G.; Atkinson, D.; Spikes, H. On the Increase in Boundary Friction with Sliding Speed. *Tribol. Lett.* **2012**, *48* (2), 237–248.

(21) Barel, I.; Urbakh, M.; Jansen, L.; Schirmeisen, A. Multibond Dynamics of Nanoscale Friction: the Role of Temperature. *Phys. Rev. Lett.* **2010**, *104* (6), 066104.

(22) Drummond, C.; Israelachvili, J.; Richetti, P. Friction Between Two Weakly Adhering Boundary Lubricated Surfaces in Water. *Phys. Rev. E* **2003**, *67* (6), 066110.

(23) Galuschko, A.; Spirin, L.; Kreer, T.; Johner, A.; Pastorino, C.; Wittmer, J.; Baschnagel, J. Frictional Forces Between Strongly Compressed, Nonentangled Polymer Brushes: Molecular Dynamics Simulations and Scaling Theory. *Langmuir* **2010**, *26* (9), 6418–6429.

(24) Kröger, M. *Models for Polymeric and Anisotropic Liquids*; Berlin Heidelberg, 2005; Vol. 675.

(25) Klein, J.; Perahia, D.; Warburg, S. Forces Between Polymer-Bearing Surfaces Undergoing Shear. *Nature* **1991**.

Chapter 6

Brush-Brush Systems under Shear: Explicit-Solvent-Based Study

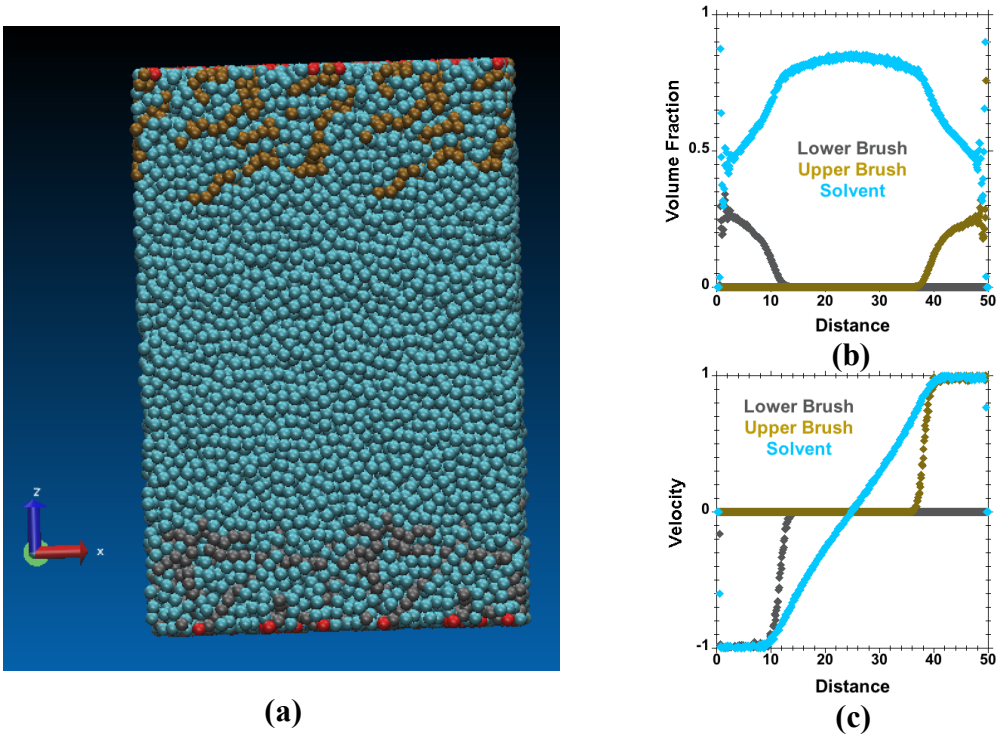

Figure 6.1: (a) Schematic of brush-against-brush system with explicit solvent, (b) Density profile and (c) Velocity profile for brush-against-brush system (M = 20, N = 30 and ρ = 0.075) under shear with a speed of 1 applied on tethered beads on both sides in opposite directions at separation D=50. The simulation was performed at very high shear speed, S = 1, to obtain a clear trend, otherwise simulations were carried out at a maximum speed of S = 0.1

6.1 Simulation Details

We have carried out simulations for the brush-against-brush model system described in Chapter 4 (Fig. 6.1). Three types of beads—non-tethered, tethered and solvent—are used. We have performed simulations with randomly grafted polymer chains on a flat surface. The system consists of M = 20 chains on each side, with each chain having N = 30 beads and grafting density, ρ = 0.015, ρ = 0.025, ρ = 0.075 and ρ = 0.15 (all in LJ units). The simulations are carried out for different values of chain-stiffness, K_s = 0, 1 and 3. For our simulations we have used the purely repulsive potential for polymer-polymer ($\epsilon_{pp} = 0$) interaction and solvent-solvent interaction ($\epsilon_{ss} = 0$). For

polymer-solvent interaction we have used ($\epsilon_{\mathrm{ps}} = 0.4$) and using this combination we have ensured good solvent quality. The cut off, z_c = 0.5 was used for the wall potential (Eq. 4.2) in **Chapter 4**.

The total number of beads in the simulation box is such that the number density of beads is approximately 0.8 at each separation, i.e. (number of solvent beads + number of polymer beads)/ (volume by substrate surfaces on both sides) ~ 0.8. As the separation decreases, certain numbers of solvent beads are removed to maintain a total bead density of approximately 0.8.

At different separations *D* between the polymer-chain-bearing surfaces, the polymer-brush system was allowed to equilibrate before steady shear was applied by moving the tethered beads on both sides with the same prescribed velocity but in opposite directions, keeping the separation constant during each run of shear speeds. At each separation and speed, the stress tensor was calculated using the Irving-Kirkwood expression.[1,2] The temperature was maintained constant at T = 1.2 using a temperature-rescale thermostat after removing the bias speed. Two kinds of studies were carried out: (i) speed-dependent: different speeds while keeping the separation constant and (ii) separation-dependent: different separations while keeping a fixed speed.

For the speed-dependent studies, the simulations are carried out over a range of shear speeds 0.00015-0.05 at fixed separations. The simulations were done for different numbers of time steps at different speeds for the speed-dependent studies. At all speeds, the data for first 500,000 time steps at time step $\Delta t = 0.001$ were ignored. Then the simulations were run with $\Delta t=0.0025$ for 300,000 time steps (data for first 100,000 time steps were ignored and data for next 200,000 time steps were recorded for analysis) at speed S=0.05 and for 99,900,000 time steps (data for first 33,300,000)

time steps were ignored and for next 66,600,000 time steps were recorded for analysis) at speed S=0.00015.

$$\tau_R \sim N^{2.31}\left(\frac{D}{\rho_g}\right)^{-0.31} \qquad 6.1$$

Table 6.1: Relaxation time (τ_R) and Weissenberg number (Wi) at different grafting densities for speed-dependent studies at different separations. τ_R is calculated using equation 6.1[3,4].

Grafting Density (ρ)	Speed (S)	Separation (*D*)	Relaxation time τ_R[4]	Weissenberg number Wi
0.075	0.00015-0.05	20	457	0.00343 – 1.14
		30	403	0.002 - 0.67
		40	368	0.0014 - 0.46
0.15		30	499	0.0025 - 0.833

Table 6.2: Relaxation time (τ_R) and Weissenberg number (Wi) at different grafting densities for separation-dependent studies at a fixed speed.

Grafting Density (ρ)	Speed (S)	Separation (D)	Relaxation time τ_R[4]	Weissenberg number Wi
0.015	0.001	12 - 24	325 - 262	0.027-0.011
0.025		13 - 26	371 - 299	0.028-0.012
0.075		15 - 30	499 - 403	0.033-0.013
0.15		18 - 36	585 - 472	0.033-0.013

Simulations for each separation (D) and speed (S) were repeated using 10 different initial configurations. The mean value from these 10 runs is reported with standard deviations (e.g. Fig. 6.2(a)).

RESULTS AND DISCUSSION

6.2 Effect of Separation Distance (D)

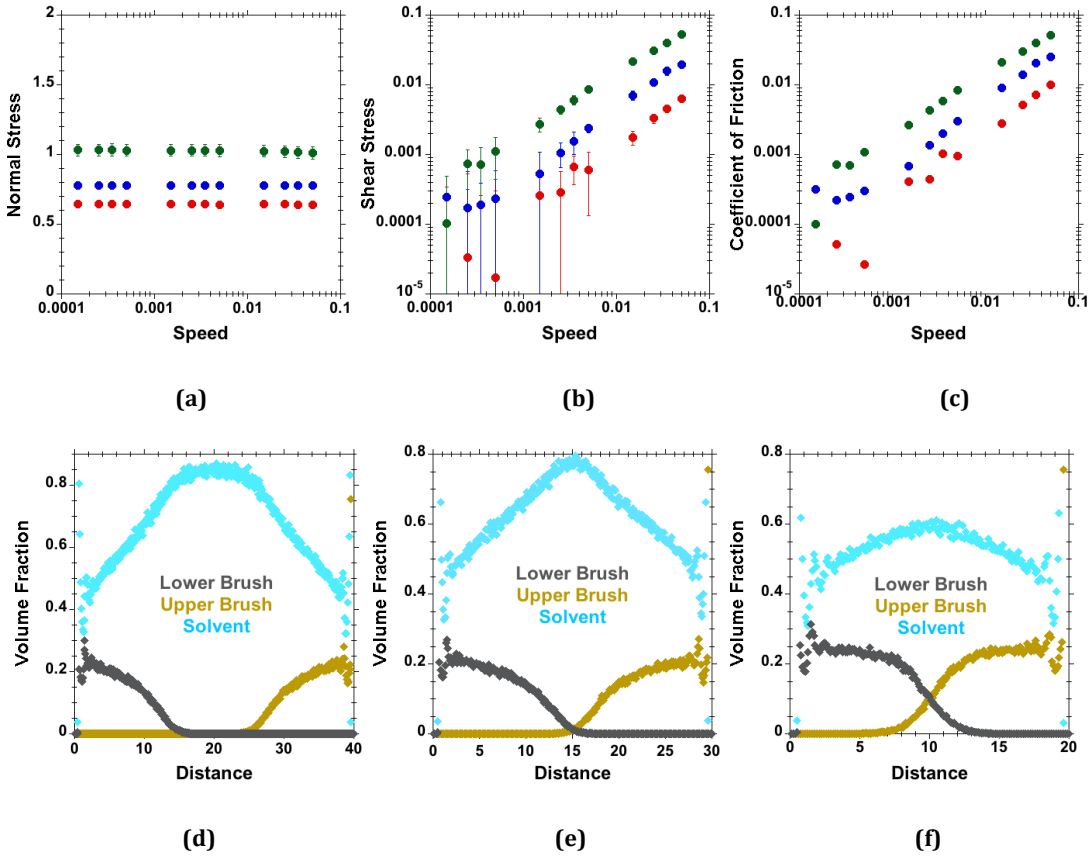

Figure 6.2 Effect of separation distance D (red dots for D=40, blue dots for D=30 and green dots for D=20) for number of chains on each side, M=20, number of beads per chain, N=30, grafting density, ρ=0.075, flexible chain, K_s=0 and good solvent quality (a) Normal stress against Speed, (b) Shear stress against speed, (c) Coefficient of friction against speed, density profiles of solvent (cyan dots), lower polymer-chains (grey dots) and upper polymer-chains (brown dots) at (d) D=40, (e) D=30, and (f) D=20.

In Fig. 6.2 shear and normal stresses are plotted against shear speed at different separations (D=40, D=30 and D=20). The normal stress is found to remain constant at all speeds at each separation but increases with decreasing gap size. We observe an increase in friction (shear) forces with decreasing gap size or increasing normal load at all investigated speeds. Similar trends were observed in previous experimental

studies.[5-7] Kinetic coefficients of friction (ratio of shear and normal stress) also increase with increase in speed and with increase in normal stress. Fig. 6.2 further shows the density profiles at the corresponding separations for uncompressed brushes (D=40), marginal compressed brushes (D=30) and highly compressed brush (D=20) where interpenetration is observed. At separation D = 40, the grafted opposite polymer chains are not interacting with each other and there is layer of solvent in between the polymers leading to a tribological/friction behavior that is dominated by the friction behavior of solvent, implying a very low or immeasurable friction coefficient[8]. As surfaces are brought nearer, the opposite chains interact with each other and friction increases. With further compression, the penetration between the opposite chains increases and it leads to further increase in friction.

6.3 Effect of Grafting Density

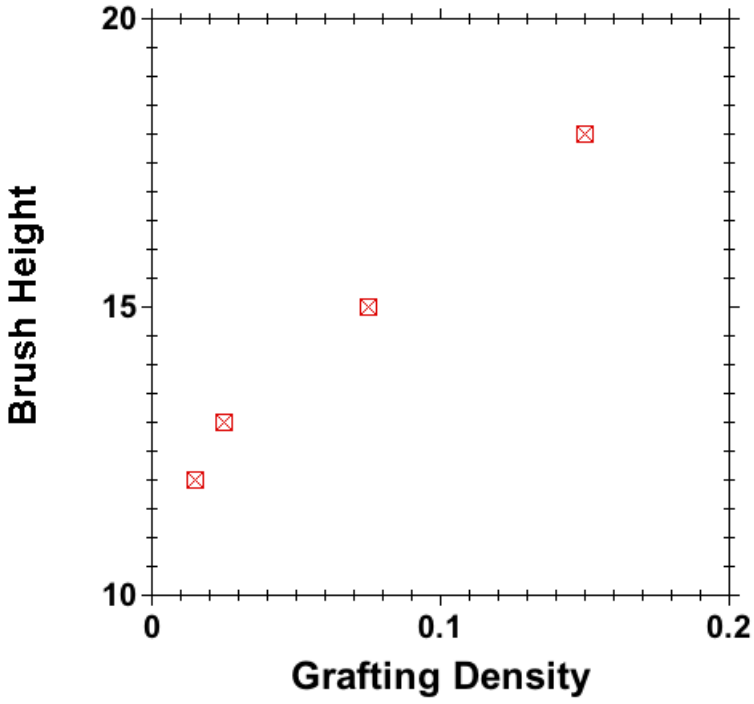

Figure 6.3: Brush height (h) against grafting density (ρ) for M=20, N=30 and good solvent quantity.

Figure 6.3 shows the effect of grafting density on brush height (h) as calculated from density profiles for each different grafting density at large separation between brush

bearing surfaces. In the following section we will study the effect of grafting density on the tribological response of polymer brushes.

6.3.1 Speed-dependent Studies

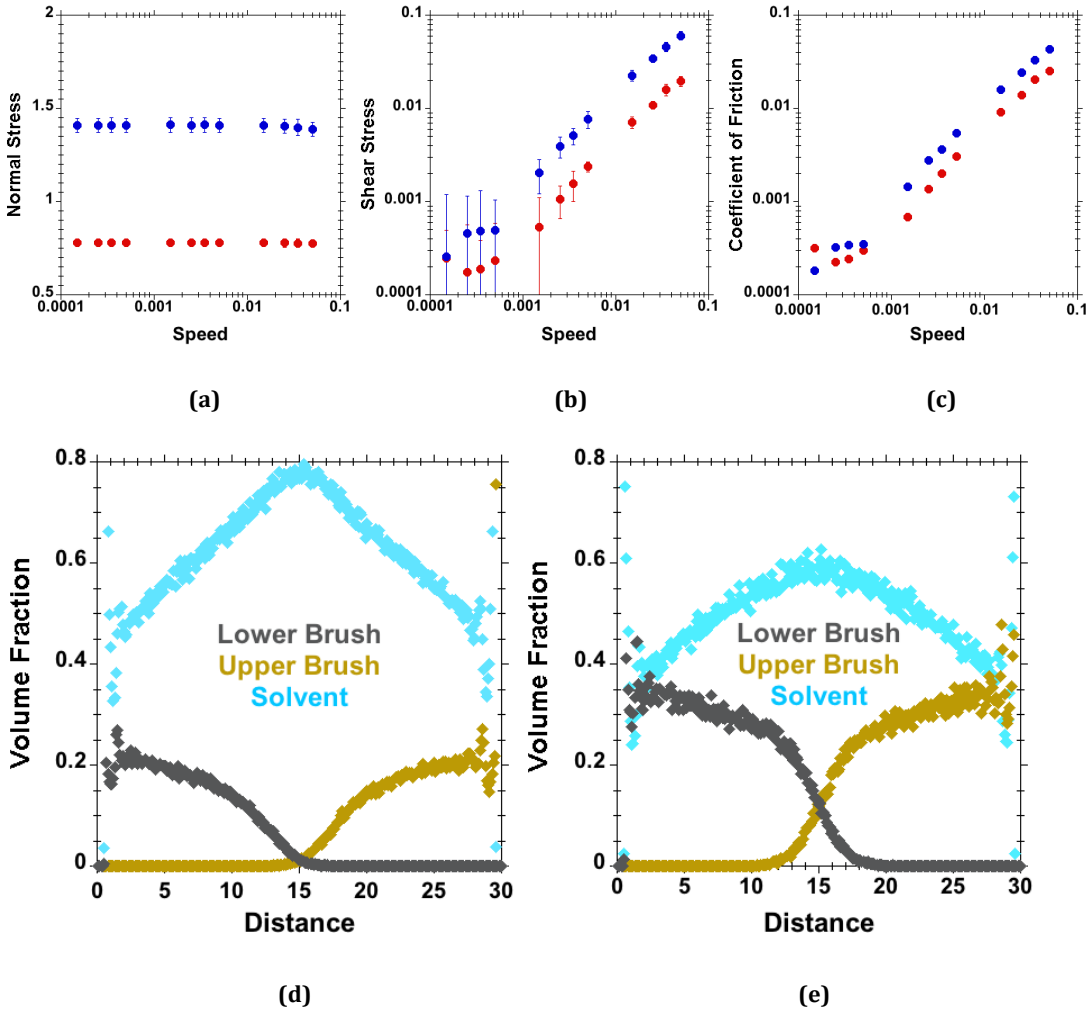

Figure 6.4 Effect of grafting density (red dots for ρ = 0.075 and blue dots for ρ = 0.15) for M=20, N=30, K_s=0, D=30 and good solvent quality (a) Normal stress against speed, (b) Shear stress against speed, (c) Coefficient of friction against speed; Density profiles of solvent (cyan dots), lower polymer-chains (grey dots) and upper polymer-chains (brown dots) for (d) ρ=0.075, and (e) ρ=0.15.

In Fig. 6.4, normal and shear stresses are plotted against speeds for a fixed separation D = 30 for different grafting densities ρ = 0.075 and ρ = 0.15. Here we observe an increase in normal and shear forces with increase in grafting density at all shear speeds. In the shear stress against speed curve (Fig. 6.4(b)) we have observed a typical "boundary regime" like behavior for brush-brush systems at lower speeds, which was observed in previous experimental studies[6,7]. For the corresponding

grafting densities and separation (D = 30), we have plotted density profiles of solvent and polymer chains. Here we observe that at lower grafting density (ρ = 0.075) the polymer chains are marginally compressed or uncompressed but at higher grafting density (ρ = 0.15) for the same separation (D = 30) the brushes are compressed and interpenetration between opposite chains is observed. This higher interpenetration between chains causes higher friction to be observed at higher grafting density. Galuschko et al.[3] have observed an increase in friction with increase in grafting density at constant separation distance for a brush-against-brush system with a dissipative particle dynamics (DPD) thermostat.

6.3.2 Separation-Dependent Study

Here we have run the simulations at different separations between polymer-bearing surfaces at a constant speed, S = 0.001 applied in opposing directions on tethered beads on both sides for systems with different grafting densities. The simulations were done for different numbers of timesteps at each grafting density, as shown in Table 6.3. Data at each timestep, $\Delta t = 0.001$ and $\Delta t = 0.002$ were ignored and only at $\Delta t = 0.0025$ were recorded for analysis.

Table 6.3: Number of timesteps for simulations carried at different grafting densities for separation-dependent studies at fixed speed=0.001.

Grafting Density ρ	**Speed (S)**	**Number of timesteps**		
		Δt = 0.001	**Δt = 0.002**	**Δt = 0.0025**
0.015	0.001	500,000	11,000,000	22,000,000
0.025			10,000,000	20,000,000
0.075			6,250,000	12,500,000
0.15			6,250,000	12,500,000

It is important to mention here that the critical grafting density ($\rho^* = 1/\pi R_g^2$)[3] for chains having $N = 30$ beads is $\rho^* \approx 0.025$. We have considered four grafting densities of $\rho = 0.015$ (less than critical density), $\rho = 0.025$ (equal to critical grafting density), $\rho = 0.075$ (3 times the critical grafting density) and $\rho = 0.15$ (6 times the critical grafting density). Since the stresses calculated at different grafting densities are not comparable, I have presented the results for shear stress (σ_{xz}) against normal stress (σ_{zz}) for each grafting density in the following four plots.

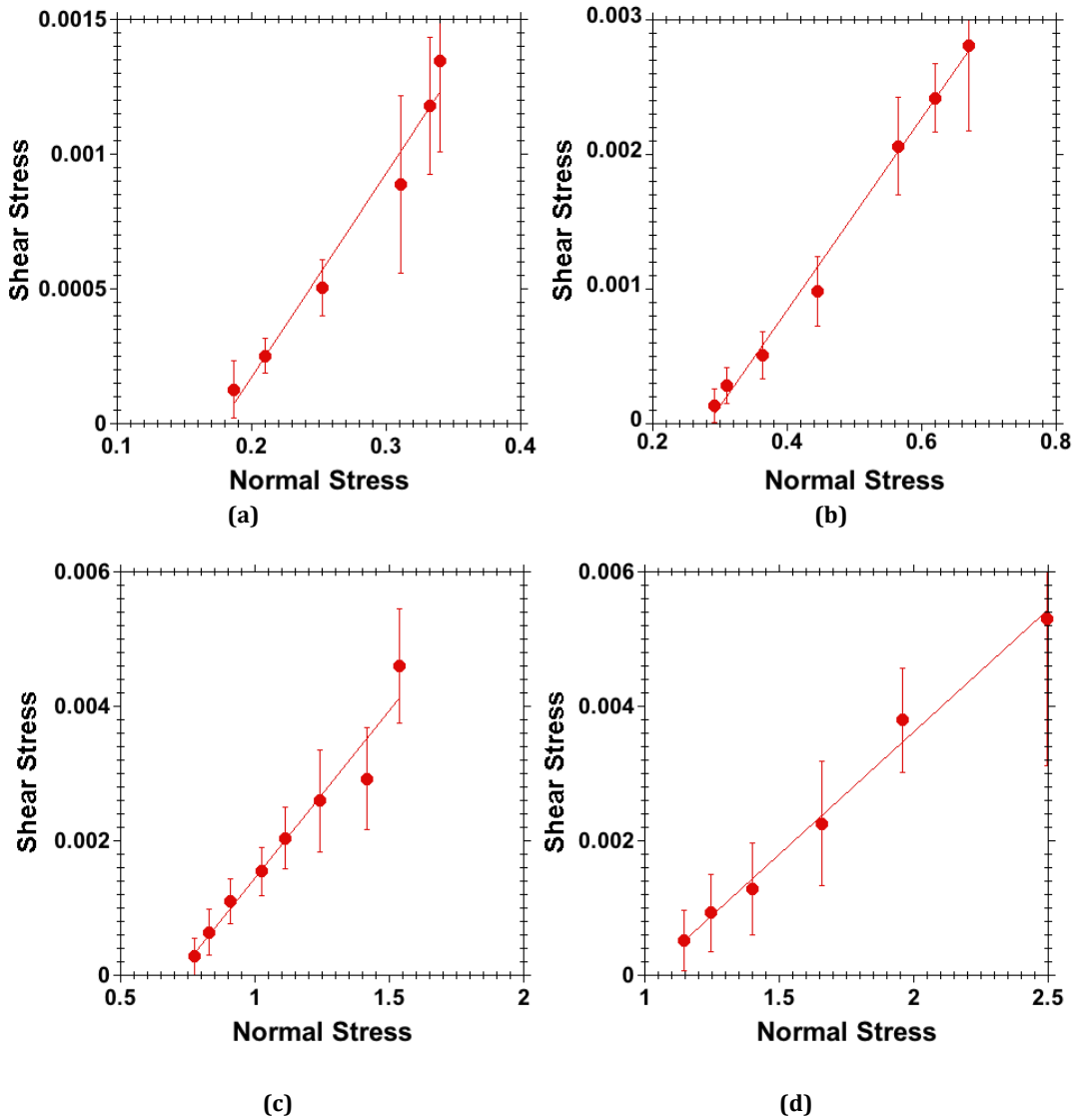

Figure 6.5 Effect of grafting density for M=20, N=30, K=0 and good solvent quality, Shear Stress against Normal Stress for (a) ρ = 0.015, (b) ρ=0.025, (c) ρ = 0.025 and (d) ρ = 0.075.

In Fig. 3 (a), (b), (c) and (d) are plotted results of σ_{xz} against σ_{zz} calculated over different separations applying shear speeds of 0.001 (in opposing directions) on

tethered beads on each sides for $\rho = 0.015$, $\rho = 0.025$, $\rho = 0.075$ and $\rho = 0.15$ systems, respectively. It is important to state here that in Fig. 6.5, results for all the grafting densities are plotted for $D/2h < 1$ (D is separation between the polymer bearing surfaces and h is the equilibrium brush heights). The shear stress against normal stress data was found to have linear dependence. Fitting a straight line (considering the error in each value[9]) to all the curves, the coefficient of friction was calculated from the slope of the curve, as was also done in experiments[8]. The coefficient of friction thus obtained from the slope of the curves is plotted against the corresponding grafting densities in Figure 6.6.

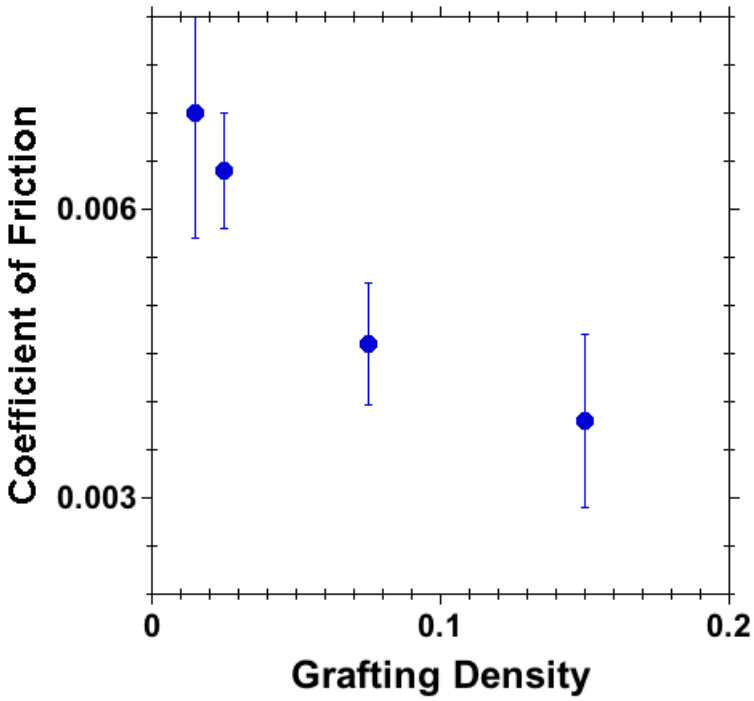

Figure 6.6 Coefficient of friction against grafting density (ρ) for *M*=20, *N*=30 and good solvent quality.

We observe a decrease in coefficient of friction with increase in grafting density. Similar trends were observed in experiments[10] where at a moderate load/pressure the system with highest grafting density exhibits lowest friction. As the applied load increases, a "transition load" was observed at each grafting density in the

experimental work[10]. Above the transition load, the friction was found to be increasing with increase in grafting density.

In our simulation studies we have observed two trends: (i) increase in friction with increase in grafting density (Fig. 6.4) at a fixed separation D = 30 and (ii) decrease in friction with increase in grafting density (Fig.6.6) at a fixed speed, S=0.001, in the separation-dependence study. The experimental[10] results have two clear regimes: (i) at lower load friction decreases with increase in grafting density and (ii) at higher load (beyond "transition load" regime) friction increase with increase in grafting density.

We can explain it as follows: The systems with higher grafting densities have higher repulsive forces acting between opposite chains, and thus at moderate pressure the system with higher grafting density has a solvent layer between the brushes[11] which results in less friction observed. But at the same load the system with lower grafting density polymer brushes cannot support the load and there is interpenetration between chains, which results in higher friction. But as the normal stress acting increases further, the system with higher grafting density also has interpenetration between opposite chains and because of higher grafting density, there is more interaction between opposite polymer chains, which results in higher friction at higher load when compared to the system with lower grafting density. The simulation has limitations in the sense that we cannot see a clear "transition load" in the presented simulation work over the studied separations between polymer-bearing surfaces.

6.4 Effect of Stiffness

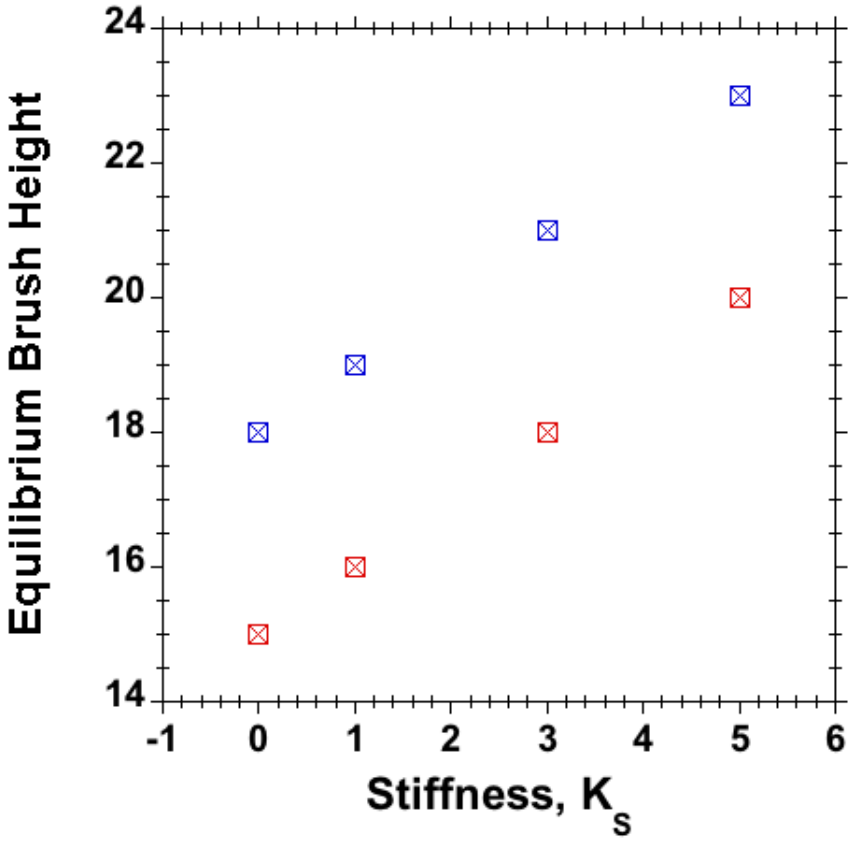

Figure 6.7 Equilibrium brush height against chain stiffness (K_S) at different grafting density ρ=0.075 (red squares) and ρ=0.15 (blue squares) for M=20, N=30 and good solvent quality.

The equilibrium brush height (h) of polymer brushes can be calculated from density profiles when the polymer chains grafted on opposite surfaces are not in contact with each other. In Fig. 6.7 the equilibrium brush height (h) is plotted as a function of chain stiffness (K) for different grafting densities (ρ = 0.075 and ρ = 0.15). We have observed an increase in equilibrium brush height (h) with increase in chain stiffness (K) for different grafting densities.

6.4.1 Speed dependence

In Fig. 6.8 the normal and shear stresses are plotted against shear speed at a separation of D = 30 for different chain stiffnesses. We have observed an increase in normal stress with increase in chain stiffness, whereas the shear stress decreases with

increasing chain stiffness. An increase in normal stress and decrease in shear stress with increase in chain stiffness leads to the conclusion that the coefficient of friction decreases with increase in chain stiffness over the range of stiffness studied.

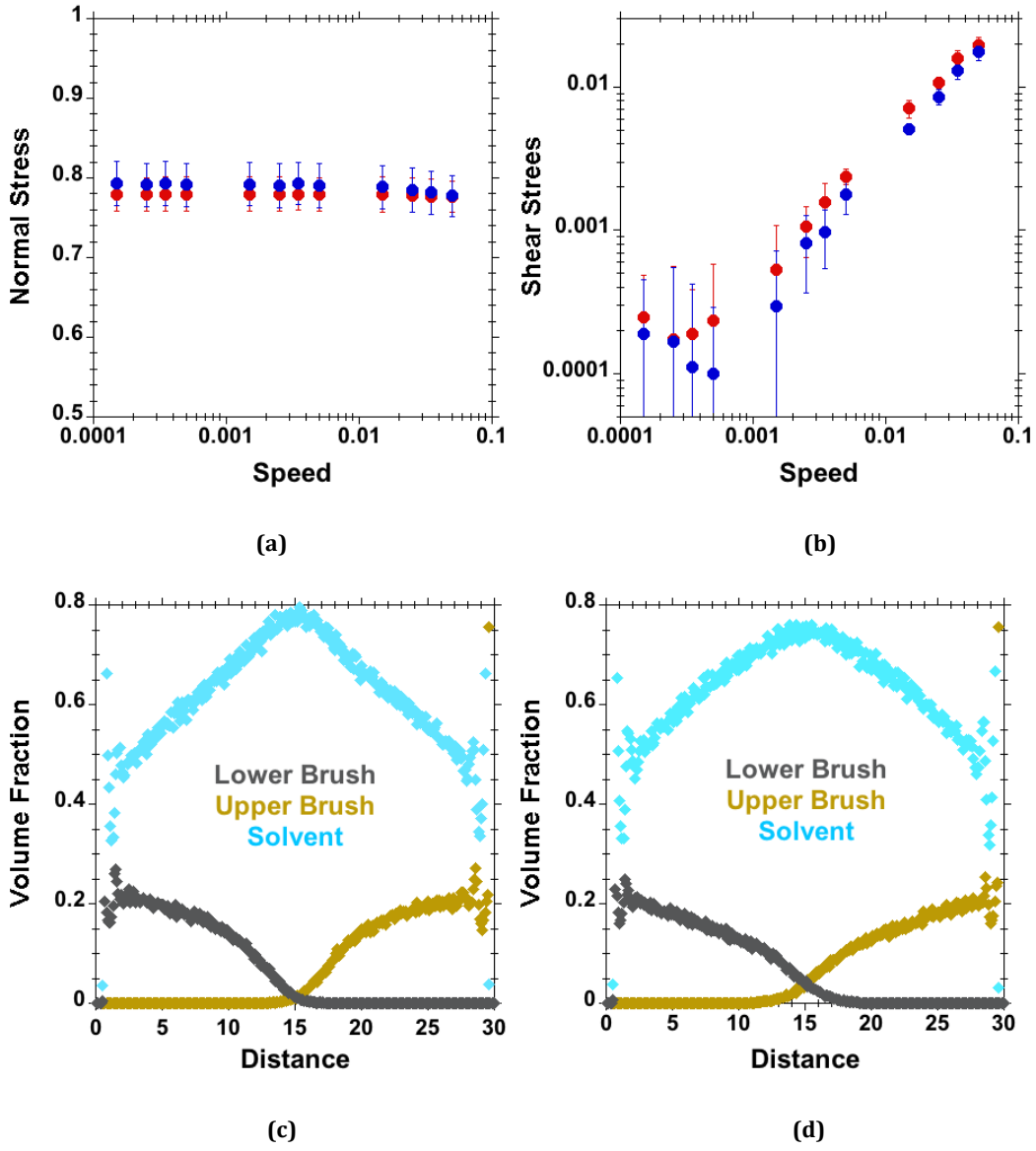

Figure 6.8 Effect of chain stiffness (red dots for K_s = 0 and blue dots for K_s = 3) for M=20, N=30, ρ=0.075, D=30 and good solvent quality (a) Normal stress against speed, (b) Shear stress against speed, Density profiles of solvent (cyan), lower polymer-chains (grey) and upper polymer-chains (brown) for (c) K_s=0, and (d) K_s=3.

Here again we have observed "boundary-regime" like behavior at lower speeds in the shear-stress-vs-shear-speed representation (Fig. 6.8(b)). The corresponding density-profile plots show that flexible (K_s=0) polymer chains are marginally compressed or

uncompressed at separation D=30 but for stiffer chains (K_s=3), interpenetration is observed for the same separation D=30.

6.4.2 Separation Dependence

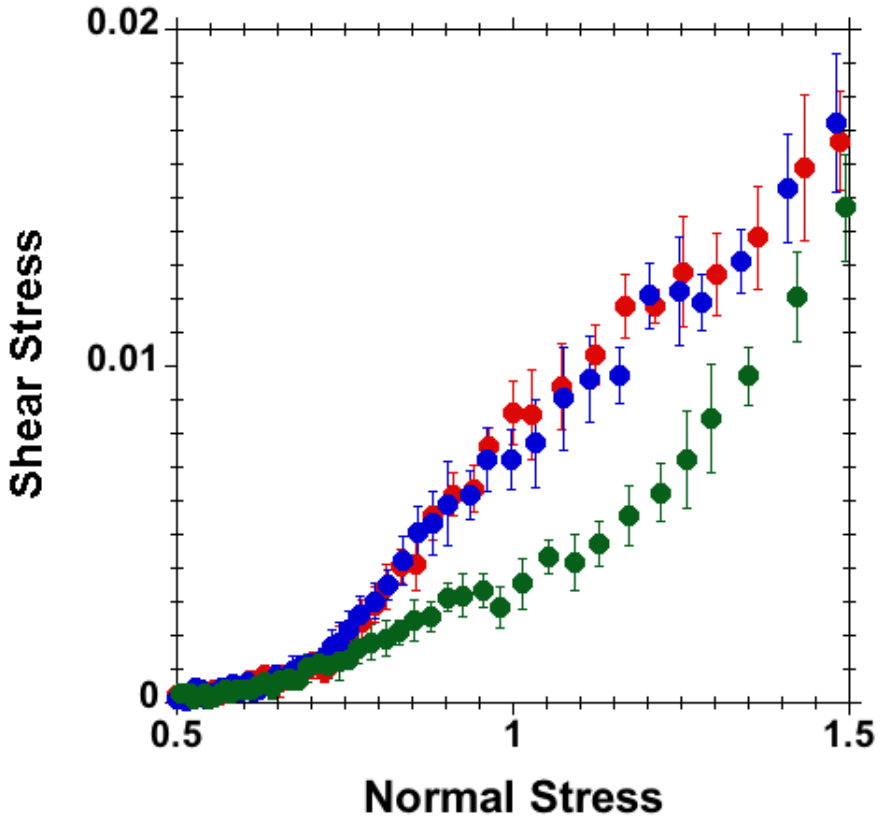

Figure 6.9: Shear stress against normal stress for M = 20, N = 30, ρ = 0.075 and good solvent conditions for different chain-stiffness values, K=0 (red), K=1 (blue) and K=3 (green).

In Fig.6.9 we have again plotted shear stresses against normal stresses obtained for different chain stiffness values by running the simulation over different separations between the polymer-bearing surfaces when a constant shear speed, S = 0.005, was applied on tethered beads on both sides but in opposite directions. As in the speed-dependent studies, we observe a lower shear stress at a given normal stress for systems with chains of higher chain-stiffness values. The normal stress vs distance plot (not shown here) does not show any effect of chain stiffness, but when we plot the shear stress vs distance (again not shown here) we observe a decrease in shear stress with increasing chain stiffness at the same separations. This can be explained by

the fact that even though at the same separation the system with higher stiffness shows higher penetration between opposite chains, because of higher chain stiffness there is less interaction/contact between opposite chains, so the friction is decreasing instead of increasing.

6.5 Combination of grafting density and chain stiffness

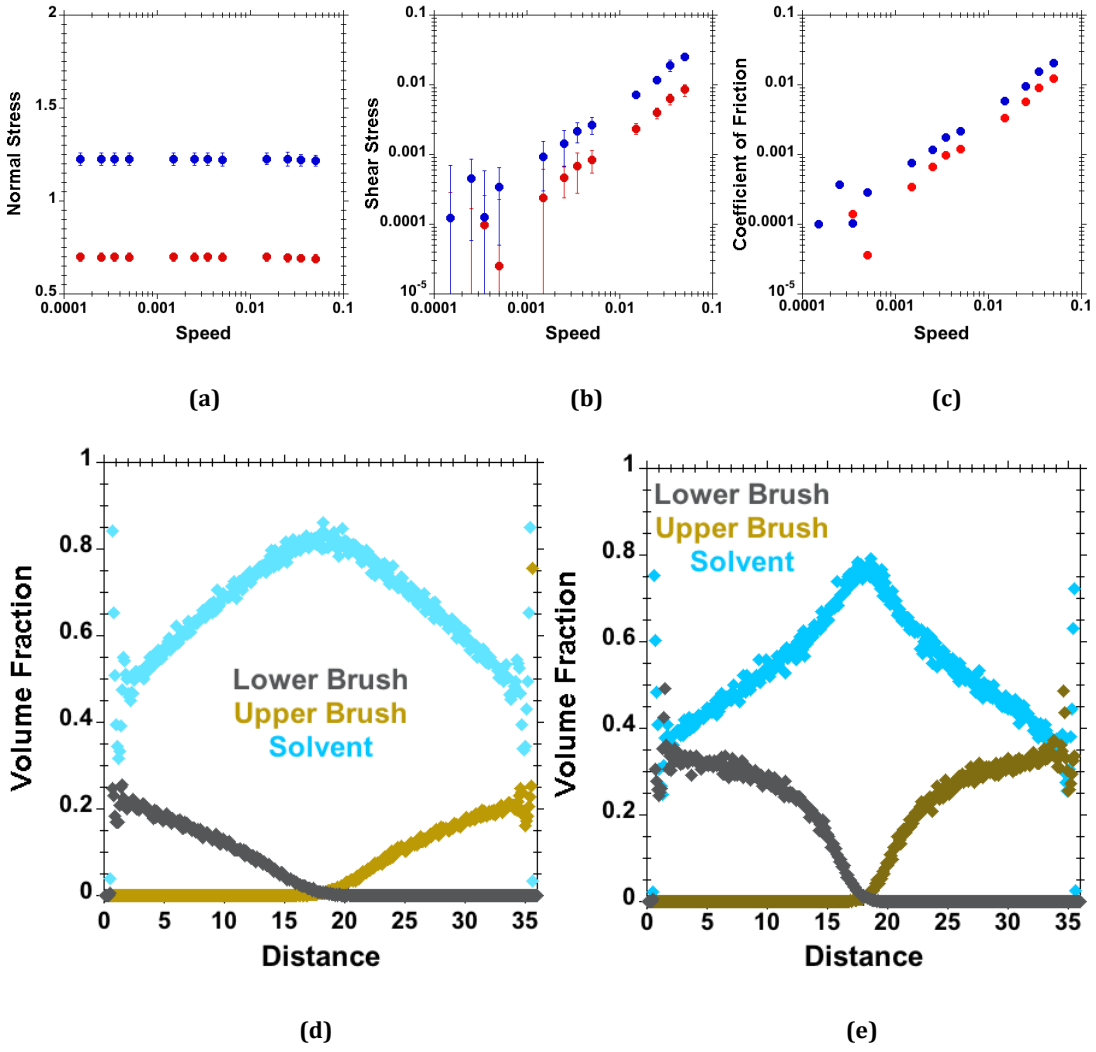

Figure 6.10 Effect of combination of chain stiffness and grafting density (red dots for ρ=0.075 and K_S=3 and blue dots for ρ=0.15 and K_S=0) resulting in equal equilibrium brush height, h=18 in each case, M=20, N=30 and good solvent quality (a) Normal stress against speed, (b) Shear stress against speed, density profiles of solvent (cyan dots), lower polymer-chains (grey dots) and upper polymer-chains (brown dots) for (c) ρ=0.075 and K=3, and (d) ρ=0.15 and K=0.

In Fig. 6.7 we have observed that different combinations of grafting density (ρ) and chain stiffness (K_S) can result in similar equilibrium brush height (h). For example, two different combinations, first ρ=0.075 and K_S=3 and second ρ=0.15 and K_S=0

result in the same equilibrium brush height, h =18. In Fig. 6.10, the normal and shear stresses are plotted against shear speeds for these two different cases discussed earlier at the same separation, D=36. We have observed higher normal and shear stresses at all shear speeds for the combination where grafting density is higher (though equilibrium brush height is same in both cases). The corresponding density profile plots confirm the similar equilibrium brush height.

6.6 Conclusions

Molecular-dynamics simulations were performed on a brush-against-brush system with explicit solvent beads. The effect of grafting density and chain stiffness was studied on the tribological behavior of polymer brushes. When the separation between polymer-bearing surfaces is maintained constant and the friction behavior of brushes studied over different shear speeds, the friction was found to be increasing with increasing grafting density. However, when the speed was kept constant, and the friction behavior was studied over different separations as a function of shear stress against normal stress, the coefficient of friction was found to be decreasing with increasing grafting density. This was explained with the help of the load-bearing capacity of polymer brushes with higher grafting density. Friction was found to be decreasing with increase in chain stiffness, both in speed-dependent and separation-dependent studies.

This study can be taken further to study the effect of other parameters such as chain length, solvent quality etc. to better understand the effect of different parameters on the tribological behavior of polymer brushes.

6.7 References

(1) Hess, S.; Kröger, M. Elastic and Plastic Behavior of Model Solids. *Technische Mechanik* **2002**.

(2) Kröger, M. *Models for Polymeric and Anisotropic Liquids*; Berlin Heidelberg, 2005; Vol. 675.

(3) Galuschko, A.; Spirin, L.; Kreer, T.; Johner, A.; Pastorino, C.; Wittmer, J.; Baschnagel, J. Frictional Forces Between Strongly Compressed, Nonentangled Polymer Brushes: Molecular Dynamics Simulations and Scaling Theory. *Langmuir* **2010**, *26* (9), 6418–6429.

(4) Galuschko, A. *Molecular Dynamics Simulations of Sheared Polymer Brushes*; 2010.

(5) Nalam, P. C.; Ramakrishna, S. N.; Espinosa-Marzal, R. M.; Spencer, N. D. Exploring Lubrication Regimes at the Nanoscale: Nanotribological Characterization of Silica and Polymer Brushes in Viscous Solvents. *Langmuir* **2013**, *29* (32), 10149–10158.

(6) Tsujii, Y.; Nomura, A.; Okayasu, K.; Gao, W.; Ohno, K.; Fukuda, T. AFM Studies on Microtribology of Concentrated Polymer Brushes in Solvents. *J Phys. Conf. Ser.* **2009**, *184* (1), 012031.

(7) Nomura, A.; Okayasu, K.; Ohno, K.; Fukuda, T.; Tsujii, Y. Lubrication Mechanism of Concentrated Polymer Brushes in Solvents: Effect of Solvent Quality and Thereby Swelling State. *Macromolecules* **2011**, *44* (12), 5013–5019.

(8) Nalam, P. C. *Polymer Brushes in Aqueous Solvent Mixtures: Impact of Polymer Conformation on Tribological Properties*; 2012.

(9) Press, W. H.; Flannery, B. P.; Teukolsky, S. A.; Vetterling, W. T. *Numerical Recipes in FORTRAN 77: Volume 1, Volume 1 of Fortran Numerical Recipes*; Cambridge University Press, 1992.

(10) Rosenberg, K. J.; Goren, T.; Crockett, R.; Spencer, N. D. Load-Induced Transitions in the Lubricity of Adsorbed Poly(L-Lysine)- G-Dextran as a Function of Polysaccharide Chain Density. *ACS Appl. Mater. Interfaces* **2011**, *3* (8), 3020–3025.

(11) Yamamoto, S.; Ejaz, M.; Tsujii, Y.; Fukuda, T. Surface Interaction Forces of Well-Defined, High-Density Polymer Brushes Studied by Atomic Force Microscopy. 2. Effect of Graft Density. *Macromolecules* **2000**, *33*, 5608–5612.

Chapter 7

Influence of Crosslinking on Tribological Behavior of Polymer Brushes

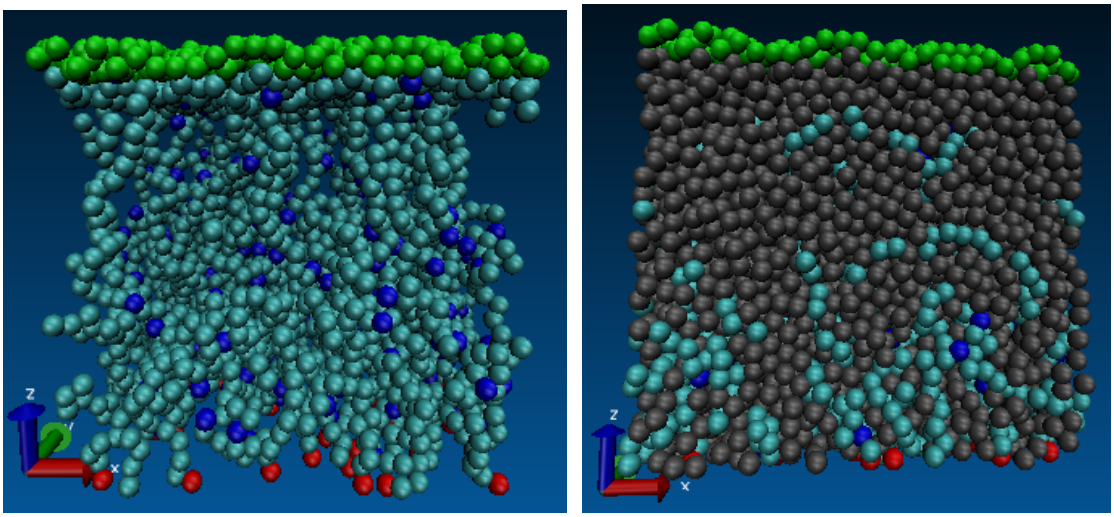

(a) (b)

Figure 7.1: Schematic of crosslinked polymer chains against wall system (a) Implicit Solvent and (b) Explicit Solvent. Red colored beads are tethered, cyan beads constitute the polymer chains, blue beads are crosslinkers, green beads make up the explicit wall and gray beads represent solvent.

Results from MD simulations of crosslinked polymer brushes are presented in this chapter. We have performed simulations that address either the (i) speed dependent (keeping the separation constant) or the (ii) separation dependent (keeping the speed constant) tribological behaviors of crosslinked polymer brushes. For case (i) implicit solvent-based MD simulations were performed while for case (ii) we have employed explicit-solvent-based MD simulations. All the simulations are carried for the brush against wall system **(Fig.7.1)**. The LJ-12/6 potential with R_{cw} = 2.5 (Eq 4.3) was used for interaction between polymer chains (also explicit solvent beads for explicit-solvent based simulations) and explicit-wall beads. The brush-against-wall system has M = 50 chains tethered randomly on the grafting surface at a grafting density of 0.075, and each chain consists of N = 50 beads. The counter explicit wall has beads

randomly placed at altitudes (D - 1) +/- 0.5 to allow for the effect of roughness, as described in **Chapter 4**. Simulations are performed for systems with different lengths of crosslinker chains (LS) and numbers of crosslinker chains (NS), as summarized in Table 7.1.

Table 7.1: Simulations carried out for M=50 chains of N=50 beads each, subject to the following lengths of crosslinker chains (LS) and amount of crosslinker chains (NS), where (100%) means that each monomer is connected to exactly one crosslinker chain.

LS	NS (Degree of Crosslinking in %)		
1	50 (4%)	100 (8%)	200 (16%)
2	50 (4%)	100 (8%)	200 (16%)
4	50 (4%)	100 (8%)	200 (16%)

7.1 Speed-dependent study with implicit solvent

The speed-dependent studies were carried out by maintaining the separation D between the grafting surface and the explicit wall constant, $D = 8$. The simulations were done for various fixed lateral speeds S = 0.0003, 0.0005, 0.0007, 0.001 and 0.003 of the tethered beads, while the opposing rough wall was kept in place. The simulations were carried out for a duration of 90,500,000 time steps (data for first 30,500,000 steps ignored in the analysis) at speed S = 0.0003 and for 9,500,000 steps (ignoring data for first 3,500,000 steps) for speed S = 0.003 where the time step was chosen as $\Delta t = 0.002$ when data was ignored and Δt=0.0025 when data was recorded and analyzed.

7.1.1 Effect of number of crosslinkers (NS)

Figure 7.2 shows results highlighting the effect of degree of crosslinking for crosslinkers of length LS=1 on the (a) normal stress, (b) shear stress, (c) coefficient of friction against speed, and (d) volume fraction against distance. The normal stress is found to be constant over the speeds studied for all the systems under consideration whereas it is found to be decreasing with increase in the degree of crosslinking. The shear stress is found to be increasing with increasing speed for all the systems and it also increases with increase in the degree of crosslinking. The coefficient of friction increases with increase in degree of crosslinking.

Figure 7.2(d) shows density profiles for polymer brush-systems with different degrees of crosslinking for the shortest (single bond) crosslinkers (LS = 1) in terms of volume fraction against distance. The decrease in normal stress with the increase in the degree of crosslinking can be explained with the help of a density-profile curve. The brush height decreases with increasing degree of crosslinking, so less deformation is felt in brushes with a higher degree of crosslinking at the same separation between wall and

the polymer-bearing surface. This results in a decrease of the normal stress applied at the same separation with increasing degree of crosslinking. The increase in shear stress with increase in degree of crosslinking can also be explained with the help of the density profile. As the degree of crosslinking increases there are fewer polymer chains available in the outer layer to assist brush-mediated lubrication[1-4] and also the lateral motion of polymer chains are more inter-dependent which results in an increase of the shear stress or coefficient of friction upon increasing the degree of crosslinking.

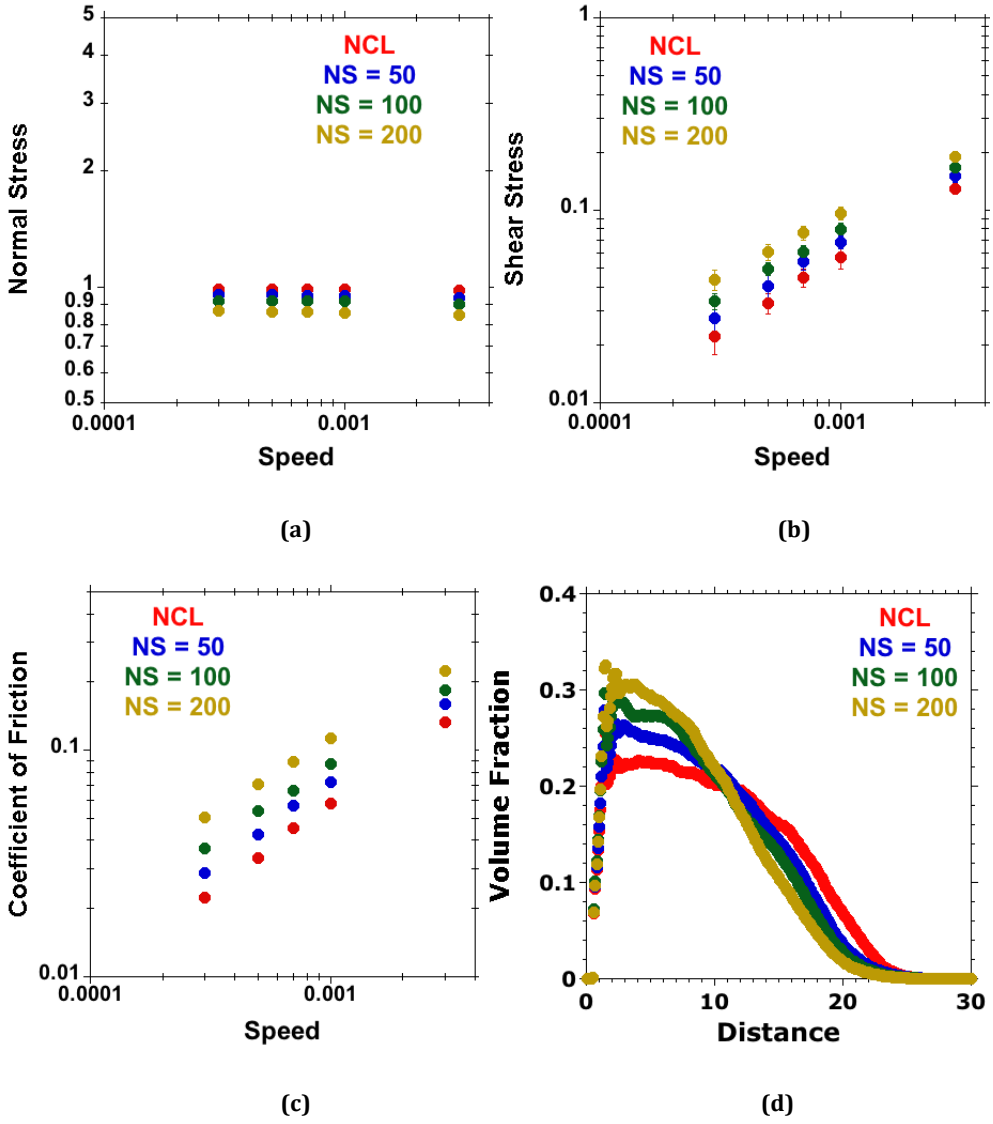

Figure 7.2: (a) Normal stress against shear speed (b) Shear stress against speed (c) Coefficient of friction against speed and (d) Volume fraction against distance for systems made of M = 50 chains with N = 50, at grafting density ρ=0.075, length of crosslinkers/spacers LS=1, and for different numbers of spacers/crosslinkers (NS) = 0, 50, 100 and 200.

Figure 7.3 presents the results to the study of the effect of degree of crosslinking on polymer-brush systems having crosslinkers of length, LS=4 in terms of (a) normal stress against speed, (b) shear stress against speed, (c) coefficient of friction against speed and (d) volume fraction against distance.

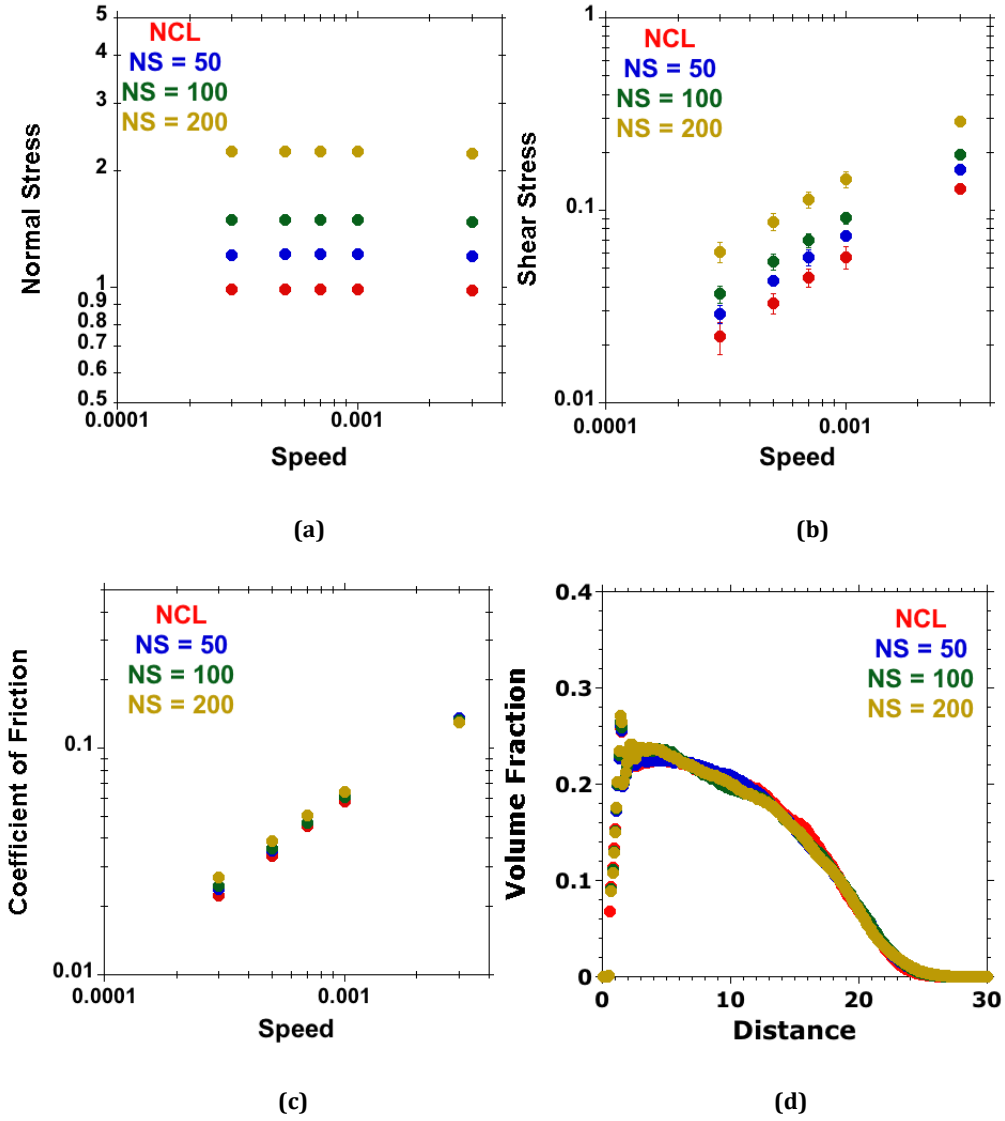

Figure 7.3: For M = 50, N = 50, ρ = 0.075, LS = 4 and for different number of spacers/crosslinkers (NS) = 0, 50, 100 and 200 (a) Normal stress against speed (b) Shear stress against speed (c) Coefficient of friction against speed and (d) Volume fraction against distance.

The normal stress is found to remain constant over the speeds studied for each system, whereas it increases with increase in degree of crosslinking at each speed. The shear stress is found to be increasing with speed for each of the systems studied and it also increases with increasing degree of crosslinking at each speed. The coefficient of

friction is found to be increasing with increase in speed for each system and it also increases with increase in degree of crosslinking at each speed. However, the effect of the degree of crosslinking on the coefficient of friction for polymer-brush systems with LS=4 is not as significant as was observed with shorter crosslinkers, LS=1.

The observations can be rationalized with the help of the density profiles for the different systems. The density-profile curves and brush heights for systems with different degrees of crosslinking at L=4 are quite similar to the corresponding uncrosslinked polymer brush systems. The increase in normal and shear stress with increase in the degree of crosslinking can be explained with an increase of the number density (because of the explicit beads contained in crosslinker chains) with increase in the degree of crosslinking. The coefficient of friction (ratio of shear stress and normal stress) exhibits a slight increase with increase in degree of crosslinking at each speed, which is a reflection of the density-profile curves for different degrees of crosslinking at LS=4 in comparison to uncrosslinked polymer-brush systems. The slight increase in the coefficient of friction with increase in degree of crosslinking can be attributed to interdependent lateral motion of the crosslinked systems and increases with an increase in the degree of crosslinking. Uncrosslinked polymer chains are deformed easily in comparison to gels under shear[5-7].

7.1.2 Effect of length of crosslinkers (LS)

Figure 7.4 present the results for the crosslinked polymer brush systems with NS = 50 crosslinkers/spacers, to facilitate the study of the effect of length of crosslinkers (LS) in terms of (a) normal stress against speed, (b) shear stress against speed, (c) coefficient of friction against speed, and (d) volume fraction against distance. The normal stress is found to remain constant for each of the systems over the speeds studied. In comparison to the uncrosslinked systems, the normal stresses at each speed

decrease for LS=1 but increase for LS=2 and LS=4 with increasing length of crosslinkers. The shear stress for all the crosslinked systems is found to be higher compared with the uncrosslinked systems, but no clear effect of the length of crosslinkers is observed for any of the systems. The shear stress was found to be increasing with an increase in speed for all the NS=50 systems. The coefficient of friction is found to be increasing with increase in speed for each speed whereas the coefficient of friction slightly decreases at all speeds studied with an increase of the length of crosslinkers, again for NS=50 system.

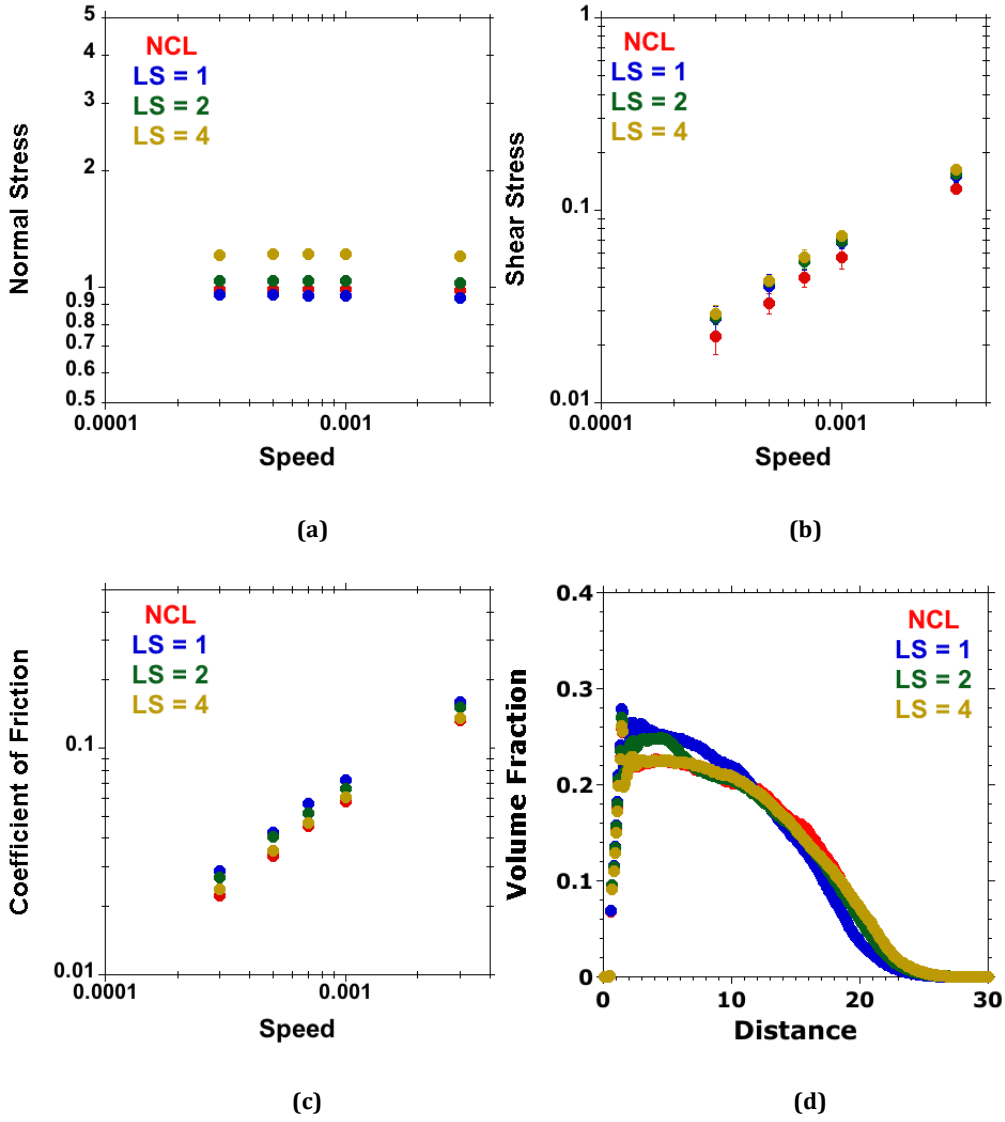

Figure 7.4: For M = 50, N = 50, ρ = 0.075, NS = 50 and for different lengths of spacers/crosslinkers (LS) = 0, 1, 2 and 4 (a) Normal stress against speed (b) Shear stress against speed (c) Coefficient of friction against speed and (d) Volume fraction against distance

Less normal stress for system with LS=1 crosslinkers in comparison to uncrosslinked polymers can be explained by a decrease in brush height with increase in degree of crosslinking for LS = 1 crosslinkers. Deformation of crosslinked brushes with LS = 1 in comparison to uncrosslinked polymer brushes at the same separation is less, which results in less normal stress applied on the crosslinked brush (LS = 1) in comparison to uncrosslinked polymer brushes at the same separation. As the length of crosslinkers increases (LS = 2 and LS = 4), the number density of beads in the simulation box increases, so the normal stress also increases in comparison to that in the uncrosslinked polymer brushes. The shear stress for crosslinked polymer brushes increases with respect to uncrosslinked polymer brushes because of an interdependent motion of crosslinked chains under shear. The coefficient of friction against speed curve reflects the density-profile curves. For systems with longer crosslinkers, the density profile of crosslinked and uncrosslinked brushes looks similar, which is reflected in a decrease in the coefficient of friction with increasing length of crosslinkers.

Figure 7.5 shows results for uncrosslinked and crosslinked polymer brushes with NS = 200 to facilitate the study of the effect of lengths of crosslinkers in terms of (a) normal stress against speed, (b) shear stress against speed, (c) coefficient of friction against speed, and (d) volume fraction against distance to the grafting surface. The normal stress here also decreases for LS = 1 in comparison to uncrosslinked polymer brushes but increases for LS = 2 and LS = 4, and it can also be explained as before for the case of NS = 50 crosslinkers. The shear stress increases with increase in the length of crosslinkers (LS) at all speeds studied. The coefficient of friction decreases with increase in length of crosslinkers at all speeds studied and at LS = 4 the coefficients of friction values are at all speeds close to those for the uncrosslinked polymer brush

systems. The density profiles (figure 7.5(d)) show that the brush height increases with increase in length of crosslinkers, and the density profile for LS = 4 is quite similar to that of the uncrosslinked polymer brush system. As the length of crosslinkers increases, the crosslinked polymer brushes behave more and more like uncrosslinked polymer brushes and assist in brush-mediated lubrication[1,4,8]. For systems with shorter crosslinkers as can be seen from density profile lesser polymers are available at the free end of grafted polymers to facilitate brush assisted lubrication and it results in higher friction observed. Compared to system with NS = 50 crosslinkers, the effect of length of crosslinkers is more clearly visible in systems with NS = 200 crosslinkers.

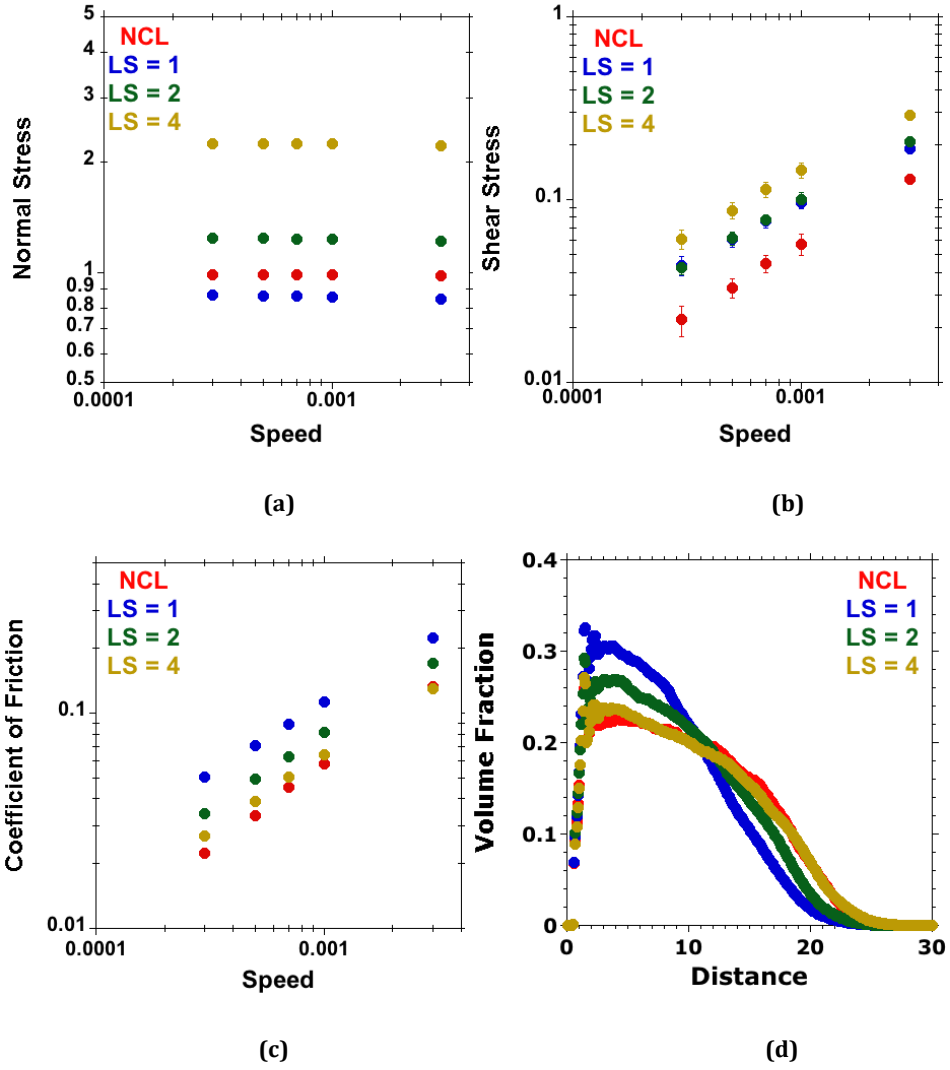

Figure 7.5: For M = 50, N = 50, ρ = 0.075, NS = 200 and for different length of spacers/crosslinkers (LS) = 0, 1, 2 and 4 (a) Normal stress against speed (b) Shear stress against speed (c) Coefficient of friction against speed and (d) Volume fraction against distance to the grafting surface.

7.2 Separation-dependent study at constant speed with explicit solvent

The separation-dependent studies were carried out at a fixed shear speed, S = 0.001 applied on the tethered beads at different separations between explicit wall and polymer-bearing surface. At each separation, normal and shear stress acting on the brush and crosslinkers were calculated and the shear stress plotted against normal stress for different combinations of lengths and numbers of crosslinkers, in order to study the effect of crosslinking on the frictional behavior of model polymer brushes. The simulations were done for 30,500,000 steps where data for the first 10,500,000 steps at timestep Δt = 0.002 were ignored and data for subsequent 20,000,000 steps at Δt = 0.0025 were recorded and analyzed.

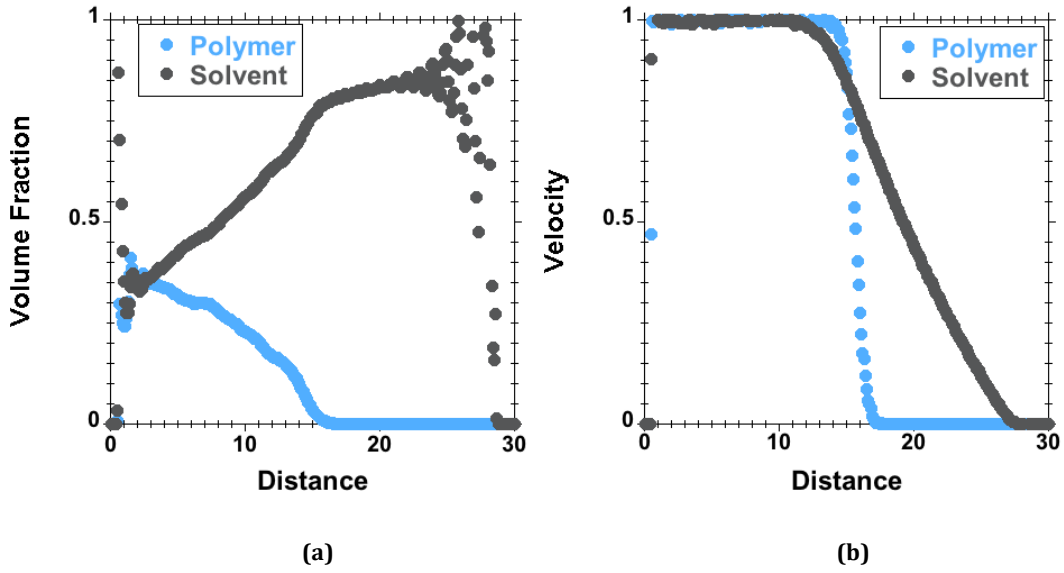

Figure 7.6: For M = 50, N = 50, ρ = 0.075, LS = 1 and NS = 200 in explicit solvent with shear speed = 1 applied on the tethered beads, (a) Density profile, and (b) Velocity Profile.

Figure 7.6(a) shows a typical density profile for crosslinked polymer-brush systems under shear with explicit solvent beads and Fig. 7.5(b) shows the corresponding velocity profile of the polymer and explicit solvent beads under shear when a shear speed, $S = 1$, is applied on the tethered beads in a brush-against-wall system. Tethered beads are located at altitude $D = 0.5$ and the explicit wall is at $D = 30$. It is important

to mention here that a very high shear speed of S=1 is applied in this case to get a clear velocity profile and density profile but in general all the subsequent simulations in this chapter are carried at a lower speed, $S = 0.001$. From the density profile we can see that there are no polymer beads beyond $D = 16$ and at each separation there are more solvent beads than polymer beads. In the velocity profile, we see a perfect step-like function for the velocity of the polymers and the velocity profile for solvent particles shows that the polymer drags the solvent beads with the imposed speed S = 1 up to $D = 13$; subsequently the profile decreases linearly to 0 at wall position $D = 30$. The crosslinking decreases the relative permeability of the brush and thus moves more of strain rate to narrower region near wall.

7.2.1 Effect of number of crosslinkers (NS)

Figure 7.7 shows the results on the effect of degree of crosslinking on friction behavior of polymer brushes in terms of shear stress against normal stress and volume fraction against distance, for different systems having crosslinkers of length LS = 1, LS = 2 and LS = 4. The shear stress for all the crosslinked systems is found to be higher compared with that of the uncrosslinked system at a given normal stress. The shear stress was found to be increasing with increasing degree of crosslinking, but the effect is more pronounced in the systems having shorter crosslinkers of length LS = 1. These observations can be explained as follows. Crosslinking leads to interdependent motion of crosslinked grafted chains under shear, resulting in an increase in the shear stress for all the crosslinked systems when compared to uncrosslinked polymer brush systems. Under shear, the uncrosslinked systems are deformed more easily than a crosslinked network of polymer brushes.[5] The increase in the degree of crosslinking leads to more chains moving interdependently under shear. We therefore find an increase in friction with increase in degree of crosslinking.

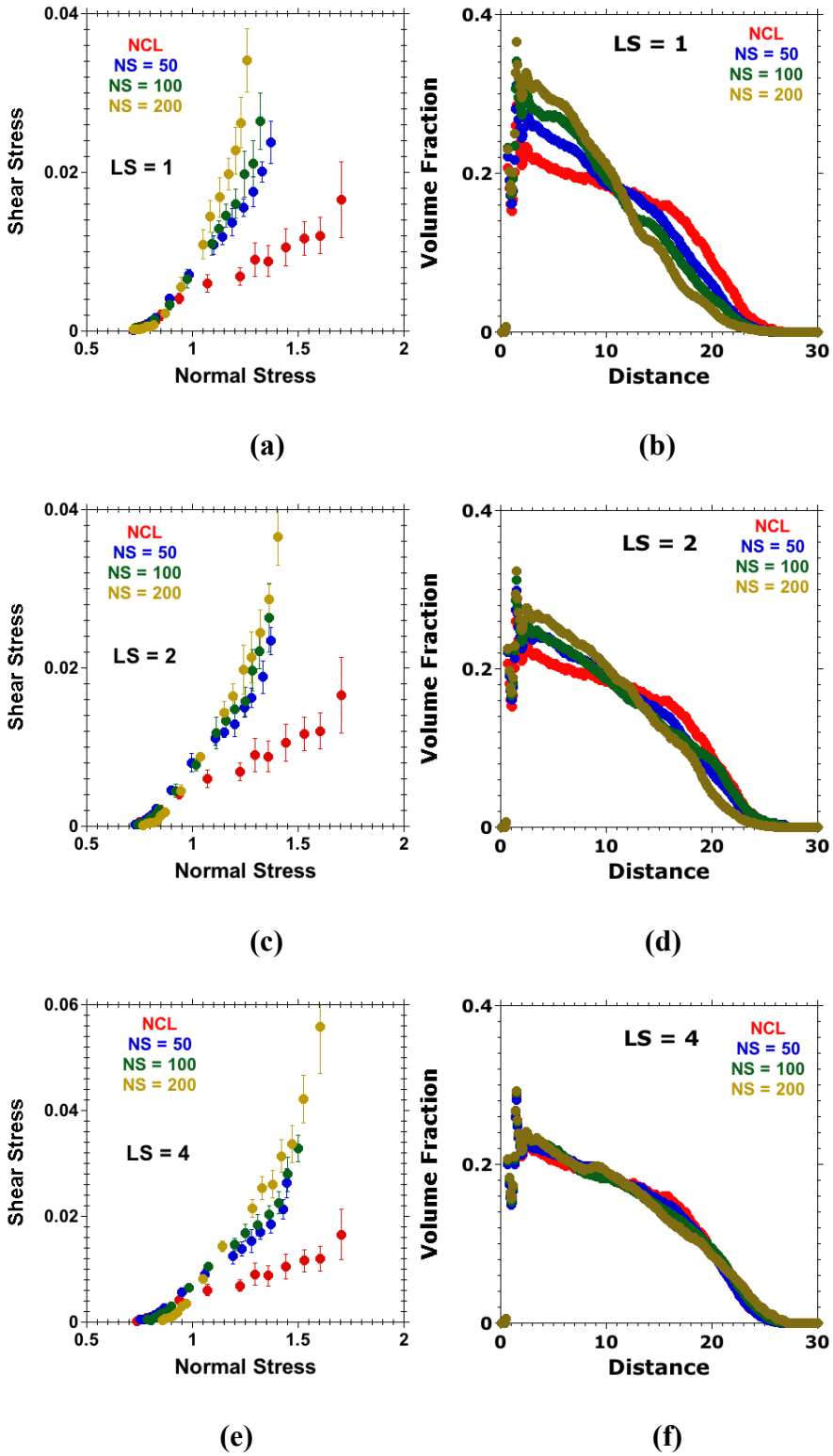

Figure 7.7: For M = 50, N = 50 and ρ = 0.075 in explicit solvent, for LS = 1 (a) Shear stress against normal stress, (b) Density profile, for LS = 2 (c) Shear stress against normal stress, (d) Density profile and for LS = 4 (e) Shear stress against normal stress, (f) Density profile each for different number of spacers/crosslinkers (NS) = 0, 50, 100 and 200.

Inspecting the density profiles, the systems with shorter crosslinkers show a decrease in brush height with increase in degree of crosslinking and more and more polymer density is accumulated at the grafting surface. There is hence fewer polymers available towards the outer layer of grafted chains to assist in brush-mediated lubrication[1,9]. This leads to a further increase in friction/shear.

7.2.2 Effect of length of crosslinkers (LS)

Figure 7.8 presents plots of the shear stress against normal stress and volume fraction against distance for different systems, to facilitate the study of the effect of length of crosslinkers on the tribological behavior of crosslinked polymer brushes. As before, we see that shear stress for all the crosslinked systems is higher when compared with that of the uncrosslinked systems. We observe a decrease in shear stress with increase in the length of crosslinkers in systems having number of spacers, NS = 50, 100 and 200 but the effect is very substantial only in the system with NS = 200 spacers. The density profile shows that the brush height of each of the crosslinked systems increases with increase in length of crosslinkers and the density profile for the LS = 4 crosslinked system resembles the profile of an uncrosslinked system. The systems with lower brush height have less polymer beads towards the free end of grafted chains and more polymers near the grafting surface, so that fewer polymers are available for brush-assisted lubrication, in addition to the effect of interdependent motion of crosslinked chains. This results in higher shear or friction for systems with smaller lengths of crosslinkers. For systems with larger lengths of crosslinkers (LS=4) the increase in friction due to crosslinking is caused only by the interdependent motion of crosslinked chains under shear. Under shear, uncrosslinked polymer networks are deformed more easily than the crosslinked chains[5,6].

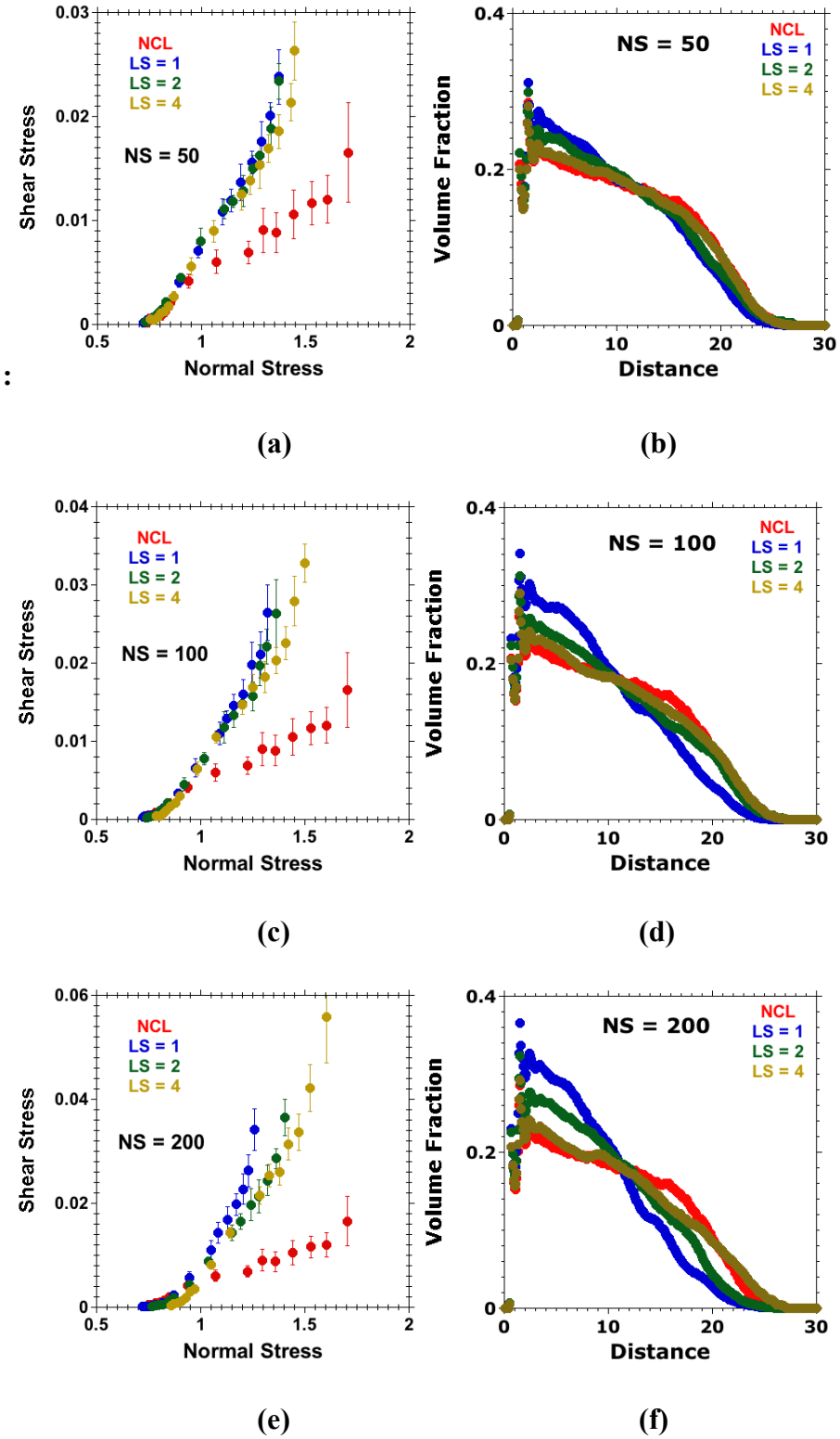

Figure 7.8: For M = 50, N = 50 and ρ = 0.075 in explicit solvent, for NS = 50 (a) Shear stress against normal stress, (b) Density profile, for NS = 100 (c) Shear stress against normal stress, (d) Density profile and for NS = 200 (e) Shear stress against Normal Stress, (f) Density profiles for different lengths of spacers/crosslinkers (LS) = 0, 1, 2 and 4.

7.3 Comparison with Experimental Results

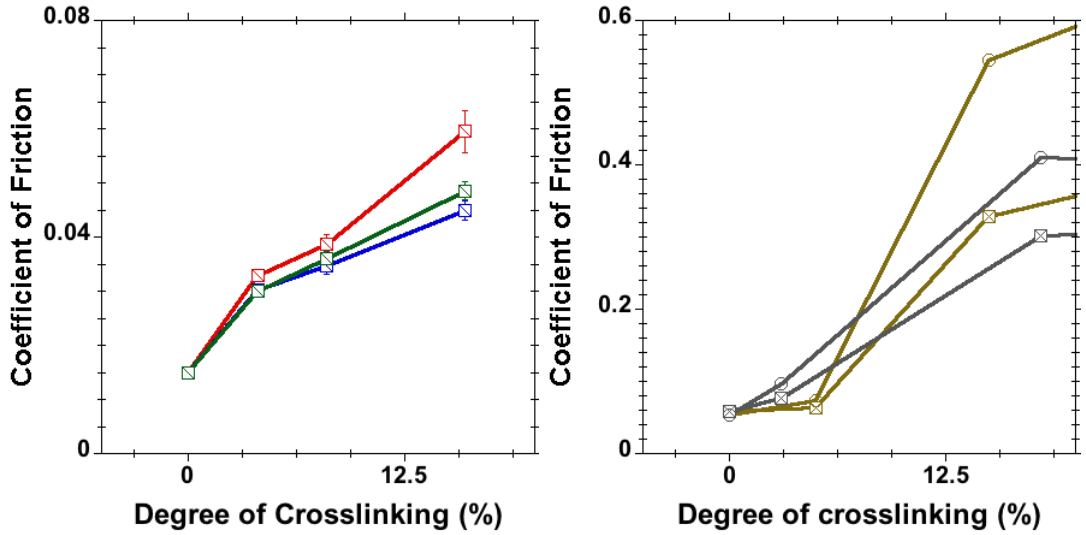

(a) (b)

Figure 7.9: Coefficient of friction against degree of crosslinking for (a) Simulation with M=50 and N=50 for different lengths of crosslinkers, LS=1 (red lines), LS=2 (blue lines) and LS=4 (green lines) at a shear speed, S=0.001 for a brush-against-wall system and (b) Experimental results for length of crosslinkers, LS = C_2 (brown lines) and LS = C_4 (gray lines) at speed of 1μm/sec (square) and 5 μm/sec (circle).

Figure 7.9(a) shows the coefficient of friction against the degree of crosslinking for different lengths of crosslinkers, as obtained from our simulation. For each system the coefficient of friction has been estimated from the slope of shear stress against normal stress curves from the initiation of deformation until a 50% deformation of polymer brushes. The shear stress against normal stress curve in this regime is predominantly linear and a linear curve was fitted taking into account the error at each point in the curve[10]. The coefficient of friction for all the crosslinked system is found to be higher than that of the uncrosslinked system and it is also found to be increasing with the degree of crosslinking for systems having different lengths of crosslinkers. Similar observations were made in the experimental results of Li et. al.[4] where the coefficient of friction was found to be increasing with increase in crosslinker content in PAAm hydrogel-brushes. Concerning the effect of crosslinker length on the coefficient of friction at given degree of crosslinking, the coefficients of friction for LS = 2 and LS

= 4 are below the values for the LS = 1 systems at all degrees of crosslinking, but the effect is more clear only at a higher degree of crosslinking. The effect of the length of crosslinkers between LS = 2 and LS = 4 remains unresolved. The systems with LS = 4 crosslinkers show higher coefficients of friction than systems with LS = 2 at 16% degree of crosslinking. Next we compare the simulation results with experimental results for PGMA gels presented in **Chapter 3**. The experimental results are reproduced in Fig. 7.8(b) up to 20% degree of crosslinking only. The effect of degree of crosslinking on the coefficient of friction from our simulations is consistent with the experimental results. But the effect of length of crosslinkers on the coefficient of friction in experiments switches at different degrees of crosslinking. At a lower degrees of crosslinking (less than 5%), the coefficient of friction increases with increase in the length of crosslinkers and at a higher degree of crosslinking (more than 15%) decreases with increase in length of crosslinker. In our simulations we observe a decrease in the coefficient of friction with increasing length of crosslinkers when compared with results of the LS = 1 systems. At 16% degree of crosslinking, however, the coefficient of friction for LS = 4 system is higher than for the LS = 2 system. The effect of length of crosslinkers on frictional behavior of gels is generally not pronounced, and requires further investigation.

7.4 Conclusions

Crosslinked polymer brushes are successfully modeled using the coarse-grained MD technique. The tribological behavior of crosslinked polymer brushes under shear has been compared with uncrosslinked polymer brushes and also with experimental results in **Chapter 3** of the thesis. The simulations were done (i) at fixed separation subject to different shear speeds applied on the tethered beads, using an implicit solvent, and (ii) at a constant speed at different separations using an explicit solvent.

In general the coefficient of friction for all the crosslinked systems was found to be larger than for the uncrosslinked polymer brushes. We observed an increase in the coefficient of friction with increasing degree of crosslinking and a decrease of the coefficient of friction with increasing crosslinker lengths for all speed dependent studies. For the separation-dependent studies, results were presented in the form of shear stress against normal stress. Here, too, there was a clear trend towards an increase of the coefficient of friction with increasing crosslinking degree and the trends were consistent with the experimental observations (**Chapter 3**) for PGMA brushes and gels in DMF. The length of crosslinkers did not show any clear influence on the tribological response of the gels under shear in our separation dependent studies.

This work can be taken forward by doing studies over a wider range of degree of crosslinking for various lengths of crosslinkers to gain a better understanding of the influence of the length of crosslinkers on the mechanical behavior of gels under shear.

7.5 References

(1) Lee, S.; Spencer, N. D. Sweet, Hairy, Soft, and Slippery. *Science* **2008**, *319* (5863), 575–576.

(2) Chen, M.; Briscoe, W. H.; Armes, S. P.; Klein, J. Lubrication at Physiological Pressures by Polyzwitterionic Brushes. *Science* **2009**, *323* (5922), 1698–1701.

(3) Li, A. *Structure-Property Relationships of Surface-Grafted Polymeric Architectures: From Ultra-Thin Films to Quasi-3D Polymer Assemblies*; 2013.

(4) Li, A.; Benetti, E. M.; Tranchida, D.; Clasohm, J. N.; Schönherr, H.; Spencer, N. D. Surface-Grafted, Covalently Cross-Linked Hydrogel Brushes with Tunable Interfacial and Bulk Properties. *Macromolecules* **2011**, *44* (13), 5344–5351.

(5) Gong, J. P. Friction and Lubrication of Hydrogels?Its Richness and Complexity. *Soft Matter* **2006**, *2*, 544.

(6) Gong, J. P.; Higa, M.; Iwasaki, Y.; Katsuyama, Y.; Osada, Y. Friction of Gels. *Journal of Physical Chemistry B* **1997**, *101* (28), 5487–5489.

(7) Ohsedo, Y.; Takashina, R.; Gong, J. P.; Osada, Y. Surface Friction of Hydrogels with Well-Defined Polyelectrolyte Brushes. *Langmuir* **2004**, *20* (16), 6549–6555.

(8) Klein, J.; Perahia, D.; Warburg, S. Forces Between Polymer-Bearing Surfaces Undergoing Shear. *Nature* **1991**.

(9) Klein, J.; Kumacheva, E.; Mahaiu, D.; Perahia, D.; Fetters, L. J. Reduction of Frictional Forces Between Solid Surfaces Bearing Polymer Brushes. *Nature* **1994**, *370* (6491), 634–636.

(10) Press, W. H.; Flannery, B. P.; Teukolsky, S. A.; Vetterling, W. T. *Numerical Recipes in FORTRAN 77: Volume 1, Volume 1 of Fortran Numerical Recipes*; Cambridge University Press, 1992.

Chapter 8

Summary and Outlook

8.1 Summary

The presented thesis is an attempt to study the tribological behavior of polymer brushes using a complementary approach that combined computer simulations and experiments. A major aim was to formulate a design rules for the fabrication of polymer brushes with specific tribological properties.

Experimental studies were performed using colloidal-probe lateral force microscopy (LFM) on poly (lauryl methacrylate) (PLMA) brushes in hexadecane solvent and poly (glycidyl methacrylate) (PGMA) brushes and gels in dimethylformamide (DMF) solvent. Simulation studies were performed using a multibead-spring based coarse-grained molecular dynamics technique.

In Chapter 3, experimental results on polymer brushes have been presented and discussed. PLMA brushes in hexadecane and PGMA bushes in DMF solvents show low friction when compared to a bare silica surface. The experiments were performed by attaching silica and polyethylene (only for PLMA brushes) microspheres on tipless atomic force microscope (AFM) cantilevers. The effects of length of crosslinkers and degree of crosslinking were studied on the frictional behavior of PGMA gels in DMF solvents. It was observed that the coefficient of friction increases with increasing degree of crosslinking for all lengths of crosslinkers investigated. With increasing length of crosslinker chains, the coefficient of friction was found to be increasing at lower degrees of crosslinking, whereas at higher crosslinking degrees friction was found to be decreasing.

Chapter 5 presented results obtained during modeling of dextran brushes using an implicit-solvent approach. Simulation parameters (grafting density and number of beads per chain) were estimated by matching the radius of gyration and extended chain length with experimental data. Using the obtained simulation parameters, equilibrium MD simulations were performed, where polymer-bearing surfaces were brought closer step by step, and at each step the normal stress was calculated and simulation results were compared with force against distance results from surface force apparatus (SFA) experiments[1] for dextran brushes in HEPES. Next, a shear speed was applied on the tethered beads of an equilibrated brush against wall system. Results for the shear stress against speed were compared with experimental[2] results from colloidal-probe lateral force microscopy (LFM) on dextran brushes in HEPES. The boundary-like regime observed in the experiments was interpreted with the help of simulation findings.

In Chapter 6, explicit-solvent-based simulation results for brush-against-brush systems subjected to shear have been presented and discussed. Simulations were performed to study the effect of speed (at fixed separation) and the effect of separation (at fixed speed) on the tribological behavior of polymer brushes. As in the previous experimental[3,4] work, the "boundary-like" regime was observed in the simulation studies at very low speeds for the brush-brush system. The effect of grafting density on tribological behavior of polymer brushes was studied and compared with previous simulations[5] and experimental[6] results. We further observed that an increase in chain stiffness leads to a reduction in friction in polymer-brush based lubrication.

MD simulations of crosslinked polymer brushes have been discussed in Chapter 7. Simulations were performed for the speed-dependent (using an implicit solvent

approach, at fixed separation) and separation-dependent (using an explicit solvent approach, at constant speed) effect of crosslinking on the tribological response of polymer brushes. The trends from simulations were compared with, and discussed in the light of, experimental results in **Chapter 3** and previously published results[7,8]. It was observed that the coefficient of friction increases with increasing degree of crosslinking in both speed-dependent and separation-dependent studies. In the speed-dependent studies, friction was observed to be decreasing with increasing length (LS) of crosslinker chains. In the separation-dependent studies, the coefficient of friction decreased for systems with LS=2 and LS=4 crosslinkers in comparison with systems made of LS=1 crosslinkers, while it increased for systems with LS=4 in comparison with systems containing LS=2 crosslinkers.

In conclusion, the investigations carried out on polymer brushes in this thesis seem to have provided useful insights into the understanding of the mechanical and structural behavior of polymer brushes under shear, and they may have the potential to make significant contributions to future studies in the area. While the coarse-grained simulations were capable of reproducing particular experimental results, they quickly provide additional microscopic information that is nowadays not directly accessible, neither by experiments nor by full atomistic simulations.

8.2 Outlook

8.2.1 Effect of chain length

There have been several experimental studies[9-11] on the effect of chain length or brush thickness on the friction behavior of polymer brushes. McNamee et al.[10] measured higher friction for poly (ethylene glycol) (PEG) polymer brush systems with longer chains and they attributed this to higher degree of entanglements in longer brushes.

Zhang et al.[9] observed for poly(2-methacryloyloxy)ethylphosphorylcholine) (PMPC) brushes with a thickness greater than 200 nm, that the coefficient of friction decreases with increasing brush thickness. For shorter PMPC brushes, little variation was observed in the coefficient of friction upon varying brush thickness. They explained their observations by an increase in the amount of bound solvent with the increase in brush thickness, which leads to an increase in osmotic pressure, causing less deformation at any given applied load.

It would be interesting to take forward the current simulation work to investigate and explain the effect of chain-length on the tribological behavior of polymer brushes.

8.2.2 Solvent-quality effect

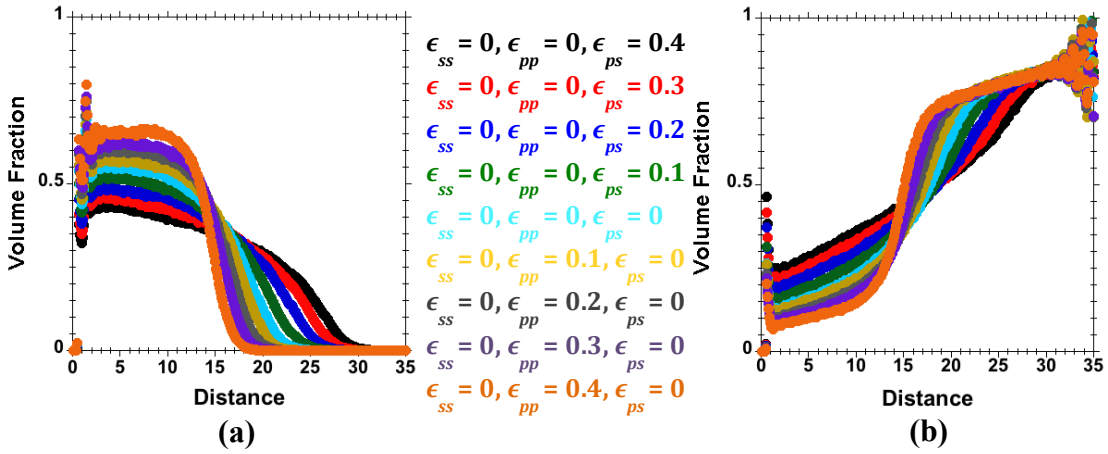

Figure 8.1: Volume fraction against distance curves for different solvent quality for (a) Polymer and (b) Solvent. Simulation was performed for brush against wall system with number of grafted chains, M=36 with each chain having N=60 beads and grafting density, ρ = 0.185.

Figure 8.1 shows the density profiles for polymer (Fig. 8.1(a)) and solvents (Fig.8.1 (b)) for various combinations ϵ_{pp}, ϵ_{ss} and ϵ_{ps} values in the LJ-cosine potential[12,13] (equations 4.4 and 4.5 in chapter 4) resulting in different solvent qualities. The simulations were performed for simulation parameters (number of chains, length of chains and grafting density) as by Dimitrov et al.[12] They used a dissipative particle dynamics (DPD) thermostat, whereas a temperature rescaling thermostat was used for

our results presented in Fig. 8.1. This approach can be taken forward to study the effect of solvent quality on the behavior of polymer brushes subjected to shear.

8.2.3 Wear studies

Wear behavior can be explored within the current model by anchoring chain ends using a modified form of the FENE force law, known as FENE-C model[14,15], which is parameterized by an energy barrier to be overcome (or energy to be gained) during an individual scission (or tethering) event. See Milchev et al.[16] work for a recent simulation study on breakable bonds in a bottle-brush polymer and other works[17,18] for simplified models.

A simple breakable quartic[19,20] potential can be employed to study the wear behavior of polymer brushes. This potential gives the same equilibrium bond length as FENE bond.

$$E = K_q(r - R_c)^2\left(r - R_{qc} - B_1\right)(r - R_{qc} - B_2) \qquad 8.1$$

The coefficient K_q has units of energy/distance^4, B_1, B_2 and R_{qc} have units of distances and U_0 has units of energy. The coefficients should be selected carefully to form a suitable bond potential.

Figure 8.2(a) shows the comparison between the FENE and the quartic potential at different values of the coefficients for the FENE and quartic bond. Figure 8.2(b) shows the number of bonds against time using the quartic potential. Breaking of bonds is observed at higher speeds over different time steps.

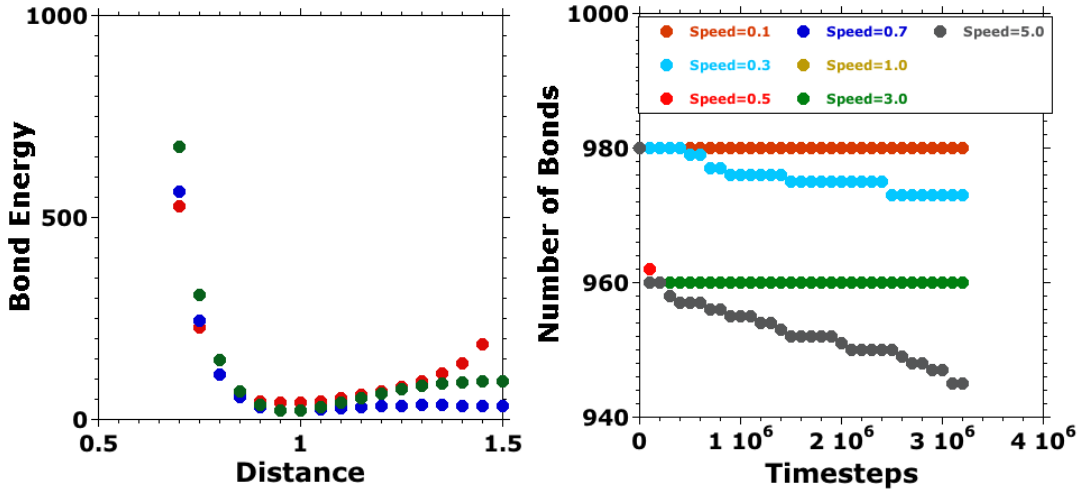

(a) (b)

Figure 8.2: (a) Bond energy against distance plots, to compare FENE potential (K = 30, and R_0 = 1.5), Quartic potential (with K_q = 2351, B_1 = 0, B_2 = 0.7425, R_{qc} = 1.5 and U_0 = 92.94467) and Quartic potential (with K_q = 1200, B_1 = -0.55, B_2 = 0.25, R_{qc} = 1.5 and U_0 = 34.6878) and (b) Number of bonds against time steps at different speeds for a brush-against-wall system having no. of chains, M = 20 with each chains having N = 50 beads, grafting density, ρ = 0.075 and good solvent quality. At the beginning of the simulation the number of bonds was 980.

The model discussed in the thesis can be taken forward to study the wear behavior of polymer brushes as a function of grafting density, chain stiffness, length of chains and degree of crosslinking.

8.3 References

(1) Espinosa-Marzal, R. M.; Nalam, P. C.; Bolisetty, S.; Spencer, N. D. Impact of Solvation on Equilibrium Conformation of Polymer Brushes in Solvent Mixtures. *Soft Matter* **2013**, *9* (15), 4045.

(2) Nalam, P. C.; Ramakrishna, S. N.; Espinosa-Marzal, R. M.; Spencer, N. D. Exploring Lubrication Regimes at the Nanoscale: Nanotribological Characterization of Silica and Polymer Brushes in Viscous Solvents. *Langmuir* **2013**, *29* (32), 10149–10158.

(3) Tsujii, Y.; Nomura, A.; Okayasu, K.; Gao, W.; Ohno, K.; Fukuda, T. AFM Studies on Microtribology of Concentrated Polymer Brushes in Solvents. *J Phys. Conf. Ser.* **2009**, *184* (1), 012031.

(4) Nomura, A.; Okayasu, K.; Ohno, K.; Fukuda, T.; Tsujii, Y. Lubrication Mechanism of Concentrated Polymer Brushes in Solvents: Effect of Solvent Quality and Thereby Swelling State. *Macromolecules* **2011**, *44* (12), 5013–5019.

(5) Galuschko, A.; Spirin, L.; Kreer, T.; Johner, A.; Pastorino, C.; Wittmer, J.; Baschnagel, J. Frictional Forces Between Strongly Compressed, Nonentangled Polymer Brushes: Molecular Dynamics Simulations and Scaling Theory. *Langmuir* **2010**, *26* (9), 6418–6429.

(6) Rosenberg, K. J.; Goren, T.; Crockett, R.; Spencer, N. D. Load-Induced Transitions in the Lubricity of Adsorbed Poly(L-Lysine)- G-Dextran as a Function of Polysaccharide Chain Density. *ACS Appl. Mater. Interfaces* **2011**, *3* (8), 3020–3025.

(7) Gong, J. P.; Higa, M.; Iwasaki, Y.; Katsuyama, Y.; Osada, Y. Friction of Gels. *Journal of Physical Chemistry B* **1997**, *101* (28), 5487–5489.

(8) Gong, J. P. Friction and Lubrication of Hydrogels?Its Richness and Complexity. *Soft Matter* **2006**, *2*, 544.

(9) Zhang, Z.; Morse, A. J.; Armes, S. P.; Lewis, A. L.; Geoghegan, M.; Leggett, G. J. Effect of Brush Thickness and Solvent Composition on the Friction Force Response of Poly(2-(Methacryloyloxy)Ethylphosphorylcholine) Brushes. *Langmuir* **2011**, *27* (6), 2514–2521.

(10) McNamee, C. E.; Yamamoto, S.; Higashitani, K. Preparation and Characterization of Pure and Mixed Monolayers of Poly(Ethylene Glycol) Brushes Chemically Adsorbed to Silica Surfaces. *Langmuir* **2007**, *23* (8), 4389–4399.

(11) Kitano, K.; Inoue, Y.; Matsuno, R.; Takai, M.; Ishihara, K. Nanoscale Evaluation of Lubricity on Well-Defined Polymer Brush Surfaces Using QCM-D and AFM. *Colloid Surface B* **2008**, *74* (1), 350–357.

(12) Dimitrov, D. I.; Milchev, A.; Binder, K. Polymer Brushes in Solvents of Variable Quality: Molecular Dynamics Simulations Using Explicit Solvent. *J. Chem. Phys.* **2007**, *127* (8), 084905.

(13) Soddemann, T. Non–Equilibrium Molecular Dynamics Study of an Amphiphilic Model System. **2001**.

(14) Kröger, M. *Models for Polymeric and Anisotropic Liquids*; Berlin Heidelberg, 2005; Vol. 675.

(15) Kröger, M.; Makhloufi, R. Wormlike Micelles Under Shear Flow: a Microscopic Model Studied by Nonequilibrium-Molecular-Dynamics Computer Simulations. *Phys. Rev. E* **1996**, *53* (3), 2531–2536.

(16) Milchev, A.; Paturej, J.; Rostiashvili, V. G.; Vilgis, T. A. Thermal Degradation of Adsorbed Bottle-Brush Macromolecules: a Molecular Dynamics Simulation. *Macromolecules* **2011**, *44* (10), 3981–3987.

(17) Aubouy, M.; Harden, J. L.; Cates, M. E. Shear-Induced Deformation and Desorption of Grafted Polymer Layers. *J. Phys. II* **1996**, *6* (7), 969–984.

(18) Carl, W.; Makhloufi, R.; Kröger, M. On the Shape and Rheology of Linear Micelles in Dilute Solutions. *J. Phys. II* **1997**, *7* (6), 931–946.

(19) Rottler, J.; Barsky, S.; Robbins, M. Cracks and Crazes: on Calculating the Macroscopic Fracture Energy of Glassy Polymers From Molecular Simulations. *Phys. Rev. Lett.* **2002**, *89* (14), 148304.

(20) Ge, T.; Pierce, F.; Perahia, D.; Grest, G.; Robbins, M. Molecular Dynamics Simulations of Polymer Welding: Strength From Interfacial Entanglements. *Phys. Rev. Lett.* **2013**, *110* (9), 098301.

APPENDIX I [2]

AI.1 Self-Consistent Field (SCF) theory

Consider a linear chain made of N beads of bead size σ (Chapter 5). For a planar brush composed of such linear chains under marginal solvent conditions (dimensionless mixing free energy $f(\phi) = \tau\phi^2$ in terms of the polymer volume fraction ϕ) one expects an unconfined brush height

$$h = \frac{2(p\tau\sigma^2)^{1/3} N\sigma}{(\pi^2\Sigma)^{1/3}} \qquad \text{I-1}$$

with $p = 1$ for flexible chains. Here, τ (not to be confused with normal stress τ_{zz}) is an adjustable parameter related to solvent quality and can be estimated using this formula from the measured h if the surface area per chain, Σ, has been estimated independently. In the presence of an opposing wall (or opposing impenetrable brush) at altitude H but otherwise identical conditions the classical SCF yields a volume fraction profile,

$$\phi_H(z) = \frac{N\sigma^3}{\Sigma H} + \frac{\lambda^2 H^2}{6\tau}\left(1 - \frac{3z^2}{H^2}\right), \qquad z \le H \qquad \text{I-2}$$

where $H = h$ as long as the brush and wall or brush and brush are not yet in contact, and $H = D/2$ with wall separation D if opposing brushes are in contact, i.e., $H = \min(h, D/2)$. Here λ abbreviates a characteristic wave number

[2] Most part of this chapter is taken from my already published work: "Polymer Brushes under Shear*: Molecular Dynamics Simulation Compared to Experiments" Langmuir 2015, (31) 4798-4805*. I carried all the simulation work and co-authors participated in discussions and interpretation of the work.

$$\lambda \equiv \left(\frac{3\pi^2}{8p\sigma^2N^2}\right)^{1/2} \qquad \text{I-3}$$

Using the Derjaguin approximation the experimentally measured *F/R* curve in a crossed cylinder setup can be calculated using the normal pressure at the outer edge of the confined planar brush, $P(H) = \tau_{zz}(2H) = \tau_{zz}(D)$ with

$$P(H) = \frac{k_B T}{\sigma^3}\,(\phi f' - f)_{\phi=\phi_H(H)} = \frac{k_B T}{\sigma^3}\,\tau\phi_H^2(H) = P_0\left(\frac{q^3-1}{q}\right)^2 \qquad \text{I-4}$$

where $q = H/h$ is a dimensionless compression ratio and

$$P_0 = \frac{\pi^{4/3}\,k_B\,T}{4(\sigma p^2\,\Sigma^4/\tau)^{1/3}} \qquad \text{I-5}$$

a characteristic pressure. Thus,

$$\frac{F}{R} = \int_D^{2h} \tau_{zz}\,(D')dD'$$

$$= 2\int_{D/2}^{h} P(H)dH$$

$$= 2P_0h\int_d^1 \left(\frac{q^3-1}{q}\right)^2 dq, \qquad d = \frac{D}{2h}$$

$$= 2P_0h\left(d^2 + \frac{1}{d} - \frac{1}{5}d^5 - \frac{9}{5}\right) \qquad \text{I-6}$$

The result diverges when the walls approach each other, and monotonically decreases with increasing d. For d = 1, F/R vanishes, as it should. The prefactor can also be written as:

$$2P_0h = \left(\frac{\pi^2\sigma^4\tau^2}{p\Sigma^5}\right)^{1/3} Nk_BT \qquad \text{I-7}$$

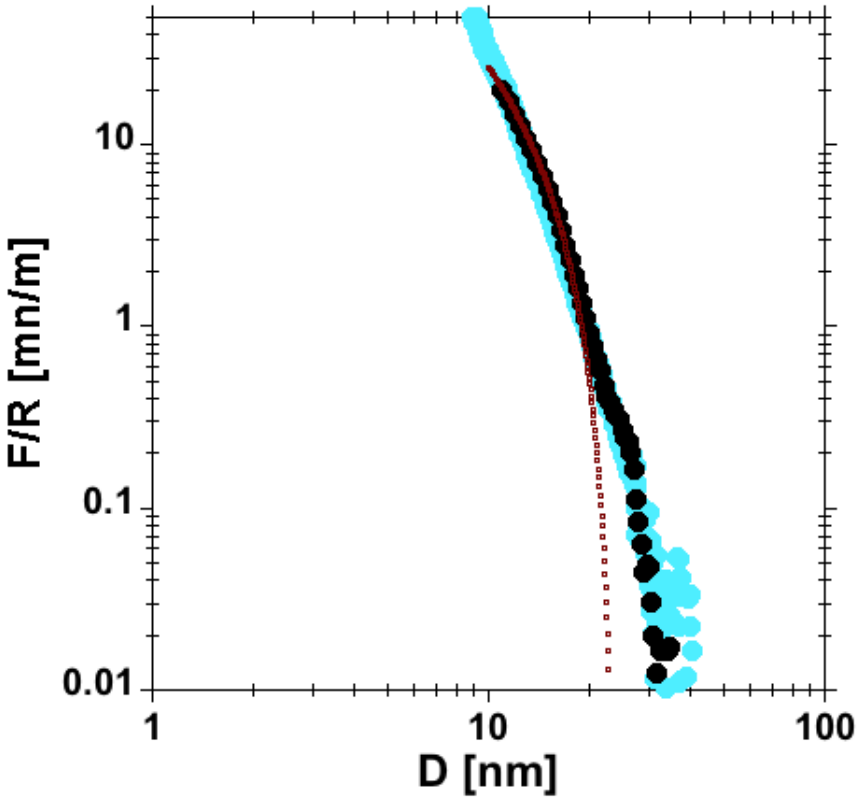

Figure I.3 : Force against distance curve from SFA experiments (cyan dots), MD Simulation (black dots) and SCF theory expression eq. A6 (brown dots) for σ = 0.5 nm, N = 50, Σ = 3.22 nm^{-2} and τ = 1.98.

AI.2 Attractive interaction in Brush-brush system

- An attractive term may also be considered for the brush-brush system. The repulsion for the brush-brush system is however stronger, the maximum applied pressure smaller, and as a result the effect of attractive term is thus less relevant than for the brush-wall system. To be more specific, the difference of the repulsive force for the two systems has two origins:

- The steric hydration force is stronger for the brush-brush system. Compression of the brush against the hard wall leads to stronger dehydration than the compression of two soft (brush-brush) interfaces.
- The entropic term of the osmotic force is larger for the brush-brush system, as it results from two rather than a single brush.

Thus, even if a van der Waals attraction is present in both cases, the repulsion is stronger in the brush-brush system than in the brush-wall system. As an empirically confirmed result is the fluid film between two brushes thicker than for the corresponding brush-wall system.

APPENDIX II

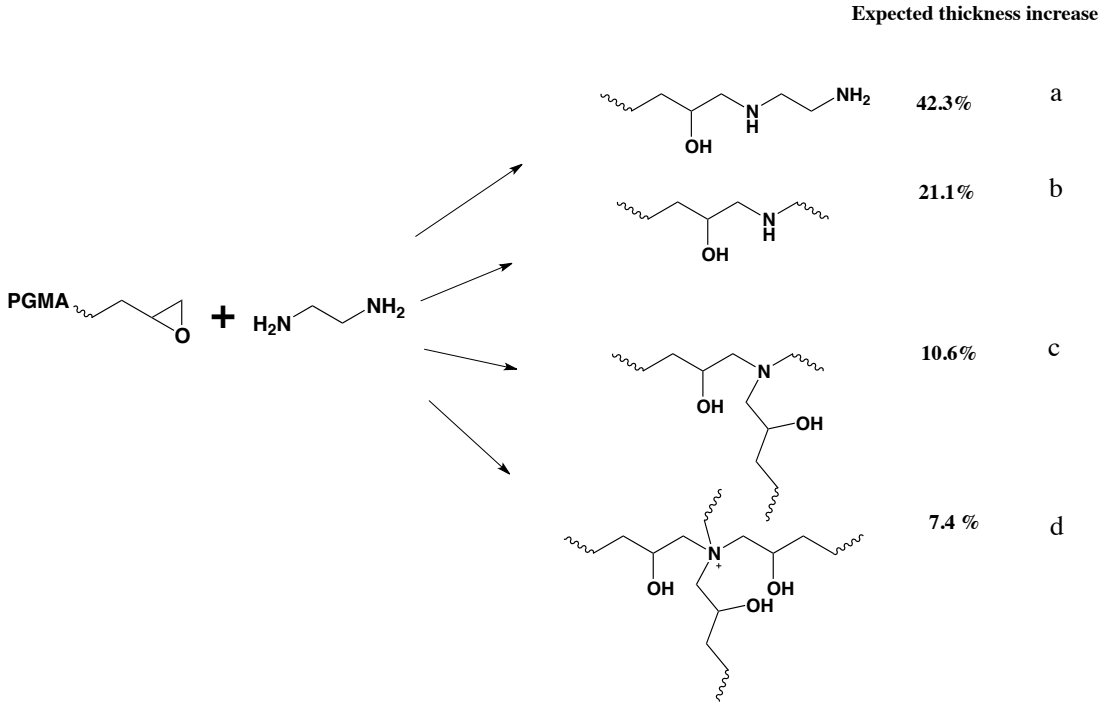

Figure II.1: Possible reaction routes between ethane-1,2-diamine and PGMA brushes.

PGMA brushes were cross-linked by ethane-1,2-diamine in a post-modification manner (Figure II.1). The reaction between ethane-1,2-diamine and PGMA could have four different possibilities, with different thickness increments expected owing to the different amount of cross-linker added to the PGMA brushes (Figure 2.2). Specifically, (a) if only one amine group in diamine reacts with one epoxypropyl group in PGMA, and assuming that the density of PGMA brushes remained constant before and after crosslinking, 42.3% thickness increase for PGMA brushes could be expected; (b) if two amine groups in diamine react with two epoxypropyl groups, 21.1% increase of PGMA brushes thickness would be expected; (c) if each amine group in diamine reacts twice and consumes four epoxypropyl groups, 10.6% of total thickness increase could be expected; and finally, (d), if each amine group in the diamine cross-linker reacts three times and consumes six epoxypropyl groups, a 7.4% increase of total thickness could be expected. In order to examine these possibilities,

we cross-linked PGMA brushes with ethane-1,2-diamine under different conditions. Firstly, PGMA brushes were immersed with the thicknesses of 153.9 nm and 99.6 nm into 5 ml ethanol solution at 60 °C, and 0.2ml ethane-1,2-diamine was added as cross-linker. The kinetics of thickness increase with immersion time is as follows:

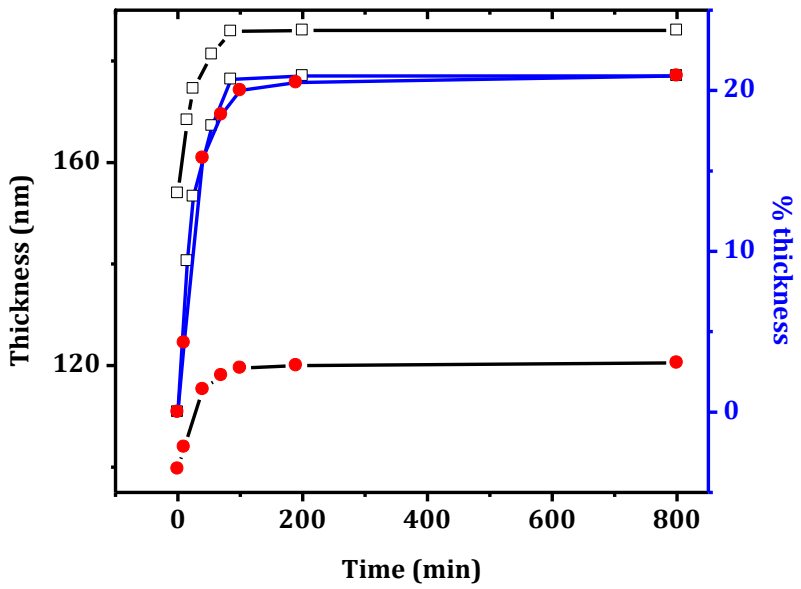

Figure II.2: Cross-linking of PGMA brushes with different thickness by ethane-1,2-diamine (4% v/v) in ethanol; □ and ● represent PGMA brushes with a thickness of 153.9 nm and 99.6 nm, respectively.

From Figure II.2 we can see that both PGMA brushes with two different thicknesses have similar thickness-increase kinetics and the final thickness increment is around 21% of initial dry thickness, with no further thickness increase being observed upon extending cross-linking time. This indicates the complete consumption of epoxypropyl groups in PGMA brushes and is quite consistent with case (b), in which both amine groups of diamine reacted only once with epoxypropyl group in PGMA.

In order to examine cases (c) and (d), cross-linking reactions were firstly carried out under the same conditions as in case (b), however, as soon as the thickness increment reached 10%, samples were removed from cross-linking solution and re-immersed into pure ethanol at 60 °C. In such a case, there should have been an excess amount of

unreacted epoxypropyl groups in the PGMA brushes, which could potentially continue to react with secondary amine groups. To allow this possibility to happen, the semi-cross-linked PGMA sample was immersed in pure ethanol for further 12h. Diamine cross-linker was subsequently added to sample containing ethanol solution and it was found that the thickness of PGMA brushes continue to increase until the total thickness increment reached around 21% (Figure 2.4 (red circle)). The above observations indicate that cases (c) and (d) are highly unlikely under the present experimental conditions, because if cases (c) or (d) happened in the cross-linking reaction, the final thickness increment would below 21% due to the consumption of epoxypropyl groups by the secondary amine, and thus less cross-linker would add to PGMA brush and contribute less to thickness increment.

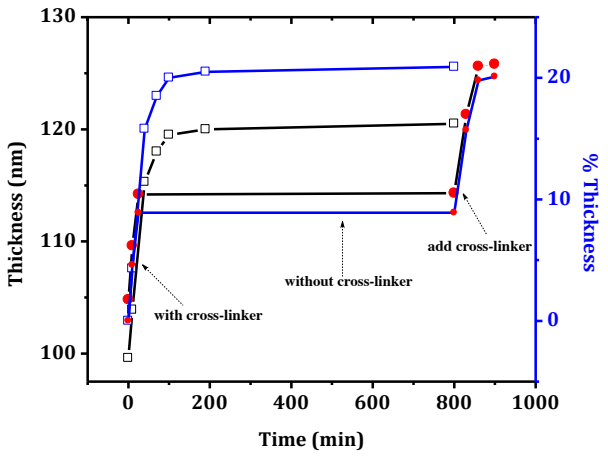

Figure II.3: Cross-linking of PGMA over time. (□) PGMA brushes with thickness of 99.5 nm and cross-linked under the same conditions as in case (b). (●) PGMA brushes (104.3nm) subsequently cross-linked under the same conditions with (□) until the thickness increment reached 10%, immersed in pure ethanol for 12h, after which 4% ethane-1,2-diamine ethanol solution was added.

Finally, we examined the possibility of case (a) by increasing the cross-linker concentration. Here we used a mixture of 5ml ethane-1,2-diamine and 5ml ethanol as the cross-linking solution, and the PGMA brush dry thickness increment kinetics were as follows:

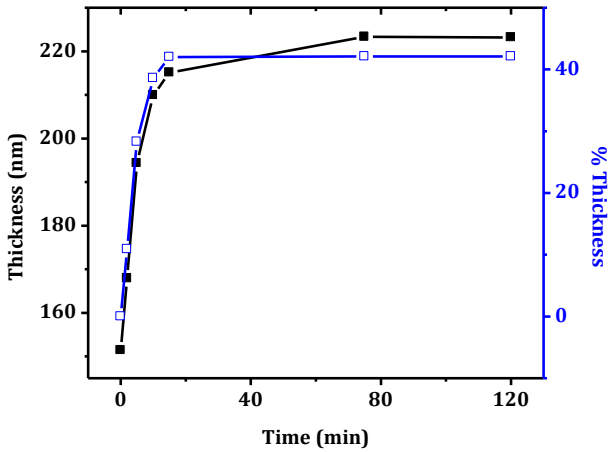

Figure II.4: Cross-linking of PGMA under 50% (v/v) concentration of diamine cross-linker in ethanol.

In conclusion, cross-linking between diamine and PGMA could happen for cases (a) and (b), which could be controlled by using different cross-linker concentrations l. Specifically, case (a) could happen when the crosslinker has a high concentration in solution, such as 50%, while under lower crosslinker concentrations, such as 4%, case (b) is more likely to happen. Cases (c) and (d) are not possible under the present experimental conditions, probably due to the secondary amine having a high steric requirement for participating in the reaction. For the rest of this thesis, the cross-linking of PGMA brushes was performed as in case (b). The cross-linking introduced hydroxyl groups into the polymer chains and rendered the cross-linked PGMA films hydrophilic.

APPENDIX III

AIII.1 Stress/Pressure Calculation

The stresses were calculated using Irving-Kirkwood formula. The pressure or stress acting on each beads has two components: kinetic and virial. Virial again has contribution from pair interactions, bond interactions, angle interaction (bending stiffness of chain), charge interactions etc. In this thesis I have considered only pair and bond interactions except when I have studied effect of chain-stiffness in chapter 6.

Stress/Pressure = Kinetic + Virial

Kinetic Stress/Pressure,

$$P_{kinetic_{ij}} = \frac{\sum_k^N m_k v_{k_i} v_{k_j}}{V} \qquad \text{III-1}$$

Virial = Pair + Bond + Angle + Coloumb + …

Virial Stress/Pressure

$$P_{virial_{ij}} = \frac{\sum_k^N r_{k_i} f_{k_j}}{V} \qquad \text{III-2}$$

Where, P is pressure or stress, i, j stands for x, y or z, k is kth bead, m is mass, v is velocity, V is volume, r is distance between any two beads and f is force acting on bead.

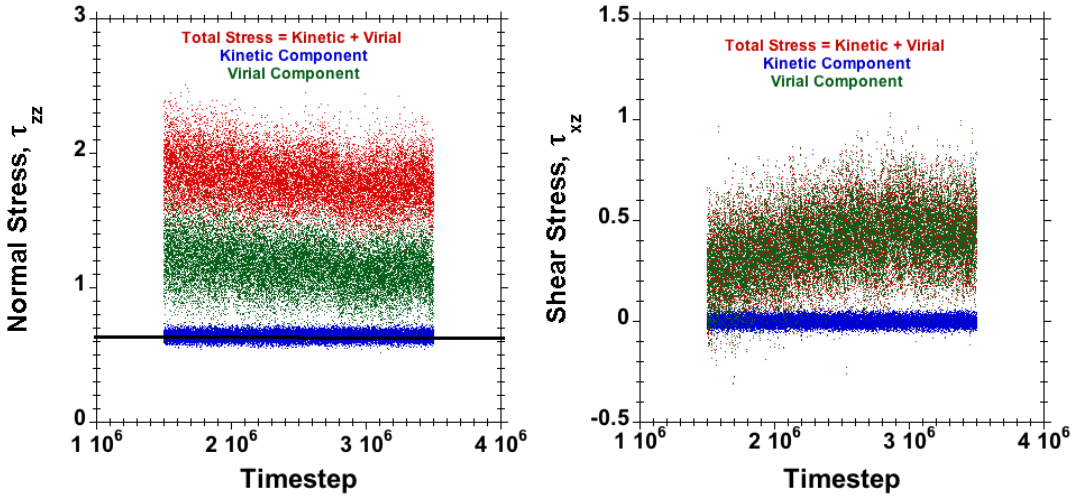

Figure III.1 Stress calculation for a brush-against-wall system with M = 20 chains, N = 50 beads per chain and ρ = 0.075. The simulation was done for separation, D = 7 between grafting-surface and counter wall-surface at a shear speed, S = 0.01 applied on the tether beads. Kinetic component in the normal stress is equal to ideal gas pressure, $\rho_n k_B T$ = 0.54*1*1.2 = 0.64 (reduced LJ units).

Acknowledgement

I express my deepest sense of gratitude to my mentor and research supervisor Prof. Dr. Nicholas D. Spencer, Department of Materials, ETH Zurich, Switzerland. He introduced me to the field of Nanotribology and Surface Science. His advice during the interpretation of data is commendable and has moulded me perfectly for the next level in research. He has been very kind to me in both academic and personal matters and I am very indebted to him for the freedom and support which he has given me during this period, in fact it has helped me to think and do research with confidence. I am really amazed by his hard work and untiring efforts; he has truly been an inspiration to me.

I would like to thank Prof. Dr. Martin Kroger, Department of Materials, ETH Zurich, Switzerland for his immense interest, constant guidance and encouragement throughout my PhD study. I feel really fortunate to learn from him. He would always be an inspiration to write more effcient and simpler codes.

I would take this opportunity to thank Prof. Dr Patrick Ilg, School of Physical and Mathematical Sciences, University of Reading, United Kingdom for being my adviser. He introduced and trained me into LAMMPS from the beginning and was always there to help me even after moving to UK.

I am also thankful to Prof. Dr. Rosa M. Espinosa Marzal, Civil and Environmental Engineering, University of Illinois at Urbana-Champaign, United States for introducing me to AFM and nanotribology experiments. She always helped me to understand my results and had many useful interactions on Skype after she moved to US.

I express my gratitude to Prof. Mark O. Robbins, Department of Physics and Astronomy, John Hopkins University, Baltimore, US for his useful discussion, encouragement and motivation.

A special thanks to Prof. Dr. Walter Steurer, Department of Materials, ETH Zurich, Switzerland to agree to chair my thesis defense on a very short notice.

I thank all the faculty and staff members of Department of Materials, ETH Zurich for providing support directly and indirectly.

I express my thanks to Josephine for administrative help and translating many of the official communications from German to English. Special thanks to Rebecca, Chris and Sara for translating abstract of my thesis to German.

My stay in the lab was a pleasant experience and was like staying with a family. I am thankful to my past and present colleagues Deepak, Prathima, Shiva, Vikrant, Venky, Ang, Chengjun, Ke, Chaterien, Maura, Clement, Tolga, Adie, Nicolas, Rebecca, Yvonne, Zita, Alok, Siddarth, Chris, Moh, Ella, Fabiana, Andrea, Giulia, Olof, Angela to mention a few of a along list for making my stay in LSST a memorable experience.

For me the continuous support and cooperation of my parents, uncles, aunts, sisters and brothers has been indispensable. They always supported and guided me and at the same time gave freedom to follow my dreams. I owe them a great debt and gratitude.

A special thanks to a very special person, a friend for almost a decade and now my wife Joyee for being a support and understanding me in my good and bad times.

These simple words are not at all sufficient to express my heartfelt gratitude I have for each and every one of them and they deserve a lot more credit than just these simple words.